Low-Dimensional Semiconductor Heterostructures and Device Applications in Optoelectronics and Renewable Energy

Hong Nhung Tran

Department of Electrical and Computer Engineering
Faculty of Engineering
McGill University
Montreal, Canada

August 2019

A thesis submitted to McGill University in partial fulfillment of the requirements
of
the degree of Doctor of Philosophy

To my Husband- Huy Binh Le and my Family

Table of Contents

Abstract

The development of high efficiency optoelectronic devices operating in the ultraviolet (UV) range, especially UV-C band (200 – 280 nm), has been fundamentally limited by large dislocation densities and poor *p*-type conduction in AlGaN planar heterostructures grown on lattice mismatched substrates. By employing nanowire heterostructures using molecular beam epitaxy (MBE) technique, the crystalline quality and *p*-doping in group III-nitride materials can be significantly improved. In this dissertation, we have elucidated that the unusually high room-temperature hole concentrations up to $\sim 6 \times 10^{17}$ cm^{-3} measured in Mg-doped AlN nanowires stem from the efficient hole hopping conduction in the Mg impurity band, driven by the significantly enhanced Mg-dopant incorporation in nearly defect-free AlN nanostructures. Detailed temperature- and gate-dependent studies of AlN nanowire transistors reveal the distinct signatures of hole hopping conduction in the Mg impurity band, which include a relatively small activation energy for electrical conductivity and an increase in hole mobility with temperature.

In visible and near-infrared wavelength range, we also study two-dimensional layered transition metal dichalcogenides (TMDCs), which have emerged as an excellent candidate for flexible and transparent optoelectronic devices. We first investigate the quantum efficiency of monolayer MoS_2 via detailed temperature- and power-dependent photoluminescence studies. From rate equation analysis, the maximum achievable internal quantum efficiencies in monolayer MoS_2 at 83 and 300 K are determined to be 45% and 8.3%, respectively. Noticeably, efficiency droop is clearly observed at high carrier injection concentrations due to the unusually large Auger recombination coefficient, which is calculated to be $\sim 10^{-24}$ cm^6/s at room temperature, nearly 6 orders of magnitude higher than that of conventional bulk semiconductors. In contrast, four-layer

MoS_2 exhibits much weaker efficiency droop, and is therefore used to fabricate, for the first time, room-temperature laser devices with a remarkably low threshold power of ~5 μW under continuous wave operation.

We have further exploited the application of III-nitride nanowire heterostructures in the field of renewable energy, specifically hydrogen production, and demonstrated large-scale photocatalytic water splitting under concentrated natural sunlight. The synthesis of double-band *p*-GaN/InGaN nanowire arrays on large Si substrate (3” in diameter) by MBE has been studied and resulted in an apparent quantum efficiency up to ~28.8% in the visible range of 400 – 480 nm. Consequently, a solar-to-hydrogen energy conversion efficiency of ~1.1% can be derived under concentrated natural sunlight. The achievement brings us one step closer towards a large-scale practical hydrogen fuel generation system.

Abrégé

Le développement de dispositifs optoélectroniques à haute efficacité dans le spectre ultraviolet (UV), en particulier la bande UV-C (200 - 280 nm), est fondamentalement limité par de hautes densités de dislocations et une faible conduction de type p dans les hétérostructures planaires en AlGaN. En utilisant des hétérostructures à base de nanofils par épitaxie par jet moléculaire (MBE), la qualité cristalline et le dopage de type p dans les matériaux à base des III-Nitrures peuvent être considérablement améliorés. Dans cette thèse, nous avons élucidé que les concentrations inhabituellement élevées de trous à la température ambiante allant jusqu'à environ 6×10^{17} cm^{-3}, mesurées dans des nanofils en AlN dopés au Mg, résultent de la conduction efficace de sauts de trous dans la bande d'impuretés de Mg, entraînée par l'incorporation du Mg dans ces nanostructures en AlN presque exemptes de défauts. Des études détaillées de transistors à base de nanofils en AlN révèlent les signatures distinctes de la conduction de sauts de trous dans la bande d'impuretés de Mg, incluant une énergie d'activation relativement faible pour la conductivité électrique et une augmentation de la mobilité des trous avec une hausse de la température.

Dans le spectre des longueurs d'onde visibles et infrarouges, nous avons également étudié les dichalcogénures de métaux de transition (TMDC), qui, en couches bidimensionnels, se sont révélés être un excellent candidat pour les dispositifs optoélectroniques souples et transparents. Nous avons d'abord étudié l'efficacité quantique des monocouches en MoS_2 par des études détaillées de photoluminescence. Ces analyses démontrent des efficacités quantiques internes maximales pouvant atteindre 45% et 8,3% dans ces monocouches en MoS_2 à 83 et 300 K, respectivement. Il est à noter que l'efficacité est réduite à cause d'un coefficient de recombinaison Auger exceptionnellement élevé, calculé comme étant d'environ 10^{-24} cm^6/s à température

ambiante, soit près de six ordres de grandeur plus élevé que celui des semiconducteurs classiques. Par ailleurs, le MoS_2 comprenant quatre couches présente une réduction beaucoup plus faible, et est donc utilisé pour fabriquer, pour la première fois, des dispositifs laser à température ambiante avec une puissance de seuil remarquablement faible d'environ 5 µW.

Nous avons davantage exploité l'application des hétérostructures à base de nanofils à base des III-Nitrures dans le domaine des énergies renouvelables, en particulier de la production d'hydrogène, et avons démontré la séparation photocatalytique de l'eau à grande échelle sous une lumière solaire naturelle concentrée. La synthèse de réseaux de nanofils *p*-GaN/InGaN sur un substrat de Si (3 pouces de diamètre) par MBE a fait l'objet d'études, résultant à une efficacité quantique apparente allant jusqu'à environ 28,8% dans le spectre visible de 400 à 480 nm. Par conséquent, un rendement de conversion d'énergie solaire en hydrogène d'environ 1,1% peut être obtenu sous une lumière solaire naturelle concentrée. Cette réalisation est une étape importante vers un système de production pratique de combustibles à base d'hydrogène à grande échelle.

Acknowledgement

This doctoral dissertation would not be completed without the supervision, support and encouragement from many people. I would like to take this as a golden chance to express my sincere appreciation to every individual who has helped me during this wonderful journey.

First of all, I am greatly thankful to my supervisors, Prof. Zetian Mi and Prof. Thomas Szkopek, for providing tremendous support, consistent encouragement and thoughtful suggestions throughout my PhD study from nearly every aspect of my life to the research. They have spent hours to listen to my problems and helped me find the solutions. Under their supervision, I have gained so much research experience that is absolutely useful for my future career. I consider myself very fortunate to have them as my supervisors. I also would like to thank Professors Nate Quitoriano, Ishiang Shih, and Odile Liboiron-Ladouceur for their valuable comments, suggestions and guidance on my research topics. I also wish to acknowledge my PhD defence committee members, Professors Chao-Jun Li, Jun Song, Francois Bouffard, and Arun Misra for their interest, evaluation and valuable suggestions.

During my PhD study at McGill University, I am indebted to all my colleagues for their time, assistance, suggestions and discussions. My special thanks to Dr. Huy Binh Le, Dr. Omid Salehzadeh, Dr. Songrui Zhao, Dr. Yong-Ho Ra, and Dr. Faqrul A. Chowdhury. Dr. Huy Binh Le and Dr. Omid Salehzadeh have offered me invaluable lessons about material science and measurement techniques. Dr. Songrui Zhao, Dr. Yong-Ho Ra, Dr. Faqrul A. Chowdhury and Dr. Renjie Wang explained the basics and operation of MBE system for me. I gladly appreciate Dr. Faqrul A. Chowdhury, who helped me understand the water splitting experiment setup and analysis by providing very detailed explanation. In this context, I am also grateful to Dr. Yichen Wang for

his insightful discussions and assistance during the initial stage of photocatalyst optimization. Here I am sincerely listing the names of other colleagues who helped me a lot during my stay at McGill University: Dr. Hieu P. T. Nguyen, Dr. Qi Wang, Dr. Md Golam Kibria, Dr. Baowen Zhou, Dr. Sheng Chu, Dr. Ashfiqua Connie, Dr. Yongjie Wang, Dr. Renjie Wang, Pegah Ghamari, Dr. Sharif Sadaf, Roksana Rashid, Nick Pant and Xianhe Liu. A very special thanks to David Laleyan for translating the abstract to French.

I would like to express my great thanks to Donald Pavlasek, shop supervisor at the ECE Design and Machining facility, who always come up with brilliant ideas for the tools and especially the chambers needed for my experiments. I also want to present my deep gratitude to the staff members of McGill Nanotools Microfab (MNM) including Dr. Matthieu Manini, Donald Berry, Jun Lee, Dr. Lino Eugene, Dr. Zhao Lu, Sasa Ristic and Peng Yang for their technical support, trainings and discussions on my research. My sincere thanks to Patricia Moraille, Christophe Clément and Marie-Hélène Bernier at University of Montreal for their support and discussion on AFM, EBL, and cleanroom tools. Great appreciation I would like to send to Dr. Michel L. Trudeau at Science des Matériaux, IREQ, Hydro-Québec and Dr. David Liu at FEMR, McGill University for carrying out TEM imaging on my samples. Special thanks to Dr. David Liu for his detailed instructions on SEM and EDXS characterizations and for being there for me whenever I had problems with the tool or needed discussion about the research topics.

Most of all, my heartfelt appreciation goes to my Grandparents, my parents Van-Thuc Tran and Thi-Hoa Luong, my parents-in-law Huy-Son Le and Thi-Hang-Nga Nguyen, all my brothers, sisters and relatives for their love, support, encouragement and strong belief in my study. My sincere and special thanks are dedicated to my husband also my colleague, Dr. Huy Binh Le, and our beloved daughter, Tran-Thanh-Thu Le who are always with me under any circumstances. My daughter's sentences: "Mommy, you are close to finish. Try your best and you will be able to make it. I am always beside you" keep me going and never give up, no matter how hard the situation is. I am heartily thankful for their endless support, patience, encouragement and love.

I sincerely acknowledge the McGill Engineering Doctoral Award (MEDA) for their financial support during my PhD pursuit. This dissertation work would not be possible without financial support for equipment and facilities from Natural Sciences and Engineering Research Council of Canada (NSERC), U.S. Army Research Office and US Department of Energy EERE Program.

List of Figures

List of Tables

List of Acronyms

1D	One Dimension
2D	Two Dimension
3D	Three Dimension
AFM	Atomic Force Microscopy
AQE	Apparent Quantum Efficiency
AQY	Apparent Quantum Yield
ATP	Adenosine Triphosphate
BEP	Beam Equivalent Pressure
CBE	Chemical Beam Epitaxy
CBM	Conduction Band Minimum
CCD	Charge Coupled Device
CPC	Compound Parabolic Concentrator
CVD	Chemical Vapor Deposition
DI	De-ionized
EBL	Electron-Beam Lithography
ECE	Energy Conversion Efficiency
EDXS	Energy Dispersive X-Ray Scanning
EQE	External Quantum Efficiency
FWHM	Full Width at Half-Maximum
HER	Hydrogen Evolution Reaction
HH	Heavy Hole

IQE	Internal Quantum Efficiency
LD	Laser Diode
LED	Light-Emitting Diode
LH	Light Hole
MBE	Molecular Beam Epitaxy
MOCVD	Metal-Organic Chemical Vapor Deposition
MOVPE	Metal-Organic Vapor Phase Epitaxy
MQW	Multiple-Quantum-Well
NADPH	Nicotinamide Adenine Dinucleotide Phosphate
NHE	Normal Hydrogen Electrode
OER	Oxygen Evolution Reaction
OWS	Overall Water Splitting
PC	Photocatalytic/Photochemical
PL	Photoluminescence
PEC	Photoelectrochemical
PMT	Photomultiplier
PV	Photovoltaic
PECVD	Plasma-Enhanced Chemical Vapor Deposition
RF-PAMBE	Radio-Frequency Plasma-Assisted Molecular Beam Epitaxy
RHEED	Reflection High-Energy Electron Diffraction
SAG	Selective Area Growth
SCCM	Standard Cubic Centimeter per Minute
SE	Secondary Electron

SEM	Scanning Electron Microscopy
STEM-HAADF	Scanning Transmission Electron Microscopy High-Angle Annular Dark-Field
STEM-BF	Scanning Transmission Electron Microscopy High-Angle Annular Bright-Field
STH	Solar-To-Hydrogen
SPSL	Short-Period Superlattice
TCD	Thermal Conductivity Detector
TDD	Threading Dislocation Density
TE	Transverse Electric
TEM	Transmission Electron Microscopy
TMDC	Transition Metal Dichalcogenide
TW	Terawatts
TWy	Terawatt-Years
UHV	Ultra-High Vacuum
UV	Ultraviolet
VBM	Valance Band Maximum
VPE	Vapor Phase Epitaxy
VLS	Vapor-Liquid-Solid
WGM	Whispering Gallery Mode
XPS	X-Ray Photoelectron Spectroscopy

Contribution of Authors

This dissertation work includes the contribution of the candidate and many other individuals. The candidate and her supervisor, Prof. Zetian Mi, defined the projects and worked closely on the designs, experiment setups, and manuscripts preparation. The contributions of the candidate and co-authors to the works presented in Chapters 3 – 5 are described as follows:

In Chapter 3, the MBE growth of Mg-doped AlN nanowires was performed by Dr. Songrui Zhao. The candidate carried out the device fabrication, the optical and electrical characterizations with some assistance from Dr. Huy Binh Le and Dr. Songrui Zhao. In Chapter 4, the candidate was responsible for sample preparation including thermal oxidation of Si substrate and exfoliation of MoS_2 flakes. The sample thickness determination was done by the candidate via optical microscope and AFM characterization. The candidate significantly contributed to the fabrication process of free-standing SiO_x microdisk by both photolithography and electron-beam lithography. The pre-pattern for locating MoS_2 flakes on Si/SiO_x substrate was designed and prepared by the candidate. In both studies presented in Chapter 4, the candidate has significant contribution to PL measurements and data analysis. The candidate has taken consents from Dr. Omid Salehzadeh and other co-authors to include the manuscripts in this dissertation. The project in Chapter 5 was designed and led by Prof. Mi, Dr. Faqrul A. Chowdhury, and the candidate. The sample preparation for the MBE growth was carried out by the candidate with some help from Roksana Rashid. The candidate and Dr. Faqrul A. Chowdhury optimized the synthesis on large-scale wafer and performed the MBE growths together with Dr. Yichen Wang and Roksana Rashid. The candidate performed SEM and PL measurements. The indoor experiments were primarily conducted by the candidate with some assistance from Dr. Faqrul A. Chowdhury for co-catalyst optimization and sample preparation on larger scale. Dr. Faqrul A. Chowdhury and the candidate conducted the intensity dependent measurements and the outdoor experiments under natural sunlight. The TEM analysis was carried out by Michel L. Trudeau at Science des Matériaux, IREQ, Hydro-Québec, Canada. Dr. Faqrul A. Chowdhury contributed to the calculation of apparent quantum efficiency and energy conversion efficiency. Prof. Hong Guo at the Department of Physics, McGill University contributed to the result analysis and discussions. In Chapter 6, Section 6.2.1, the coalesced AlN:Si thin film (shown in Figure 6-2) was grown by Dr. Huy Binh Le. Dr. Huy Binh Le prepared the illustration in Figure 6-1a. The candidate performed SEM characterization and device fabrication for Hall measurement (not reported).

Chapter 1: Introduction

1.1. Recent Developments and Challenges of III-Nitride Semiconductors for Ultraviolet Light-Emitting Elements

Ultraviolet light emitters such as light-emitting diodes (LEDs) and laser diodes (LDs) are more and more important due to their wide variety of applications in industry, life science and environment. For instance, 3-dimensional (3D) printing for lightweight construction, UV curing of paints, inks, or blood gas analysis have been using emission in the UV-A spectral range (315 – 400 nm). Meanwhile, the UV-B light (280 – 315 nm) has found its key applications in phototherapy [1] as well as plant lighting [2]. Applications in the UV-C band (200 – 280 nm) include water purification [3], disinfection of medical equipment and food [4], and bioagent sensing [5]. Compared to traditional mercury or xenon lamps, which have been widely used as sources of UV emission in the past decades, UV LEDs offer a number of benefits including cost effectiveness, long lifetime, environmental friendliness, and especially tunable emission wavelength. Not surprisingly, the market share of UV LEDs is forecasted by Yole Développement to reach US $320 million in 2020 [6].

Among wide bandgap semiconductors, AlGaN alloys have emerged as the most promising candidate for optoelectronic devices operating in wide range of the UV spectrum (wavelength ~365 – 200 nm, corresponding to bandgap energy from 3.4 – 6.2 eV), due to their unique features such as high electron mobility, high chemical stability, large saturation velocity, and direct bandgap in the entire composition range [7, 8]. Research into AlGaN-based UV emitters has undergone an accelerating development with the target of 250 – 330 nm LDs and a few tens percent external quantum efficiency (EQE) for LEDs with emission wavelengths shorter than 350 nm [8].

However, III-nitride planar deep UV LEDs and LDs still exhibit poor performance, of which the major challenges will be discussed in Section 1.1.1. Figure 1.1 summarizes the reported EQEs for UV LEDs based on III-nitride semiconductor materials [9], showing a significant reduction in EQE at peak emission wavelengths below ~260 nm. In other words, the device performance severely diminishes with increasing the Al composition in AlGaN alloys. For example, the maximum reported EQE (output power) of the 227 nm, 237 nm, and 247 – 250 nm LEDs are 0.2% (0.15 mW), 0.4% (5 mW), 1.8% (25 mW), respectively [8, 10]. Similarly, AlGaN multiple-quantum-well (MQW) UV-LDs also exhibit poor performance with decreasing wavelength. The shortest wavelength achieved so far for electrically injected AlGaN MQW laser is 336 nm, and with relatively large threshold current density of 17.6 kA/cm^2 [11].

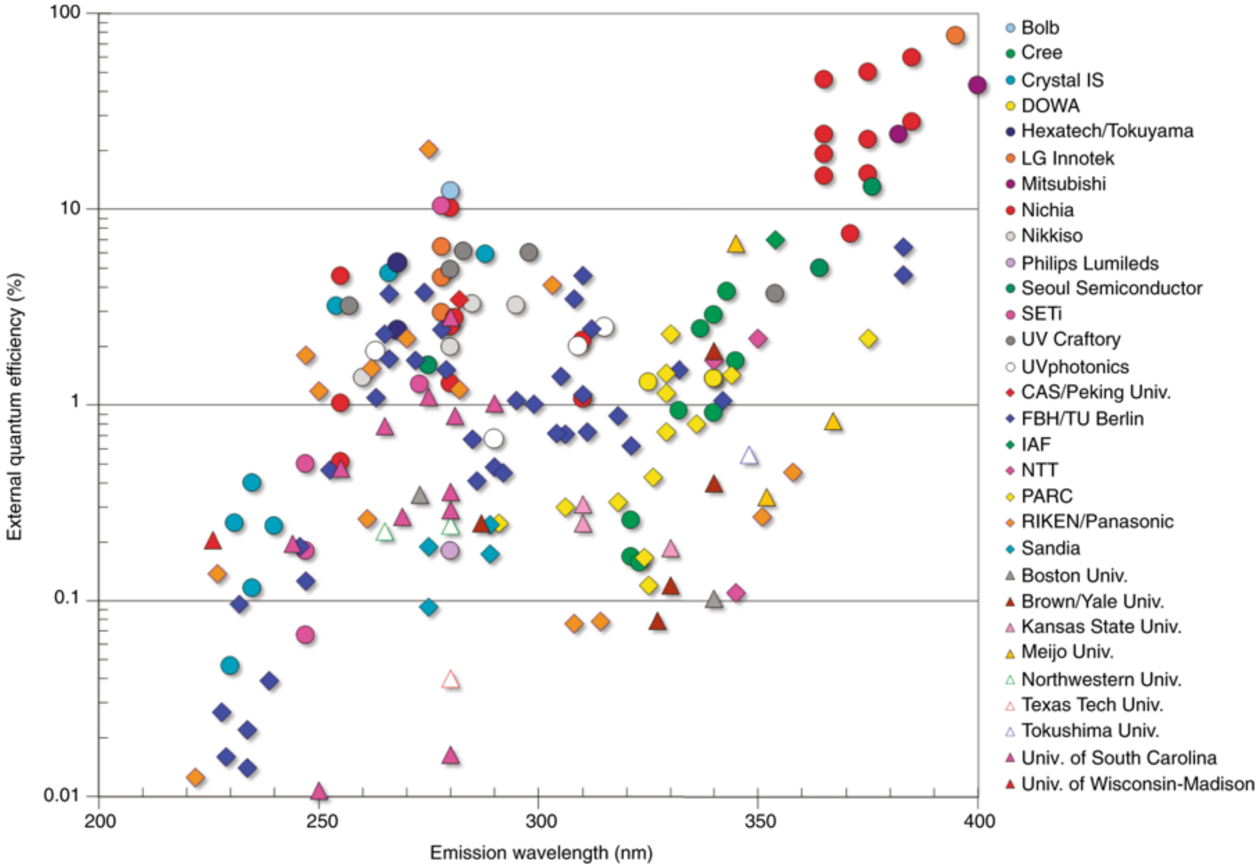

Figure 1-1: State-of-the-art EQE for III-nitride quantum well LEDs operating at wavelengths from 220 – 400 nm [9]. A clear drop of EQE can be seen as approaching UV-C range.

Consequently, the number of companies offering LED devices in the UV-B and UV-C range is much sparser than that selling UV-A LEDs. Albeit the modest performance of AlGaN-based deep UV light emitters, it is expected to improve the efficiencies and output powers over the coming years.

1.1.1. Challenges of Al(Ga)N Epilayers

This section focuses on the key factors that largely limit the performance of planar Al(Ga)N UV emitters. They are summarized in the paragraphs below.

P-type doping

One of the most formidable challenges to the development of high-efficiency deep UV LEDs and LDs is inefficient doping due to the significantly reduced thermally activated carrier concentration as increasing the bandgap energy, especially for *p*-type dopants. For example, the activation energy of magnesium (Mg), a typical *p*-dopant in III-nitride semiconductors, dramatically increases from ~0.2 eV for GaN to ~0.5 – 0.6 eV for AlN [12-16]. Consequently, the hole concentration in Mg-doped AlGaN epilayers with high Al content is very low, leading to poor *p*-type conduction that seriously limits the device performance through low hole injection and Joule heating. In addition, deep UV LEDs also suffer from low light extraction efficiency (< 25% in the UV-C range) caused by the absorption of the *p*-GaN, semitransparent *p*-AlGaN, or short-period superlattice (SPSL) contact layers [17]. The search for materials that are both *p*-type conductive and UV-transparent therefore remains difficult.

Defects and dislocations

An additional challenge arises from the lack of a lattice-matched substrate that creates relatively high defect/dislocation densities in Al(Ga)N epilayers. III-nitride semiconductor materials are conventionally grown on low-cost, commercially available sapphire, SiC, or Si substrates. The key parameters of these substrates are listed in Table 1-1. Due to the large lattice mismatches and strongly different thermal expansion coefficients between Al(Ga)N and the substrates, considerable threading dislocation densities (TDD) are generated, typically on the order of 10^9 – 10^{10} cm^{-2}. The high TDD causes a drop of the internal quantum efficiency (IQE) by creating electronic states (deep levels) within the bandgap which serve as non-radiative recombination centers. The EQE, related to IQE via $\eta_{EQE} = \eta_{IQE} \times \eta_{ext}$ (η_{ext} is the light extraction efficiency), is thus significantly reduced. In addition to the above-mentioned foreign substrates, expensive low-TDD GaN or AlN bulk single crystals can be used for the growth of AlGaN heterostructures. However, AlGaN alloys possess a huge difference in in-plane lattice constant (up to 2.4%) with increasing Al composition, making the growth of device layer structures in the range of ~260 – 340 nm (mid-alloy range) on GaN or AlN substrates very challenging [18]. Therefore, cheap sapphire substrate has been widely used despite the high TDD.

Table 1-1: Physical properties of typical substrate materials measured at room temperature [7, 19-21].

Material	Lattice constant (Å)		Thermal expansion coefficients $\times 10^{-6}$ (K^{-1})		Thermal conductivity (W/cm·K)	Lattice mismatch with (%)		Thermal expansion mismatch with (%)	
	a	c	a	c		GaN	AlN	GaN	AlN
Sapphire	4.758	12.991	7.5	8.5	0.25	-16.0	-13.3	23.4	43.2
6H-SiC	3.081	15.117	4.46	4.16	4.9	-3.5	-1.0	-25.3	7.0
Si	5.43	—	3.59	—	1.5	+17.0	+19.0	-115	-60

Polarization

Almost all III-nitride UV emitters are grown in the thermodynamically stable wurtzite (WZ) phase, where the anisotropy along and perpendicular to the growth direction (c-axis) of the crystal structure results in a crystal field splitting (Δ_{CF}) of the valance band. The calculated Δ_{CF} for GaN is +38 meV and decreases with increasing Al mole fraction to −219 meV in AlN [22]. The valance band structures near the Γ-point of $Al_xGa_{1-x}N$ compounds consist of three subbands; namely, the heavy hole (HH), the light hole (LH), and the crystal field split-off hole (CH) bands as revealed in Figure 1-2 [22-24]. As Δ_{CF} decreases, the CH band moves closer to the conduction band until it becomes the topmost valance subband. The transition between the conduction band (Γ_{7c}) and the HH (Γ_{9v}) or LH (Γ_{7v}) bands are almost forbidden for $E \parallel c$, i.e., the emitted light is polarized transverse electrically (TE). In contrast, the transition between the Γ_{7c} and the CH (Γ_{7v}) band is almost prohibited for $E \perp c$, meaning the emitted light is polarized transverse magnetically (TM) [22, 25]. The polarization degree (P) can be calculated from $P = (I_{TE} - I_{TM})/(I_{TE} + I_{TM})$, wherein I_{TE} and I_{TM} represent the integrated photoluminescence (PL) intensities of TE- and TM-polarized components, respectively. For GaN, the valance subband order with increasing transition energy is Γ_{9v}, Γ_{7v}, Γ_{7v}, whereas it is Γ_{7v}, Γ_{9v}, Γ_{7v} for AlN. Therefore, the optical polarization of the emitted light changes from TE polarization to TM polarization with increasing Al composition (x) and the crossover occurs at x = 0.25 [23]. The unique negative crystal field splitting and TM polarization in conventional c-plane Al-rich AlGaN epilayers affect profoundly the light extraction efficiency of deep UV light emitters. In addition to the spontaneous polarization caused by the asymmetry of the crystal structure, III-nitride planar structures also suffer from the piezoelectric polarization induced by the tensile or compressive strain during growth on lattice-mismatched substrates, which also degrades the device performance.

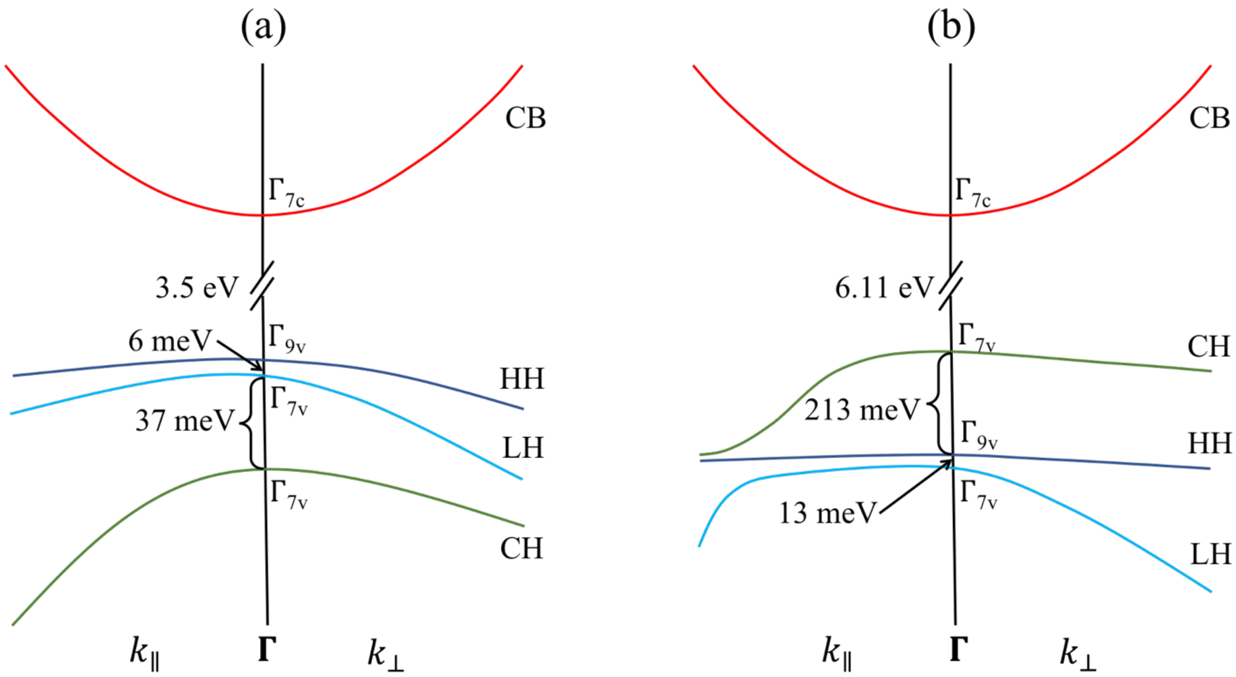

Figure 1-2: Band structures of **(a)** wurtzite GaN and **(b)** wurtzite AlN near the Γ-point.

1.1.2. Aluminum-rich AlGaN Nanowires: Promises and Challenges

The afore-mentioned fundamental challenges of AlGaN epitaxial layers can be addressed by employing nanowire structures owing to their unique properties including lateral stress relaxation, high surface-to-volume ratio, enhanced surface scattering, and size-dependent bandgap tunability. The small size of nanowires (diameter in nanometer range, typically from 2 – 200 nm) not only enables the growth of dislocation-free materials on various crystalline and amorphous substrates such as Si, SiO_2, sapphire by relaxing the strain through lateral surface [26-31] but also widens the scope of device scaling to reach true atomic level. The superior crystal quality of nanowire heterostructures has resulted in a room-temperature IQE of ~59% in AlGaN nanowire based LEDs with emission wavelength at ~340 nm [32]. Shortly after this achievement, a record IQE of 80% was realized in AlN nanowire LEDs operating at 210 nm [33]. The author also claimed that the Mg incorporation (for *p*-type doping) near the nanowire surface can be significantly enhanced by carefully optimizing the growth conditions, in particular the growth rate, leading to high Mg concentration in AlN nanowires. Moreover, the high surface-to-volume ratio of semiconductor nanowires offers more area for the emitted photons to escape, together with a lower effective refractive index compared to bulk materials as well as the strong light scattering and coupling effects, improving the light extraction efficiency [34, 35]. As described in the previous section, the emitted light of conventional AlN planar LEDs can only be extracted from the side wall due to the intrinsic TM polarization. On the contrary, the effect of light coupling and scattering amongst the nanowires can lead to the dominance of surface emission, i.e., light is extracted from the nanowire top surface (along *c*-axis), thereby enhancing the light extraction efficiency [36].

For these fundamental advantages, AlN and Al-rich AlGaN nanowires have emerged as promising candidates to realize highly efficient LEDs and LDs in deep UV range. However, there are certain challenges that need to be overcome, such as electron overflow, self-heating effect, or optical loss related to the variation of nanowire size and spacing. They require further optimization of the device structure, growth parameters as well as fabrication process. Future directions may include the exploration of large bandgap materials to improve the carrier confinement, the precise control of the nanowire diameter and spacing via selective area growth process for more efficient light emission, the use of transparent substrate for improved light extraction efficiency, and high thermal conductivity passivating materials.

1.2. Two-dimensional Layered Material Nanophotonics

Bulk transition metal dichalcogenides (TMDCs) have been used for a long time mostly as dry lubricants and industrial surface protection [37, 38], but this two-dimensional (2D) layered material family just moved to the forefront of materials science and device research with major focus on their mono- or few-layer structures after the success of graphene and recent advances in fabrication of atomically thin 2D layered materials. Compared with conventional three-dimensional (3D) photonic materials, 2D materials possess many exceptional properties such as the elimination of lattice-mismatch issue in vertical heterostructures utilizing different 2D materials due to the weak van der Walls bond between layers, the ease in integration with photonic structures, the strong light interaction even at monolayer thickness [39]. In the following sections, we will review the electronic and optical properties of TMDCs as well as their potential applications in flexible display.

1.2.1. Electronic Structure and Optical Properties

Electronic Structure

TMDCs are layered materials with the generic formula MX_2, where M is a transition metal and X is a chalcogen (S, Se, or Te). The crystal structures of these materials consist of weekly bonded sandwich layers X-M-X, with the chalcogen atoms in two planes separated by a single plane of metal atoms and the atoms in planes are hexagonally packed (Figure 1-3a). Atoms within the same plane are strongly bonded by the covalent bonding, while the weak interlayer bonding is due to van der Waals interaction that allows the mechanical cleavage of bulk crystals into individual layers through exfoliation. The bulk crystal structure can be of various polytypes depending on the metal atom coordination and stacking orders, as shown in Figure 1-3b. Metal atoms in TMDCs are six-fold coordinated and their bonding geometry can be trigonal prismatic or octahedral. In the trigonal prismatic arrangement, the two chalcogen planes are stacked directly above each other, while they are stagger in the octahedral arrangement. Bulk TMDCs are usually found in three polytypes called 2H, 3R and 1T, where 2H is the most commonly available polytype. Here, the numbers represent the number of layers in a unit cell, and the letters stand for the symmetry, which are hexagonal, rhombohedral, and tetragonal, respectively. In the scope of this thesis, we focus on group-VI TMDCs, meaning the transition metal element is either Mo or W.

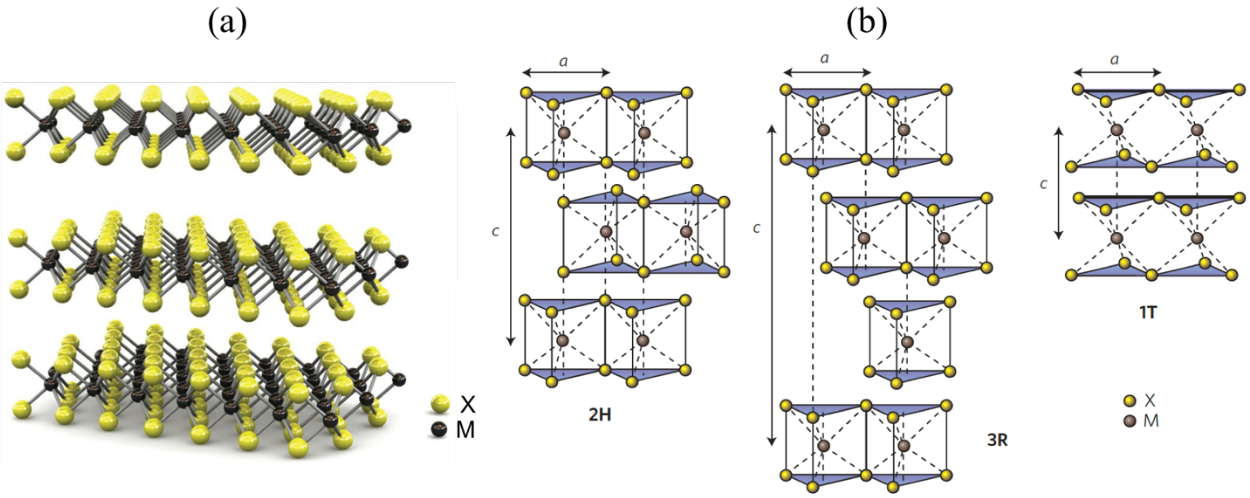

Figure 1-3: (a) Three-dimensional schematic illustration of TMDCs structure, showing the transition metal atom (M, in grey) is sandwiched between the chalcogen atoms (X, in yellow) [40]. **(b)** The bulk TMDCs can have different structural polytypes including 2H (two-layer unit cell, hexagonal symmetry, trigonal prismatic coordination), 3R (three-layer unit cell, rhombohedral symmetry, trigonal prismatic coordination), and 1T (one-layer unit cell, tetragonal symmetry, octahedral coordination) [41]. The blue-filled triangles highlight the spatial position of the chalcogen atoms within a monolayer.

In general, group-VI TMDCs are semiconducting, and their electronic structures exhibit a transition from indirect bandgap in the bulk to direct bandgap in the monolayer (Figure 1-4) [42-46]. At the same time, their bandgap also increases as decreasing the thickness of the materials due to quantum confinement in the out-of-plane direction (perpendicular to the 2D plane). Taking MoS_2 as an example, the first-principle calculations performed on the basis of density functional theory (DFT) show that bulk MoS_2 is an indirect gap semiconductor with a bandgap of ~1.2 eV, which originates from the transition between valance band maximum situated at the Γ point and conduction band minimum located halfway between Γ and K high-symmetry points [45]. As the layer number decreases, the fundamental indirect bandgap increases monotonically and becomes so high at single layer level that the material changes into a direct bandgap semiconductor [44, 45]. The direct gap occurs at the K and K′ points of the hexagonal Brillouin zone. In contrast to the variation of the indirect gap with the slab thickness, the optical direct gap at the K point stays relatively unchanged. This is because the electronic states at the K point are primarily composed of localized *d* orbitals on Mo atoms, which have weak interlayer coupling due to the middle position of Mo in the S-Mo-S layer sandwiches [44]. On the other hand, the states at the Γ point have an antibonding nature originated from p_z orbitals on the S atoms. As a result, they exhibit strong interlayer coupling, making their energies sensitive to the layer thickness.

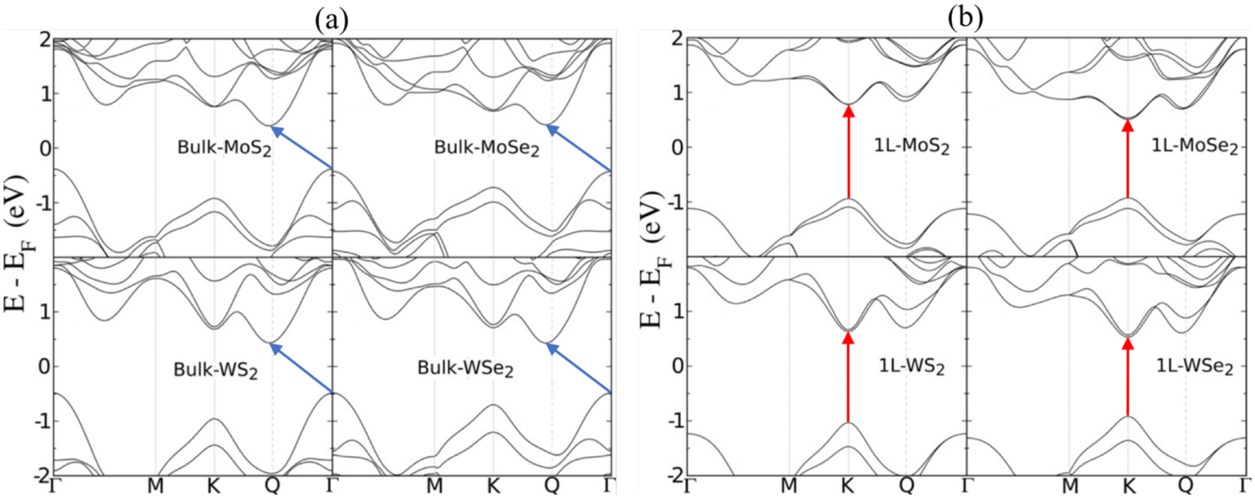

Figure 1-4: Calculated band structures of common group-VI TMDCs for bulk **(a)** and monolayer **(b)** using DFT calculations, including SOC. The blue/red arrows represent the fundamental indirect/direct bandgap for a given system, modified from [46].

The direct bandgap of monolayer MoS_2 calculated by the first-principles is 1.9 eV [45], which agrees well with the experimental data obtained from PL measurements [43, 44]. However, it is worth noticing that the theoretical results may vary depending on the calculation details [46]. DFT method is known to underestimate the bandgap of materials due to the calculated unreliable excited states [47]. It is important to add the strong spin-orbit coupling (SOC) in the calculations, especially for monolayers, to obtain a clear picture of the valance band which is split due to this effect [48, 49]. Moreover, the large exciton binding energy (0.5 – 1 eV) in TMDC monolayers arising from the reduced dielectric screening relative to bulk cases can affect the bandgap [46, 50, 51]. A more sophisticated GW approach is expected to yield better estimation of the bandgap, but results in conflicting numbers of both indirect and direct gaps [51-53].

Optical Properties

The optical properties of TMDCs are directly influenced by the electronic structures described above. For MoS_2, the indirect-to-direct bandgap transition accounts for a more than 10^4-fold enhancement of the PL quantum yield from bulk to monolayer suspended over holes in the substrate [43]. The absorption spectrum of monolayer MoS_2 shown in Figure 1-5a clearly reveals the two prominent excitonic transitions labelled as A (~1.92 eV) and B (~2.08 eV), which are associated with direct optical transitions between the maxima of spin-orbit-split valence bands and the minimum of the conduction band (marked as *v1*, *v2*, and *c1* in Figure 1-5c, respectively) located at the K-point of the Brillouin zone [43, 44, 54]. The absolute reflectance spectra of group-VI TMDC monolayers (Figure 1-5b) also reflects these features, with the two lowest energy peaks corresponding to the direct gap energies [55]. The observation of A and B resonances provides compelling evidence for strong excitonic effects in group-VI TMDC monolayers. Indeed, the extraordinarily large exciton binding energies have been calculated theoretically [48, 51, 56-58], and verified experimentally by optical spectroscopy [50, 59, 60] and scanning tunnelling spectroscopy [61].

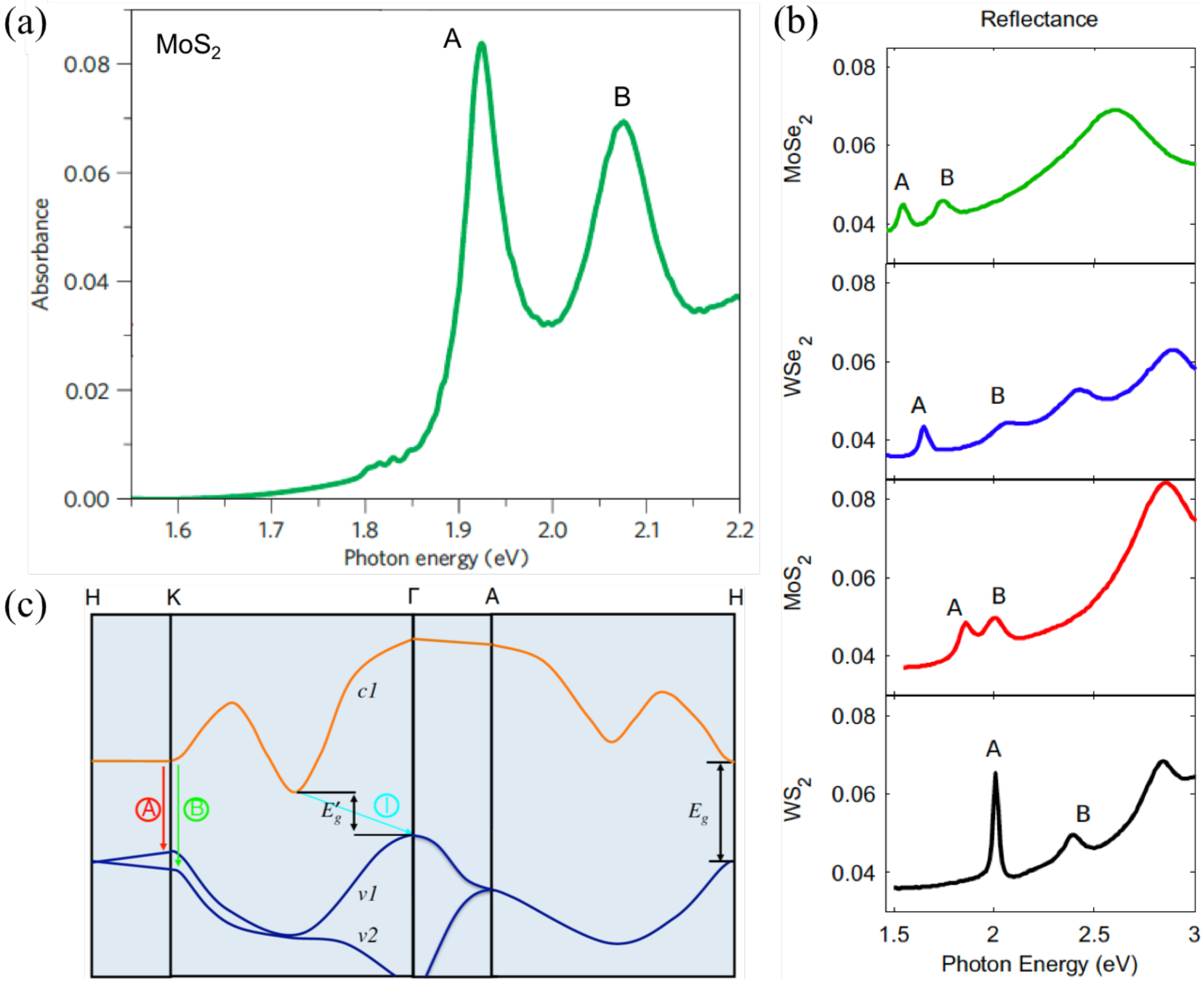

Figure 1-5: Optical properties of group-VI TMDCs. (a) Absorption spectrum of monolayer MoS_2, modified from [54]. **(b)** Experimental reflectance spectra of $MoSe_2$, WSe_2, MoS_2, and WS_2 monolayers exfoliated on fused silica [55]. **(c)** Simplified band structure of bulk MoS_2, showing two direct-gap transitions A and B (also indicated in **a** and **b**) due to spin-orbit interactions at the K-point of the Brillouin zone and indirect-gap transition I [43].

1.2.2. Two-dimensional Transition Metal Dichalcogenides and Future Opportunities in Flexible Optoelectronics

Flexible and transparent optoelectronics have attracted considerable attention in applications such as solar arrays, wearable electronics and transparent displays. These devices require the integration of various 2D material classes with different properties. 2D TMDCs, given their atomically thin architectures, hold great promises for many reasons. For instance, the direct bandgap of semiconducting TMDC monolayers make them ideal candidates for the active layers in light emitters. By carefully choosing and combining TMDC monolayers with metallic graphene and insulating hexagonal boron nitride in appropriate sequences, LEDs with tunable emission over a wide range of frequencies and extrinsic quantum efficiency of 10% was realized [62]. Owing to the large optical absorption (>10^7 m^{-1} across the visible range), the high chemical stability, and the strong light-matter interactions in atomically thin heterostructures of TMDCs, the development of extremely efficient flexible photovoltaic cells with an EQE of above 30% has been successfully demonstrated [63]. The low pretension and high elasticity of MoS_2 [64-66] are other advantages that make the material attractive for flexible electronic and optoelectronic devices.

1.3. Artificial Photosynthesis for Hydrogen Generation

1.3.1. Renewable Energy Demand

"Global warming" is not a new concept that indicates the average global temperature increase as the consequence of the accumulation of greenhouse gases, most notably CO_2. The recent increase rate of atmospheric CO_2 concentration is 2.25 parts per million per year (ppm/year) corresponding to 12 billion tons every year [67], only about half of which can be absorbed naturally. In 2017, the annual global atmospheric CO_2 was 405.0 ± 0.1 ppm, the highest in the past 800,000 years [68]. The dramatic anthropogenic buildup of heat-trapping gases from fossil fuel combustion is intensifying the greenhouse effect, leading to catastrophic changes of the global climate such as rapid sea level rise, droughts, hurricanes, tsunamis and so on. Additionally, due to the modernization and seemingly ever-larger population, our planet is facing an energy crisis with the expected worldwide energy consumption to be ~30 terawatts (TW) by 2050 [69, 70].

Therefore, it is critical to seek for carbon-free, storable and renewable energy sources to replace our reliance on fossil fuels.

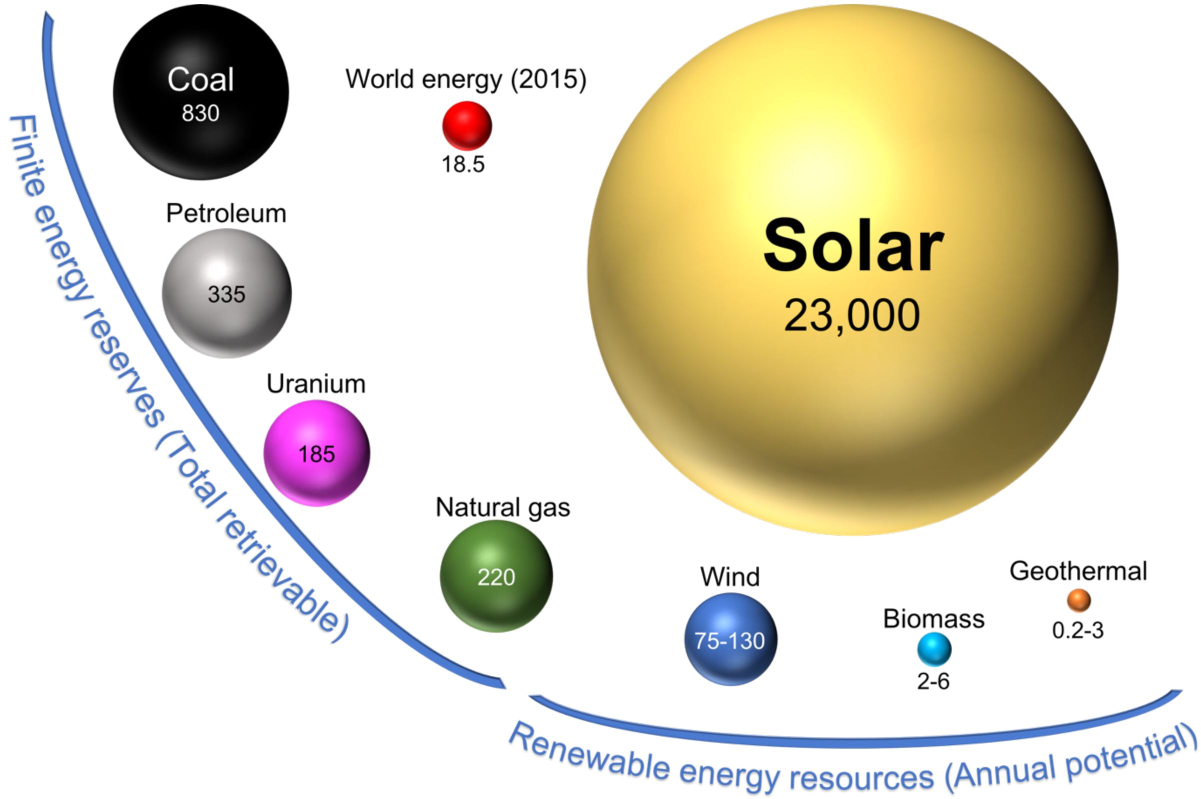

Figure 1-6: Solar energy in comparison with other energy resources. The units are in Terawatt-years (TWy). Here, the solar sphere represents the energy amount received by emerged continents only, assuming 65% losses by atmosphere and clouds [71].

Among various renewable energy options, sunlight is the most abundant and expected to be the ultimate solution to address this energy famine compared to wind, biomass or geothermal heat (Figure 1-6). The solar power (~1.2×10^5 TW) reaching the Earth's surface far exceeds the annual global energy consumption [72]. With 10% efficient solar conversion systems covering 0.16% of the land on Earth, nearly twice the world's fossil fuel consumption rate could be generated [72]. Challenges with this inexhaustible energy resource, however, are the development of economically viable technologies for its harvesting, storage, and utilization. Currently, photovoltaic (PV) is the fastest growing technology in which sunlight is converted into electricity that is difficult to store. On the other hand, solar energy stored by chemical means offers tremendous advantages in terms of storage and transportation [73]. Hydrogen, with its high energy density by mass (higher heating value of 141.9 $MJ \cdot kg^{-1}$) and environmental friendliness, is regarded as a promising carbon-free energy carrier for future [74]. Hydrogen can release energy through direct combustion in engines, as well as being utilized in fuel cells to produce electricity, wherein the only by-product is water. Evidently, the production of hydrogen via splitting water molecules (H_2O) using sunlight, the so-called artificial photosynthesis, is one of the most important approaches to solar energy conversion.

1.3.2. Solar-driven Overall Water Splitting

Mother Nature masters the utilization and storage of solar energy by developing natural photosynthesis, a two-step process. In the first step, which only occurs during the daytime, light energy is captured to split water molecules into hydrogen ions and electrons, and release oxygen as a waste product. These hydrogen ions and electrons are then used to generate Adenosine Triphosphate (ATP) and Nicotinamide Adenine Dinucleotide Phosphate (NADPH), which will be used in the second step by Calvin cycle (dark reactions) to synthesize sugars from CO_2. Artificial photosynthesis (or overall water splitting) mimics the natural process by utilizing semiconductors as light absorbers to harvest solar energy to generate electrons and holes that take part in hydrogen and oxygen evolution, respectively (Figure 1-7). The first demonstration of artificial photosynthesis was established by Fujishima and Honda (1972) who used an n-TiO_2 served as a photoanode performing the oxygen evolution reaction (OER) and an electrically connected Pt cathode performing the hydrogen evolution reaction (HER) [75]. This approach is called photoelectrochemical (PEC) water splitting, and usually requires external bias, highly conductive electrolyte and substrate for efficient carrier separation and conduction in the system. Since then, considerable efforts have been made in search for a single absorber in photocatalytic or photochemical (PC) process, where both proton reduction and water oxidation reactions take place concurrently at different sites. PC water splitting, in comparison to PEC, is low-cost and much simpler to expand the system to larger scale, although there is the associated safety issue of separating the gaseous H_2 and O_2 simultaneously generated during catalysis from the same chamber for practical applications.

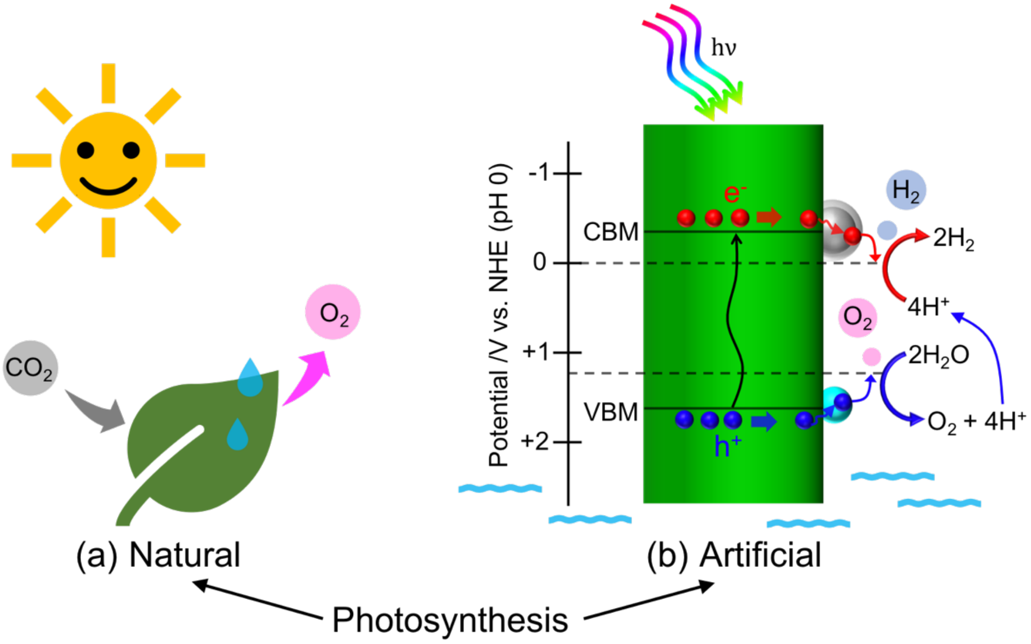

Figure 1-7: Schematic illustration of **(a)** natural and **(b)** artificial photosynthesis.

Overall water splitting (OWS) is a thermodynamically uphill reaction (i.e., energy is required to power the reaction) where the solar energy is converted into chemical energy (in the form of hydrogen) accompanied with a positive change in Gibbs free energy ($\Delta G = +237.2$ kJ/mol). The "overall" term refers to the stoichiometric ratio of the products generated simultaneously from pure water, $H_2:O_2 = 2:1$.

$$H_2O_{(l)} \rightarrow H_{2(g)} + \frac{1}{2} O_{2(g)} \quad (1)$$

As such, water splitting reaction can store 237.2 kJ/mol of energy under standard conditions (25 °C and 1 bar). In water splitting process, three steps are involved [76, 77] as described below (Figure 1-7b).

Step 1: **charge carrier generation**

Under the above-bandgap excitation ($h\nu > E_g$), the semiconductor photocatalyst absorbs photons and generate electron-hole (e^- - h^+) pairs. Photoexcited electrons move from the valance band to the conduction band while holes remain in the valance band.

Step 2: **charge carrier separation and diffusion towards the reaction sites**

The excited electrons and holes are then separated and migrate to the surface sites of the semiconductor material. This crucial process strongly affects the photocatalytic efficiency. In reality, the photogenerated carriers may recombine in the bulk or on the surface with the energy dissipated as heat due to large size of the photocatalyst and defects that operate as trapping and recombination centers, limiting the photocatalytic activity. Hence, it is important to develop highly crystalline nanostructured photocatalyst.

Step 3: **gas evolution**

In the final step, holes and electrons participate in the water oxidation and proton reduction to produce oxygen and hydrogen, respectively, through the following equations:

$$2H_2O + 4h^+ \rightarrow 4H^+ + O_2 \tag{2}$$

$$2H^+ + 2e^- \rightarrow H_2 \tag{3}$$

Thermodynamically, the primary prerequisites for the reduction and oxidation (redox) reactions to proceed are the width of the bandgap and the alignments of the conduction and valence bands. Specifically, the conduction band minimum (CBM) has to be more negative than the H^+/H_2

reduction potential (0 − 0.059 pH, V versus normal hydrogen electrode (NHE) at pH = 0), whereas the valance band maximum (VBM) needs to be more positive than the H_2O/O_2 oxidation potential (1.23 − 0.059 pH, V versus NHE at pH = 0). Therefore, the theoretical minimum bandgap energy for one-step OWS is 1.23 eV. However, sufficient overpotential is usually required for driving the redox reactions forward, while overcoming unavoidable energy losses associated with solar energy conversion [78]. Given that the energy difference between the water oxidation and proton reduction potentials is 1.23 eV, and assuming an overpotential of 0.3 eV for each half of the redox reaction, the minimum photon energy required to perform OWS becomes 1.83 eV, corresponding to a threshold wavelength of 677 nm [79].

In fact, even if the semiconductor material meets the thermodynamic requirements for water splitting, the photocatalytic efficiency can be very low due to surface recombination of the photogenerated carriers as a result of slow surface-reaction kinetic. To enhance the photocatalytic activity, co-catalysts are often loaded onto the surface of photocatalysts. The co-catalysts not only promote charge separation and suppress surface recombination by extracting photogenerated electrons and holes but they can also provide active sites/reaction sites for proton reduction and water oxidation by lowering the respective activation energies, as well as improving the stability of the photocatalyst by effectively consuming photoinduced charge carriers, particularly holes that cause photo-oxidation of the semiconductors [80, 81]. Generally, metals such as Pt, Rh, Ru, Ir, and Ni can promote the HER (reduction cocatalysts), while oxides of Co, Fe, Mn, Ru, and Ir accelerate the OER (oxidation cocatalyst) [82, 83]. It has been demonstrated that loading appropriate dual cocatalyst on the light harnessing semiconductor can significantly enhance the photocatalytic activity and stability [81, 84], and therefore is of great interest.

1.3.3. III-Nitride Nanowires as Photocatalysts for Overall Water Splitting

In terms of the solar spectrum, UV rays (below 400 nm), visible light (400 – 700 nm), and infrared light (above 700 nm) account for 3 – 5%, 42 – 46%, and 52 – 55% of the total solar energy, respectively [85, 86]. And as explained above, any photon that has wavelength longer than 677 nm is not suitable for one-step OWS. Therefore, exploring new stable, highly efficient, visible light responsive materials that satisfy stringent requirements (thermodynamic and kinetic potentials) for single-bandgap photocatalysts is among the most crucial of all challenges.

Metal nitride, specifically III-nitride, is well-known as a stable photocatalyst capable of visible-light-driven water splitting in harsh photocatalytic environment [87, 88]. An additional advantage of InGaN ternary alloy is its direct bandgap tunability to straddle the water redox potentials over a substantial portion of solar spectrum by varying the In composition, as shown in Figure 1-8 [89]. On the other hand, the use of one-dimensional (1D) nanostructures, such as nanowires, offers further advantages for hydrogen production. Nearly dislocation-free nanowires can be grown on foreign substrates (section 1.1.2), enabling the integration with low-cost Si based solar cells. The extremely large surface-to-volume ratio of nanowires provides more reaction sites, enhanced light absorption via light trapping and scattering effects [90], and hence less material is required to absorb the same amount of light. In addition, the carrier transport in the lateral direction of nanowire is no longer diffusion limited due to the small radius, making the photogenerated carriers easy to migrate to the photocatalyst-water interface and consequently reducing bulk recombination. Moreover, 1D nanowires allow control over the photocatalyst crystal plane for promoting either H_2 or O_2 evolution [91]. For all these attributes, III-nitride nanowires are the materials of choice for highly efficient OWS.

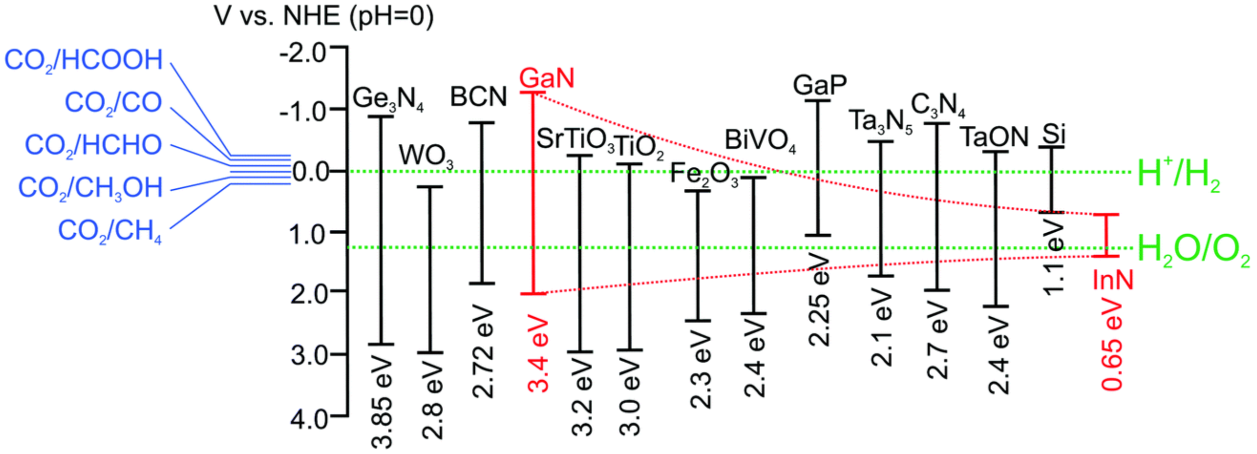

Figure 1-8: Band edge positions of commonly used photocatalysts with respect to the water redox potentials (green dotted lines). The red dotted lines represent the band edge positions of $In_xGa_{1-x}N$ as a function of In composition (0 – 1 from left to right). The reduction potentials of CO_2 to various value added products are also shown on the left. [92]

1.4. Organization of the Dissertation

Chapter 1 provides a brief overview of III-nitride semiconductors and TMDCs for applications in nanophotonics and optoelectronics. We also introduce the concept of water splitting and discuss the motivation for using III-nitride nanowires as stable, efficient photocatalysts for hydrogen production.

Chapter 2 focuses on the growth techniques of III-nitride nanowires as well as the underlying growth mechanisms. The optical and structural characterization methods are briefly summarized, together with the evaluation of photocatalytic performance.

Chapter 3 highlights our investigation of the underlying mechanism for the efficient *p*-type conduction in AlN nanowires.

Chapter 4 discusses the quantum efficiency of monolayer MoS_2 light-emitting devices. We have further demonstrated the first room-temperature lasing from 4-layer MoS_2 sandwiched between a free-standing SiO_2 microdisk and a silica microsphere that exhibits very low threshold power under continuous wave operation.

Chapter 5 reports on the development of double-band *p*-GaN/InGaN nanowire heterostructures on large Si wafer (3” in diameter) for visible-light driven overall water splitting. Subsequently, a large-scale artificial photosynthetic system with a solar-to-hydrogen conversion efficiency of ~1.1% is demonstrated under concentrated natural sunlight, followed by the discussion on the impact of light intensity on the photocatalytic activity.

Finally, Chapter 6 summarizes the dissertation work and proposes some future directions.

Chapter 2: Molecular Beam Epitaxial Growth and Characterization Methods of High Quality III-Nitride Nanowire Heterostructures

2.1. Introduction

Emerging III-nitride nanowires can be formed either by top-down or bottom-up techniques. The top-down approach starts with the planar structures and reduces its dimension to make ordered arrays of nanowires mostly through dry etching [93, 94]. Although this method is beneficial for large-scale integration, there are still numerous challenges related to significant threading dislocation densities in the starting epilayers [95], and damage resulted from etching process [96]. On the other hand, nearly defect-free nanowires can be obtained by bottom-up techniques such as chemical vapor deposition (CVD) [97, 98], chemical beam epitaxy (CBE) [99], molecular beam epitaxy (MBE) [31, 100, 101], and vapor phase epitaxy (VPE) [102]. The underlying growth mechanisms of these techniques mainly fall into vapor-liquid-solid (VLS), diffusion-induced mechanism, and selective area growth (SAG), which will be discussed in Section 2.2. Further detailed discussions on the MBE growth and characterization of III-nitride nanowire heterostructures are highlighted in Section 2.3 and Section 2.4, respectively.

2.2. An Overview of Bottom-up Nanowire Formation Techniques

The bottom-up approach enables the build-up of nearly dislocation-free nanowires with controlled properties through layer-by-layer growth from individual atoms and molecules. Although various growth techniques have been employed to achieve the nanowires with atomic perfection, they may rely on the same growth mechanism. The following sections will discuss three important mechanisms that are commonly used in the growth of III-nitride nanowires, namely, VLS mechanism, diffusion-induced mechanism, and selective area growth.

2.2.1. Catalyst-assisted Vapor-Liquid-Solid

The VLS mechanism was first proposed by Wagner and Ellis (1964) for the growth of Si whiskers from the SiI_2 or SiH_4 vapor sources [103]. In general, the VLS process involves the use of metal catalysts (impurity) such as Au, Ni, Fe, and Co that serve as nucleation centers and promote nanowire formation. The VLS growth mechanism is illustrated in Figure 2-1.

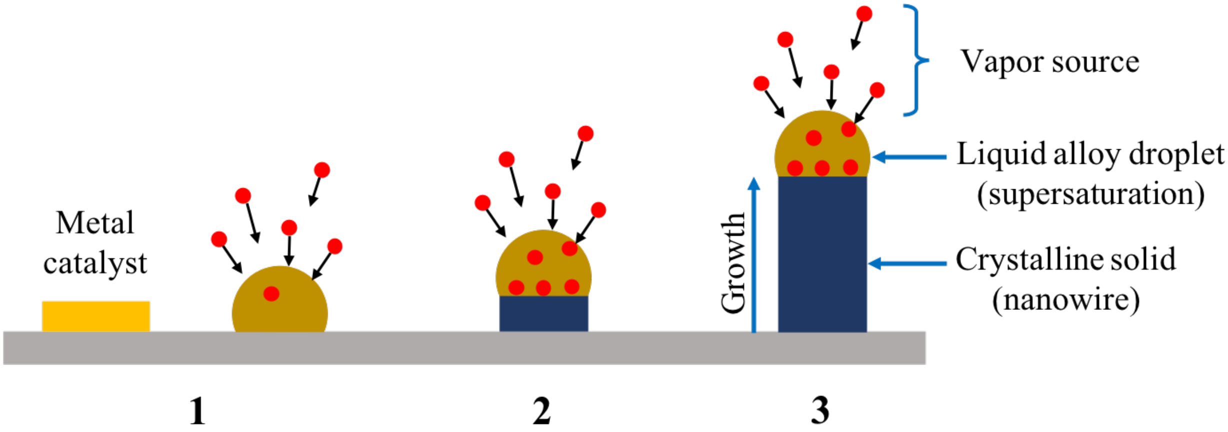

Figure 2-1: Schematic illustration of the VLS growth mechanism depicting three major steps: (1) Metal catalyst deposition, followed by the formation of liquid alloy droplet; (2) Reaching supersaturation and crystal nucleation; (3) Axial nanowire growth.

A thin layer of metal catalyst is first deposited, followed by an annealing in vapor source materials to form liquid alloy droplets. The vapor species are easily captured by the droplet surface due to its larger accommodation coefficient compared to the bare surface [104]. The species then diffuse and accumulate in the liquid phase until reaching the supersaturation, which is the thermodynamic driving force for nanowire growth. Nucleation of the crystalline structure occurs when growth species precipitate at the liquid-solid interface. The atoms arriving the crystalline surface either diffuse away or desorb back into the vapor phase while others are incorporated into the liquid droplets, leading to axial growth of the nanowires [105]. The diameter and position of nanowires are strongly dependent on the size and position of the catalyst particles, as well as growth temperature and vapor pressure. The growth of III-nitride nanowires based on VLS mechanism has been reported by using different techniques such as CVD, VPE, and on various substrates including Si, GaAs, and GaP [102, 106-108]. Despite the long nanowires synthesized in short growth duration, there remains major issue with the nanowires grown via VLS mechanism. The foreign metal catalyst atoms can diffuse into the nanowires during growth process and create deep-level trap states and stacking faults that severely degrades the optical and electrical properties [109].

2.2.2. Diffusion-induced Mechanism

Group III-nitride nanowires can also be synthesized via the diffusion-induced mechanism, which has been widely used in catalyst-free MBE technique under nitrogen-rich conditions [110-112]. In this method, no foreign metal catalyst is needed, therefore the material quality is significantly improved. Moreover, the ultra-high vacuum environment in MBE chamber helps minimize impurity incorporation, and the slow growth rate favors high crystallographic quality and atomically flat interface. Figure 2-2 represents the spontaneous formation of III-nitride nanowires by MBE technique.

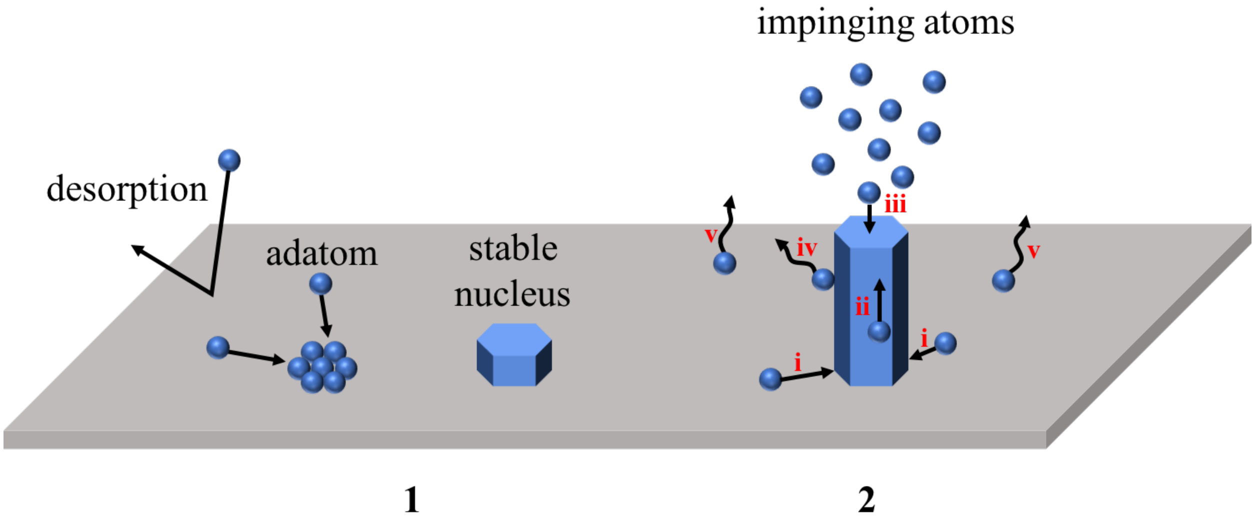

Figure 2-2: Spontaneous growth of nanowires following diffusion-induced mechanism. (1) Stable nucleus formation. (2) Axial growth of the nanowire involving five processes: (i) Substrate surface diffusion; (ii) Sidewall diffusion; (iii) Direct incorporation of the impinging atoms; (iv) Sidewall desorption; (v) Substrate surface desorption.

Adsorbed metal atoms (or "adatoms" for short) diffuse on the substrate surface and aggregate with other adatoms to form 2D nuclei and then stable nucleation sites (nanowires) [113, 114]. Due to the lower chemical potential of the top surface [101, 112], adatoms diffuse from the sidewalls toward the tip of nanowires. In addition, the higher sticking coefficient on the nanowire tips relative to that on the sidewalls [115], and in consideration of the shadow effect from adjacent nanowires, enhance the axial growth by direct incorporation of impinging atoms on the tip of nanowires. Meanwhile, some adatoms may desorb from the sidewall or substrate surface at high growth temperature. It is worth noticing that nitrogen-rich conditions not only prevent nucleation sites coalescence but also hinder layer growth to ensure well-separated nanowires [110, 113]. In some studies, a thin Ga or In seeding layer is deposited prior to the growth initiation to promote the nucleation and formation of GaN or InN nanowires [100, 116]. It has been proven that the use of *in situ* deposited In seeding layer significantly improves the structural properties and morphology of the nanowires with a non-tapered surface [100].

2.2.3. Selective Area Growth

As afore-described, the self-organization of III-nitride nanowires grown spontaneously by MBE under nitrogen-rich conditions introduces fluctuations in nanowire diameter and position due to random distribution of stable nuclei. Similar issues were observed in nanowires grown based on VLS mechanism. Consequently, the light extraction efficiency of III-nitride nanowire-based optoelectronic devices is extremely low, and the emission spectrum is usually broad. This can be overcome by selectively growing nanowires with high quality and uniformity, precise controlled size, position, and aspect ratio on pre-patterned substrate, i.e., nanowires only grow within the openings while nucleation on the mask surface is suppressed. Different types of SAG masks have been employed including SiN_x [117, 118], SiO_x [119], Ti [120-122]. Owing to the capability of well-control nanowire arrangement and morphology, the SAG approach has been extensively studied using various growth techniques, for instance, metal-organic chemical vapor deposition (MOCVD) [117], metal-organic vapor phase epitaxy (MOVPE) [123], and MBE [119-121]. In this section, we will focus on the mechanism of SAG by MBE technique of III-nitride nanowires, specifically GaN, using Ti mask.

Nitridation of the Ti mask is performed prior to the growth to prevent degradation at high temperature (usually $\geq$ 900 °C) by forming a more stable TiN layer [122]. The SAG growth of GaN nanowires involves two stages, i.e., nucleation (stage I) and shape evolution (stage II), as schematically illustrated in Figure 2-3.

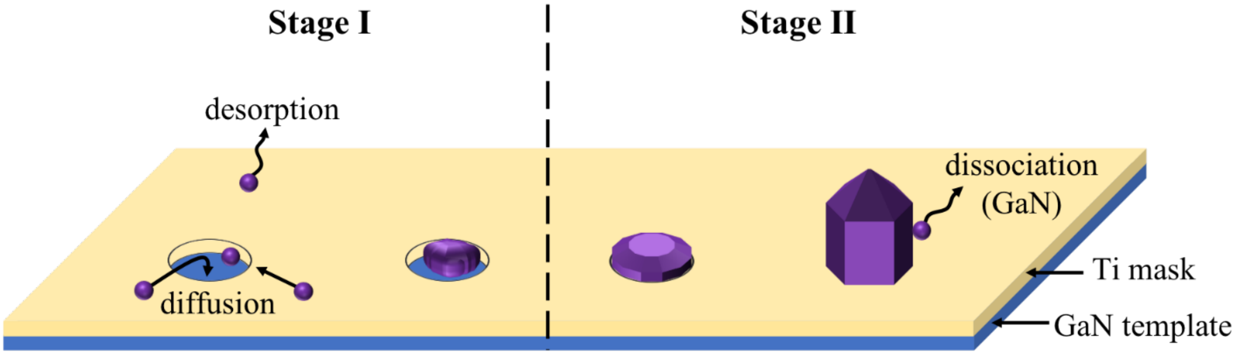

Figure 2-3: SAG growth process of GaN nanowires on GaN template covered with a Ti nanohole mask consists of two stages. Stage I: Nucleation of nanocrystal inside the nanohole. Stage II: Hexagonal GaN nanowire formation through morphological evolution.

In the first stage, Ga adatoms either desorb or diffuse into the nanoholes and nucleate a single nanocrystal inside the holes, which can be explained by the following reasons: (1) The sticking (diffusion) coefficient on the amorphous TiN is lower (higher) than that on crystalline GaN template [124]. (2) The high substrate temperature enhances the Ga surface diffusion (higher chance for Ga adatoms to reach the nanoholes) and desorption (minimize the nucleation on the mask) [120], as well as the decomposition of GaN seeds that may form outside of the nanoholes. The second stage is driven by a different mechanism that is the minimization of the total free energy per unit volume [125]. At the end of stage I, the nanocrystal with irregular shape continues to grow until it fills up the nanohole and then grows out of it laterally. The nanowire morphology undergoes multi-transition until a stable hexagonal crystal shape (*m*-faces) is formed, followed by the axial growth along the *c*-axis. Key factors in the achievement of high selectivity and crystalline quality includes the surface roughness of the mask (promotes the adatom diffusion), cleaning of the mask, mask geometry, and growth parameters (growth/substrate temperature and III/V flux ratio).

2.3. III-Nitride Nanowires Grown by MBE

The nanowire samples in this thesis were grown on Si (111) substrates by two radio-frequency plasma-assisted molecular beam epitaxy (RF-PAMBE) systems, Gen-II and GENxplor (Figure 2-4). The MBE system consists of three main vacuum chambers; namely, load-lock chamber, buffer chamber, and growth chamber. The load-lock module acts as a gate between the system and the environment and is the only one normally exposed to atmosphere. The buffer module equipped with a heated station provides an ultra-high vacuum (UHV) zone between the load-lock and growth chambers. Epitaxial growth occurs inside the growth chamber, the heart of MBE system, which is normally maintained at a background pressure on the order of $10^{-10} – 10^{-11}$ Torr in idle condition using a cryopump at 13.4 K and an ion pump at ~6200 V in GENxplor case.

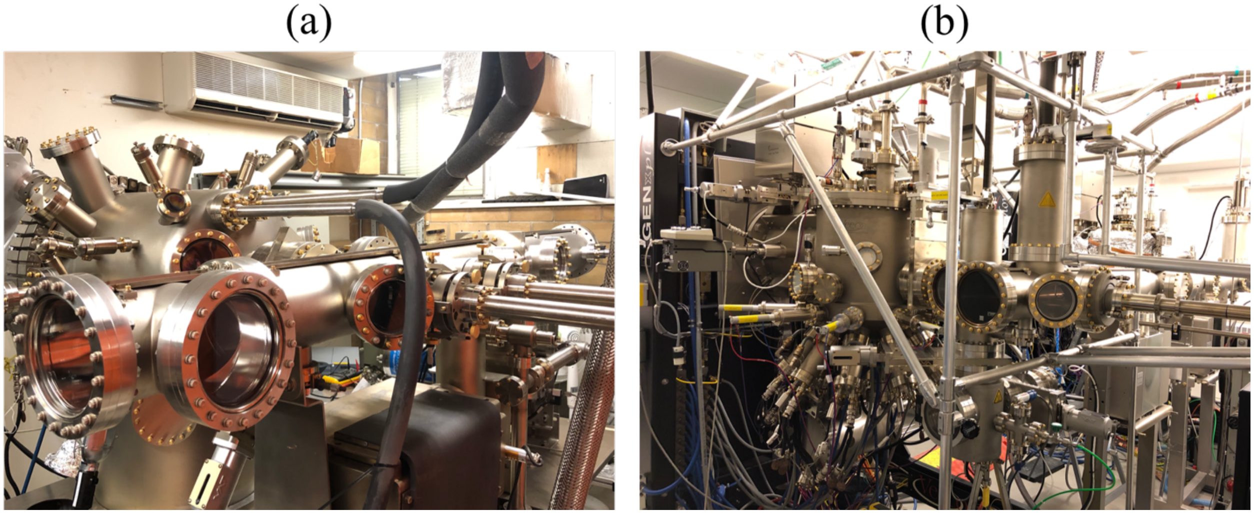

Figure 2-4: MBE systems from Veeco: **(a)** Gen-II and **(b)** GENxplor.

Prior to the epitaxial growth, the Si substrate is thoroughly cleaned with standard solvents to remove any organic contamination, followed by dipping in buffered oxide etchant (BOE 6:1) for the native oxide treatment. The substrate is then immediately loaded into the load-lock chamber of MBE system where it will be heated to 200 °C for the first degassing process. Subsequently, the substrate is transferred to the buffer chamber and degassed for the second time at 650 °C before entering the growth chamber, which is extremely clean and at very high-purity level. Group-III metal atoms (Ga, In, Al) and doping elements (Ge, Mg in Gen-II, and Si, Mg in GENxplor) are provided by thermal effusion cells. The fluxes of these elemental materials can be changed by varying the cell temperature. In RF-PAMBE systems, nitrogen radicals are supplied from the RF plasma source by breaking high purity N_2 gas to create active nitrogen plasma. The active atomic nitrogen flux can be controlled by adjusting the nitrogen flow rate and plasma power.

The growth of Mg-doped AlN nanowires was performed on 2” As-doped Si (111) wafers with resistivity in the range of $2 - 5 \times 10^{-3}$ Ω·cm in Gen-II MBE system. The detailed growth conditions will be mentioned in Chapter 3. Meanwhile, GaN/InGaN nanowire heterostructures for water-splitting application, which will be discussed in Chapter 5, were grown on larger Si (111) substrate (diameter of 3-inch) by using the modern dual-chamber GENxplor MBE system. Aside from challenges of scaling up the nanowire synthesis on larger substrate area, the growth conditions in MBE systems vary from one to another, that requires extensive calibration including the substrate temperature and the fluxes of elemental materials.

2.4. Characterization and Performance Evaluation of III-Nitride Nanowires

Experimental characterization of the material properties is of critical importance to the growth optimization and the final device performance. Numerous characterization methods have been employed during this thesis work involving scanning electron microscopy (SEM), transmission electron microscopy (TEM), PL spectroscopy, micro-Raman scattering, atomic force microscopy (AFM), X-ray photoelectron spectroscopy (XPS), and so on. Some of them will be described in the following sections.

2.4.1. Scanning Electron Microscopy (SEM)

SEM is the most efficient and fastest way to assess the morphology of the MBE as-grown nanowires. During growth optimization of a nanostructures, SEM images are used as an important instant feedback to the grower to decide the next growth conditions by providing qualitative information on the nanowire morphology, uniformity, areal density, and dimensions (diameter, length). All nanowire samples were characterized by using FEI Inspect F-50 FE-SEM equipment at an accelerating voltage of 5 – 10 kV and emission current of 5 – 10 μA.

2.4.2. Photoluminescence (PL) Spectroscopy

PL spectroscopy is a powerful method to investigate the electronic structure of materials. For example, peak positions in PL spectrum reveal the optical band gap, excitonic transitions and impurity states, while the intensity and full width at half-maximum (FWHM) can be used to assess the crystalline quality. For the growth of ternary alloys such as InGaN or AlGaN in which emission wavelength is of concern, PL spectrum provides an important feedback for the grower to adjust the incorporation of In or Al in GaN nanowires to achieve materials with desired bandgap. Since PL spectroscopy is a contactless and non-destructive technique, i.e., no electrical contacts via a complicated, time-consuming and expensive process are needed, it is an important tool to characterize the optical properties of as-grown nanowires.

PL measurements on Mg-doped AlN nanowires were carried out using a 193 nm ArF exciton laser as the excitation source in a regular PL setup. Meanwhile, the optical characterization of double-band *p*-GaN/InGaN nanowire heterostructures was performed with a 405-nm collimated diode laser system (Laserglow Technologies) in micro PL setup. The laser beam was focused on the sample through a 100× objective lens with a circular beam size of ~2 μm. The emitted light was then collected by the same objective and spectrally resolved using a high-resolution spectrometer and detected by a photomultiplier (PMT) tube.

2.4.3. Transmission Electron Microscopy (TEM)

To gain a better idea about the crystalline quality, TEM can be employed to picture the atomic structure, from which the lattice parameter, elemental composition, defects/dislocations, etc. are revealed through different operating modes. For instance, high angle annular dark field (HAADF) imaging, or Z-contrast mode, is commonly used to identify individual layers in heterostructures based on the contrast of elements with different atomic numbers (Z). The heavier (higher atomic number) the element, the brighter the region. On the other hand, high resolution TEM (HRTEM) imaging allows capturing the crystallographic structure of the sample at atomic scale.

In the course of this thesis, the structural characterization via TEM was performed by using a FEI Tecnai G^2 F20 Cryo-STEM system with a field emission gun operated at 200 kV, and a Hitachi HD2700 Cs-corrected STEM system with a cold field emission emitter operated at 200 kV and an electron beam diameter of ~0.1 nm.

2.4.4. Photodeposition of Dual-cocatalyst and Photocatalytic Water Splitting

In this dissertation, the double-band GaN/InGaN nanowire heterostructures were decorated with Rh/Cr_2O_3 (core/shell) nanoparticles and Co_3O_4 nanoparticles using photodeposition method. During unassisted overall pure water splitting reaction, Rh/Cr_2O_3 and Co_3O_4 nanoparticles perform as proton reduction co-catalyst for HER and water oxidation co-catalyst for OER, respectively. In this dissertation, 0.5 M sodium hexachlororhodate (III) (Na_3RhCl_6), 0.2 M potassium chromate (K_2CrO_4), 0.01 M cobalt nitrate hexahydrate ($Co(NO_3)_2 \cdot 6H_2O$) precursor solutions (all from

Sigma-Aldrich) were used for the deposition of Rh, Cr_2O_3, and Co_3O_4 nanoparticles on Ga(In)N nanowire surface, respectively. The deposition of Rh/Cr_2O_3 core/shell nanostructures was conducted in 20% methanol aqueous solution, while Co_3O_4 nanoparticles were photodeposited in the presence of 0.1 M potassium iodate (KIO_3, Sigma-Aldrich) in water.

Prior to the experiment, de-ionized (DI) water was purged with pure Argon (Ar) for 20 minutes. The sample was first placed in a Pyrex chamber (Kimble Chase) using a homemade polytetrafluoroethylene (PTFE or Teflon) holder, followed by adding appropriate amount of DI water and precursor solutions. The chamber was then covered with a vacuum-tight quartz lid before evacuation. Finally, the system was irradiated under 300 W Xenon lamp (Cermax, PE300BUV) for photo-assisted deposition of the nanoparticles.

For OWS reaction, the procedure was similar except only DI water was used. The evolved gases (H_2 and O_2) were manually sampled using a vacuum-tight syringe and analyzed by a gas chromatograph (Shimadzu GC-8A) equipped with a molecule sieve 5A column and a thermal conductivity detector (TCD). High-purity Ar was used as a carrier gas for the GC. The quantitative derivation of gas production rates can exhibit minor fluctuations from one water-splitting cycle to another, which can be correlated to slight inconsistencies in manual sampling of the evolved gases and/or misalignment between the light source and the sample during photocatalytic water splitting.

2.4.5. Calculation of Efficiencies in Photocatalytic Water Splitting

Solar-to-hydrogen and energy conversion efficiency:

The solar-to-hydrogen (STH) efficiency for overall water splitting under full-arc excitation can be derived from the following equation:

$$\mathrm{STH} = \frac{\mathrm{H_2}\left(\frac{\mathrm{mmol}}{\mathrm{s}}\right) \times 237\ \mathrm{kJ} \times 1000}{\rho_{\mathrm{incident\_total}}\left(\frac{\mathrm{mW}}{\mathrm{cm^2}}\right) \times A_{\mathrm{device}}(\mathrm{cm^2})} \times 100\% \qquad \mathrm{Eq.}\,(2-1)$$

Here, $\rho_{\text{incident\_total}}$ is the total incident power intensity under full arc illumination with AM1.5G filter, A_{device} is the area of the substrate covered by nanostructured photocatalysts and exposed to photo-excitation. Considering the absorption threshold of the dual-band absorber, the energy conversion efficiency (ECE) can be estimated from the following equation.

$$\mathrm{ECE} = \frac{\mathrm{H_2}\left(\frac{\mathrm{mmol}}{\mathrm{s}}\right) \times 237\ \mathrm{kJ} \times 1000}{\rho_{\text{incident\_total}}\,(\lambda_1 - \lambda_2)\left(\frac{\mathrm{mW}}{\mathrm{cm^2}}\right) \times A_{\text{device}}(\mathrm{cm^2})} \times 100\% \qquad \mathrm{Eq.}\,(2-2)$$

where $\rho_{\text{incident\_total}}\,(\lambda_1 - \lambda_2)$ is the total incident power intensity within the wavelength range $(\lambda_1 - \lambda_2)$ under full arc illumination. The incident power intensity on the sample was derived by measurements using a broadband detector (Thermopile Sensor, Newport-818P-100-55) and considering the power spectrum of the lamp and the transmittance of the optical filter, while mimicking the experimental configuration.

Chapter 3: Revealing the Underlying Mechanism of Highly Efficient p-Type Conduction in AlN Nanostructures

As discussed in Section 1.1.2, 1D nanowire structures possess many attributes that make them very promising candidates for highly efficient deep-UV light emitters, one of which is the enhanced Mg concentration in AlN nanowires. In this chapter, we will reveal the underlying mechanism for the unusually high hole concentration in Mg-doped AlN nanowires through detailed studies on the optical and electrical properties of the material grown by MBE.

3.1. Introduction

AlGaN semiconductors, with tunable bandgap energy from 6.2 eV to 3.4 eV [20], have emerged as the materials of choice for deep UV light sources, which are the *only* alternative technology to replace conventional mercury lamps for water purification and disinfection [14, 36, 126, 127]. To date, progress in this field has been fundamentally limited by the extremely poor current conduction, particularly p-type, in ultra-wide-bandgap AlGaN [8, 11, 15, 128-131]. Mg-dopant has been commonly used as p-type dopant in III-nitride semiconductors [15]. The ionization energy of Mg-dopant, however, is prohibitively large (up to 600 meV) in AlN and Al-rich AlGaN [13, 14, 132], leading to very small free hole concentration in the valence band at room temperature. Moreover, with Mg-dopant incorporation, the formation energy for nitrogen-vacancies (donors) is significantly reduced [133, 134], which, together with other defects and impurity incorporation, further compensates the presence of free holes. As a consequence, previously reported AlN epilayers only showed room-temperature free hole concentration in the range of 10^{10} cm^{-3} [13, 14, 132], which is orders of magnitude smaller than those ($\sim 10^{17} - 10^{19}$ cm^{-}

^{3}) required for efficient LED and laser operation. Attempts have been made to enhance p-type current conduction in AlGaN by exploiting the intrinsic polarization effect, incorporating the scheme of tunnel junction, and utilizing other p-type materials, but with limited success [135-138]. To date, *c*-plane AlN LEDs exhibited a turn on voltage ~20-30 V [14], significantly larger than the bandgap of AlN (~6.2 eV). The poor current conduction has also prevented the achievement of electrically pumped quantum well lasers operating in the UV-B (280-315 nm) and UV-C (200-280 nm) bands [139-143].

Recent studies have shown that efficient *p*-type conduction can be achieved in AlN and Al-rich AlGaN nanowire arrays [28, 36, 144, 145]. The resulting AlN nanowire LEDs exhibited a small turn on voltage of ~5.5 V, and electrical efficiency as high as ~85% was measured [36]. With the use of AlGaN nanowire arrays, electrically injected lasers have also been demonstrated in the UV-B and UV-C bands [35, 146]. To date, however, little is known about the charge carrier transport properties of p-type AlN nanowires [147, 148], and the underlying mechanism for the unusually efficient p-type conduction of such ultra-wide-bandgap nanostructures has remained largely unexplored. These nanostructures are grown by RF-PAMBE and are nearly free of structural defects and dislocations. In this growth process, unintentional impurity incorporation such as carbon is significantly reduced, compared to the conventional CVD or MOCVD process. Recent first-principles calculations have further shown that the Al-substitutional Mg formation energy is significantly reduced in AlN nanostructures, compared to their planar counterparts, due to the efficient surface strain relaxation [26, 145].

In this work, we have elucidated the underlying mechanism for the efficient p-type conduction in AlN nanostructures. We have performed a detailed investigation of the p-type conduction at the single nanowire level for different Mg doping concentrations by studying the temperature-dependent transfer characteristics of AlN nanowire transistors. Activation energy values in the range of ~20 – 200 meV were derived at room temperature, which is in direct contrast to the large activation energy (~500 – 600 meV) expected for Mg-doped AlN. Free hole concentrations up to ~6×10^{17} cm^{-3} were measured, which is nearly seven orders of magnitude larger than that of previously reported AlN epilayers [14]. Detailed studies suggest that such unusually high carrier concentrations stem from the efficient hole hopping conduction in the impurity band, which is consistent with the increase in hole mobility with increasing temperature. In addition, due to the enhanced Mg-dopant incorporation and the resulting Mg acceptor energy level broadening, a portion of Mg-dopants exhibits drastically reduced ionization energy, thereby enabling hole conduction in the valence band as well. The unique two-band hole conduction mechanism is further supported by the temperature-dependent measurements of the hole concentration of Mg-doped AlN nanowires. These studies provide a viable path for achieving efficient current conduction in ultra-wide-bandgap semiconductors that are critical for a broad range of applications, including deep UV LEDs, lasers, photodetectors, and modulators, and high power and high frequency transistors.

3.2. Characterization of Mg-doped Single AlN Nanowire Transistor

3.2.1. MBE Growth and Optical Properties of *p*-AlN Nanowires

In this study, catalyst-free Mg-doped AlN nanowires were grown on *n*-type Si substrate by RF-PAMBE under nitrogen-rich conditions. The use of nitrogen-rich epitaxy conditions suppresses the formation of N-vacancy related defects (donors). *In-situ* oxide desorption was performed at 805 °C in the growth chamber before the growth initiation. Prior to the growth of AlN nanowires, *n*-GaN template was grown first to better control the properties of nanowire arrays

[149]. The growth of GaN template started with a deposition of 0.6 nm Ga seeding layer before striking nitrogen plasma. The growth conditions included a RF plasma power of 350 W, a nitrogen flow rate of 1 standard cubic centimeter per minute (sccm), and Al beam equivalent pressure (BEP) of 2×10^{-8} Torr. In this study, the Mg doping concentration in AlN nanowires was varied by changing the Mg cell temperature (T_{Mg}) from 280 to 310 °C, corresponding to the Mg concentrations on the order of 10^{19} to 10^{21} cm^{-3}, which were estimated based on calibrations from Mg-doped epilayers. It is worthwhile mentioning, however, the Mg concentration in nanowires may be much lower than that of epilayers even when grown under similar conditions due to the large Mg desorption at the growth temperature and shadow effect from adjacent nanowires that hinders the incorporation of impinging Mg atoms. A high-resolution SEM image of the as-grown Mg-doped AlN nanowires is shown in Figure 3-1a.

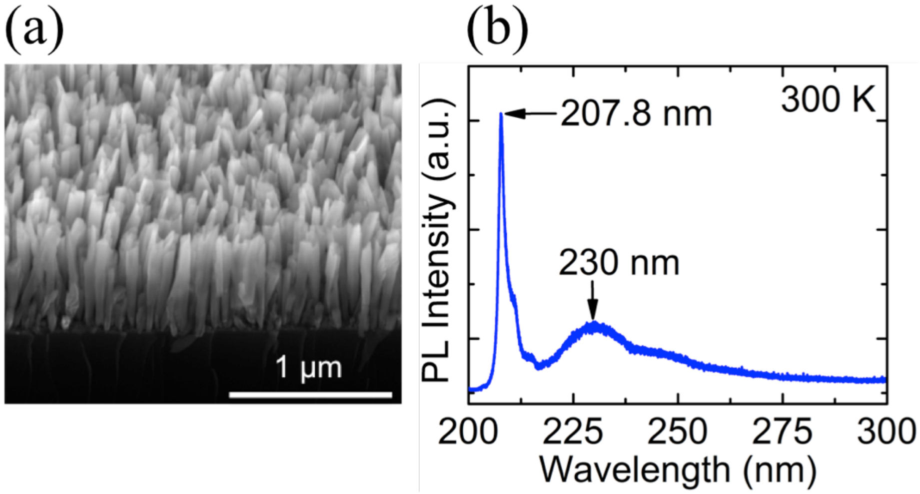

Figure 3-1: **(a)** A 45°-view SEM image of AlN:Mg nanowires grown on Si wafer and **(b)** the PL spectrum of Mg-doped AlN nanowires measured at room temperature using a 193 nm excitation laser.

The nanowires are vertically aligned on the Si substrate and oriented along the *c*-axis, with their sidewalls being the nonpolar *m*-plane. The typical nanowire lengths and diameters are ~950 nm and 100 nm, respectively. Previous reports have further confirmed that the nanowires are nearly strain- and defect-free [145, 149]. The PL characteristics of Mg-doped AlN nanowires are measured using a 193 nm excitation laser at room temperature. In Figure 3-1b, it is seen that besides the excitonic emission at 207.8 nm (5.97 eV), another low energy PL peak centered at 230 nm (5.39 eV) is also measured, which is Mg-acceptor related transition. The energy separation between these two peaks is consistent with Mg dopant activation energy (~0.6 eV) in AlN [13].

3.2.2. Electrical Properties and Discussion on the Unusually Efficient p-type Conduction in Ultra-wide Bandgap Al(Ga)N Nanostructures

Single nanowire transistors were fabricated to investigate the charge carrier transport properties of Mg-doped AlN nanowires. The as-grown AlN:Mg nanowires were dispersed onto pre-patterned Si/SiO$_x$ chips, and single AlN nanowire transistors were fabricated using standard electron-beam lithography (EBL) and contact metallization techniques. Prior to metal deposition, the nanowire surfaces were treated in hydrochloric acid (37%) for 1 minute to remove surface oxides. Metal contact layers (50/150 nm Ni/Au) were deposited using an e-beam evaporator. A rapid thermal annealing was performed at 500 °C for 2 minutes in N$_2$ ambient. An SEM image of a fabricated device and the schematic diagram of the AlN:Mg nanowire transistor are shown in Figure 3-2a and -2b, respectively.

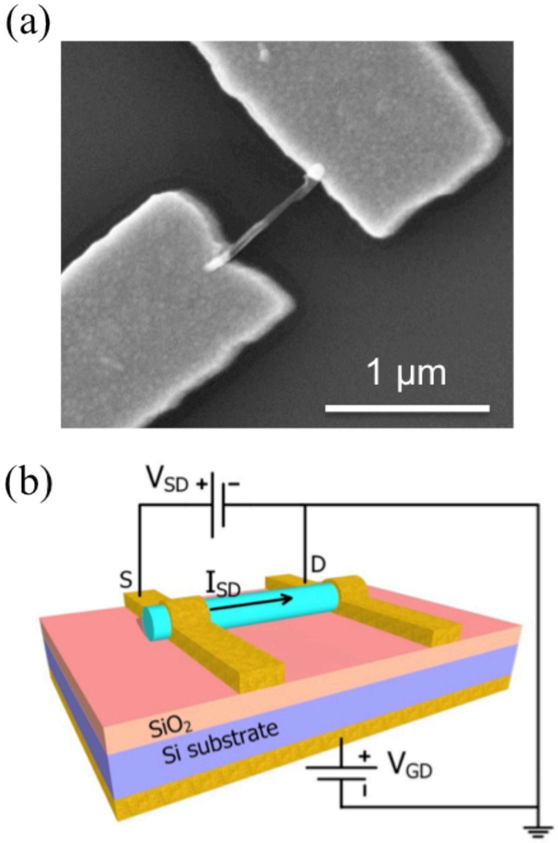

Figure 3-2: (a) The SEM image of a single AlN nanowire transistor and **(b)** the schematic diagram for electrical measurement.

We first measured the temperature-dependent resistivity of the AlN:Mg nanowires. Figure 3-3 shows the resistivity as a function of the reciprocal temperature. A distinct slope change around 600 K can be clearly seen. To further discern the underlying mechanism, we have calculated the activation energy (E_a) by utilizing the equation, $\rho(T) = \rho_0 \exp{(E_a/kT)}$, where $k = 8.617 \times 10^{-5}$ eV K^{-1} is the Boltzmann constant. E_a was found to be ~191 meV at low temperatures (below 600 K), which is nearly three times smaller compared to the Mg activation energy (~500 – 600 meV) in AlN. E_a was derived to be ~418 meV at high temperatures (above 600 K), which is consistent with the Mg activation energy in AlN, suggesting hole conduction in the valence band. It is further observed that the activation energy values decrease with the increase in Mg doping incorporation. Activation energy in the range of 20 – 30 meV has been measured for more heavily Mg-doped AlN nanowires [148]. The small activation energy measured near room temperature indicates hole hopping conduction in the impurity band. This two-band picture, with more detailed discussions later on, can also explain the temperature-dependent mobility and hole concentration rather well. It is also worth noting that similar electrical transport behavior has been observed in p-type InGaN [150], GaN [16], and AlGaN [151], with the increase in transition temperature as the bandgap energies become larger, i.e., ~250 K for p-type InGaN and GaN and ~500 K for p-type $Al_{0.7}Ga_{0.3}N$. In the present study, ~600 K was measured for AlN.

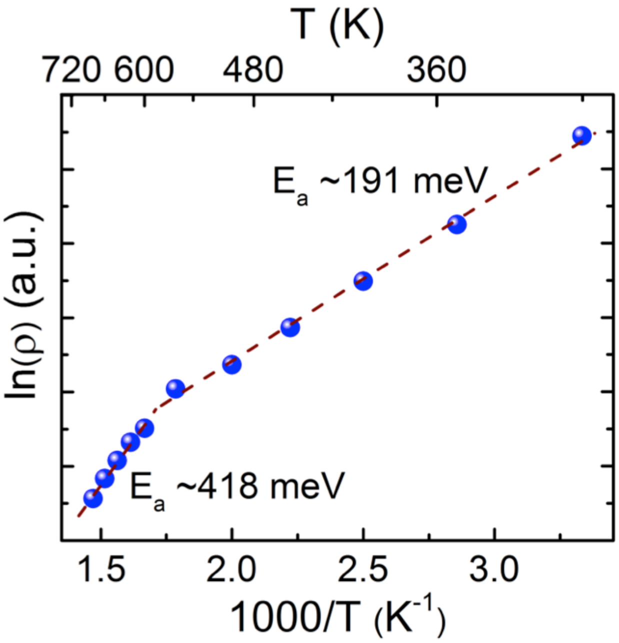

Figure 3-3: Variation of the resistivity as a function of inverse temperature for the Mg-doped AlN nanowire sample with relatively low Mg concentration (estimated to be on the order of 10^{19} cm^{-3}).

We have further investigated the back-gate voltage dependent carrier transport characteristics. Illustrated in Figure 3-4a are the back-gate voltage dependent source-drain current (I_{SD}) versus source-drain voltage (V_{SD}) collected from a device with the low-doped sample (estimated Mg concentration of ~10^{19} cm^{-3}) at 500 K. It is seen that I_{SD} increased linearly with the increase in V_{SD}, indicating the formation of Ohmic contact. Furthermore, the channel conductance (i.e., I_{SD}/V_{SD}) exhibited a dramatic increase as more negative back-gate voltages were applied, providing an unambiguous evidence for the p-type conduction of the present AlN:Mg nanowires [147, 150, 152, 153]. The transfer characteristic, i.e., the $I_{SD} - V_{GD}$ dependence is shown in Figure 3-4b at V_{SD} = 0.2 V. A clear p-type conduction feature can be seen. Moreover, it is noticed that I_{SD} reaches the minimum at a positive V_{GD} (~0.5V), indicating a p-type conduction at zero back-gate voltage. Similar behavior was observed in many other AlN nanowire devices (not shown).

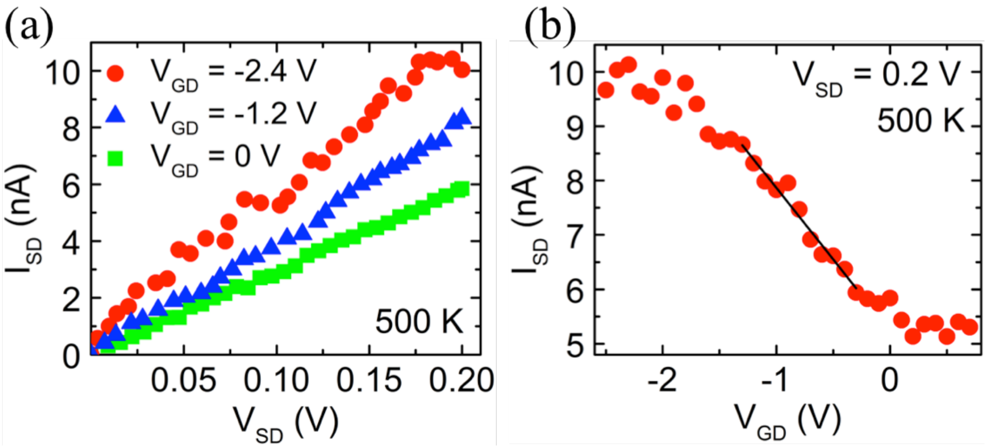

Figure 3-4: The field-effect characteristics of AlN:Mg nanowire transistor (estimated Mg concentration ~10^{19} cm^{-3}) measured at 500 K. **(a)** I-V characteristics. **(b)** The $I_{SD} - V_{GD}$ curve at a fixed V_{SD} = 0.2 V clearly shows p-type conduction. Similar behavior was observed at other doping levels.

From the slope of the transfer characteristic shown in Figure 3-4b at negative back-gate bias, we have calculated the field-effect free hole mobility μ from 300 to 690 K by the following equation:

$$\mu = \frac{g_m L^2}{C V_{SD}} \qquad \text{Eq.}\,(3-1)$$

where $g_m = \partial I_{SD}/\partial V_{GD}$ is the nanowire transconductance, determined by the best linear fit to the

$I_{SD} - V_{GD}$ curve, L is the channel length (i.e., distance between the source and drain contacts), and C is the total capacitance, which is defined as [153]:

$$C = \frac{2\pi\varepsilon\varepsilon_0 L}{\cosh^{-1}(1 + t_{ox}/a)} \qquad \text{Eq.}\,(3-2)$$

where ε = 3.9, t_{ox} = 350 nm (SiO_2 thickness), and nanowire radius a is ~50 nm. With a channel length of 700 nm, the obtained value for hole mobility is ~0.67 $cm^2/V{\cdot}s$ at room temperature, which is reasonably close to that measured for AlN epilayers previously [14]. Compared to the theoretical values of the hole mobility in AlN (~14 $cm^2/V{\cdot}s$ at 290 K), the hole mobility in AlN nanowires is limited by surface scattering [154]. With the increase in Mg doping concentration, the total mobility was decreased from ~0.67 $cm^2/V{\cdot}s$ to ~7.7×10^{-4} $cm^2/V{\cdot}s$ at room temperature, consistent with the enhanced ionized impurity scattering.

The hole mobility of the low-doped sample is almost invariant with temperature from 300 – 400 K, then increases with the increase in temperature until 600 K, followed by a decrease (Figure 3-5a). This temperature-dependent carrier mobility does not follow conventional semiconductors wherein the conduction is through either conduction or valence band. For conventional semiconductors, the mobility follows $\mu \propto T^{3/2}$ due to ionized impurity scattering at low temperatures, and $\mu \propto T^{-3/2}$ due to phonon scattering at high temperatures [155]. Here, it is seen that the phonon scattering explains the high temperature (above 600 K) mobility well, while the low temperature (below 600 K) mobility shows a much larger temperature exponential (1.9 for Mg concentration of 10^{19} cm^{-3}, and 11.3 for Mg concentration of 10^{21} cm^{-3}).

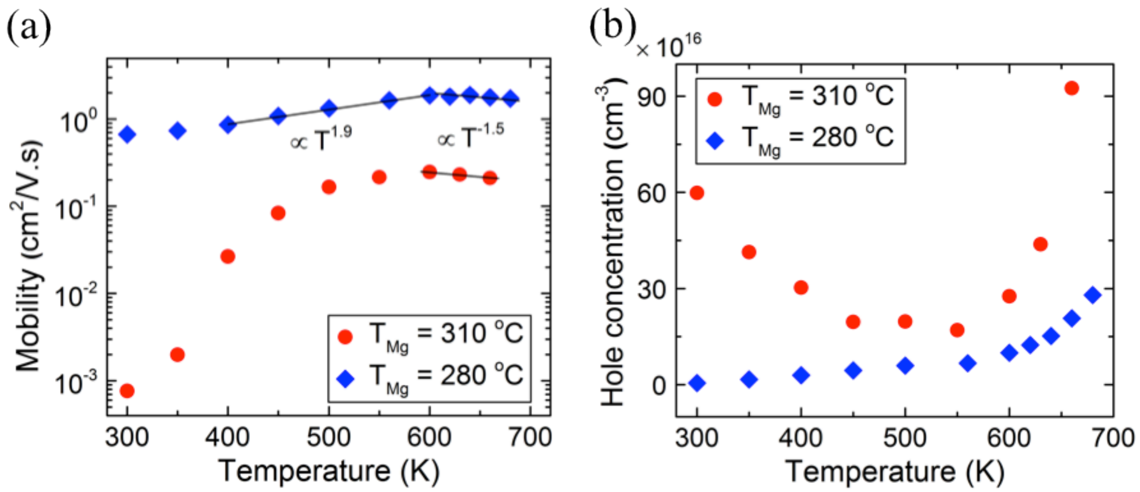

Figure 3-5: (a) Plot of the derived mobility of two AlN:Mg samples at different Mg concentrations as a function of measurement temperature. Blue diamond and red dot are for low-doped (Mg cell temperature of 280 °C) and high-doped (Mg cell temperature of 310 °C) samples, respectively. **(b)** Free hole concentration versus temperature for these two samples.

To understand the underlying reason, we adopt the previously introduced two-band conduction mode [156-158]. Impurities in semiconductors are generally described as localized energy levels with respect to conduction or valance band at low doping concentrations. As the doping concentration increases, impurities start to interact, and the probability of carrier (hole in the present study) hopping from one state to adjacent state increases, accompanied by a reduction in the thermal activation energy for such a conduction. This is consistent with our previous study, which showed a very small activation energy of ~23 meV for heavily Mg-doped AlN nanowires [148]. When the average separation r between the impurity atoms is comparable to the radius r^* of hydrogen-like impurity, the formation of an impurity band is expected [159, 160]. Here, $r = (3/4\pi N)^3$, and $r^* = \left(\frac{\varepsilon_s}{\varepsilon_0}\right)\left(\frac{m_0}{m^*}\right) 0.5 \times 10^{-8}$ cm. For AlN, taking the relative dielectric constant $\varepsilon_s/\varepsilon_0$ around 9 and reduced mass m^* ~$0.3m_0$, it requires an impurity concentration N on the order of 10^{18} cm^{-3} to form an impurity band. For the lowest Mg-doped sample in the present study, the doping concentration is estimated to be on the order of 10^{19} cm^{-3}, which can lead to the formation of a Mg impurity band. Due to the finite overlap of the localized energy levels, the hole mobility in the impurity band is expected to be smaller compared to that in the valence band. In addition, since impurity band conduction dominates at low temperatures due to the associated small activation energy (Figure 3-3), it thus explains the large temperature exponentials in the temperature-dependent mobility values below 600 K. This argument is further supported by the increased low-temperature exponential as the Mg doping concentration increases.

Free hole concentrations were further derived from the following equation,

$$p = \frac{L}{e\mu[(R_{tot} - R_{cont})(\pi a^2)]} \qquad \text{Eq.}\,(3-3)$$

wherein R_{tot} and R_{cont} denote the total resistance and contact resistance, respectively. For the low-doped sample, the hole concentration is ~5.4×10^{15} cm^{-3} at room temperature and shows a small increase with temperature. The hole concentration increases dramatically with temperature above 600 K, due to the thermal ionization of Mg dopants. Such a temperature-dependent behavior is consistent with impurity band conduction and valence band conduction at low and high temperatures, respectively [157]. The significant effect of impurity band conduction is more evident in the high-doped sample. The hole concentration reaches as high as 6×10^{17} cm^{-3} at room temperature, which is nearly seven orders of magnitude higher than previously reported values (~10^{10} cm^{-3}) for Mg-doped AlN epilayers. Moreover, the hole concentration exhibits a *decreasing* trend with increasing temperature in the range of 300 K to 550 K, followed by an increase with temperature from 550 K to 650 K. Such an anomalous temperature-dependent hole concentration can be well explained by the afore-described two-band conduction model. The hole concentrations in the impurity and valence bands exhibit different temperature-dependent behaviors: The effective hole concentration in the impurity band decreases with temperature, whereas hole concentration in the valence band increases with temperature. Consequently, the dominance of impurity band conduction near room temperature leads to a decrease in hole concentration from 300 K to 550 K. With further increasing temperature, the contribution from holes in the valence band becomes more important, and the hole concentration shows an increasing trend with temperature. Such a unique temperature-dependent hole concentration has been previously measured in GaN in a lower temperature range [157, 158]. For practical application in LED and laser devices, the Mg-dopant incorporation in AlN and Al-rich AlGaN will need to be carefully optimized to achieve minimum resistivity.

Factors that contribute to such unusually efficient p-type conduction in ultra-wide-bandgap Al(Ga)N are described as follows: (i) Al(Ga)N nanostructures exhibit drastically reduced defect densities, compared to Al(Ga)N epilayers. Moreover, the use of plasma-assisted MBE can significantly reduce impurity incorporation, such as carbon, compared to Al(Ga)N grown by CVD or MOCVD. (ii) The use of nitrogen-rich epitaxy conditions suppress the formation of nitrogen-vacancy related defects (donors) in Al(Ga)N. (iii) Recent first principles calculations have revealed that the Al-substitutional Mg formation energy is drastically reduced in Al(Ga)N nanowire structures, compared to that in Al(Ga)N epilayers, thereby leading to significantly enhanced Mg-dopant incorporation and the formation of Mg impurity band in Al(Ga)N nanostructures [145, 161]. (iv) Another critical advantage associated with the enhanced Mg-dopant incorporation is that a portion of the Mg-dopants have significantly reduced ionization energy, due to the band tailing effect and the significantly broadened Mg energy levels [148], which are evidenced by the partial overlap between the excitonic emission and the Mg acceptor related radiative recombination transition peaks shown in Figure 3-1b.

3.3. Conclusion

In conclusion, we have identified the formation of a Mg impurity band and revealed the underlying mechanism for the unusually efficient p-type conduction in ultra-wide-bandgap Al(Ga)N nanostructures. Through detailed studies on the temperature-dependent electrical transport characteristics of Mg-doped AlN nanowires via back-gate field-effect transistor configuration, we have further measured unique charge carrier transport properties, including a very small activation energy for electrical conductivity, large free hole concentrations, and a significant increase in mobility with temperature, which are well explained by the presence of a Mg impurity band and the efficient hole hopping conduction. This work provides important insight into the current conduction of ultra-wide-bandgap semiconductor materials and further offers a viable path to achieve high efficiency deep UV optoelectronic devices that were not previously possible.

Chapter 4: MoS_2-based Light-Emitting Devices

One of the most critical challenges limiting the performance of light emitters is high defect and dislocation densities due to lattice mismatch between epilayers and the substrates (see Section 1.1.1). Beside 1D nanowires with the offer of lateral stress relaxation, 2D layered material family, such as MoS_2, can also eliminate this issue owing to the weak van der Walls bond between layers as mentioned in Section 1.2. This chapter will discuss the quantum efficiency of monolayer MoS_2 light-emitting devices, and further demonstrate MoS_2-based optically pumped lasers operating at room temperature.

4.1. Introduction

The transition metal dichalcogenide semiconductors, such as molybdenum disulfide (MoS_2), are indirect bandgap in their bulk case with a transition to direct-gap semiconductors in a monolayer limit due to significant quantum confinement effect [43, 44]. In the last decade, there have been extensive theoretical and experimental studies of the optical properties and the electronic band structure of TMDCs [43-45, 49]. Due to high optical absorption [43, 162], strong band-to-band PL emission [44], large exciton binding energy [57], and relatively high carrier mobility [163, 164], 2D TMDCs are promising candidates for next generation nanophotonics and optoelectronic devices. Mono- and few-layer materials possess extremely short radiative carrier lifetime (~100 ps) [165], nearly an order of magnitude smaller than that in the state-of-the-art quantum well devices operating in the same wavelength range, suggests the possibility of achieving light emitting devices with high modulation bandwidth. Moreover, compared to conventional group III-V quantum well lasers, the large refractive index of 2D TMDCs (~6-7 in the visible range) can significantly increase the optical confinement in the laser active region. The optical gain can be further enhanced by the strong Coulomb interactions due to the vertical confinement and the reduced dielectric screening in these materials. While extensive research has been devoted to exploring their properties and incorporating them into functional devices, there is still a vast lack of fundamental understanding of the device performance. The realization of a room-temperature 2D TMDC based semiconductor laser has also not been reported.

In Section 4.2, the maximum achievable quantum efficiency of the emerging monolayer light-emitting devices and the comparison with that of GaN quantum well LEDs, the presently dominant technology for solid-state lighting, will be discussed. Through temperature- and power-dependent PL measurements, the radiative and various nonradiative recombination processes in single layer (1L) MoS_2 have been investigated. Section 4.3 will follow by demonstrating an optically pumped 2D MoS_2 lasers operating at room temperature. In this work, four-layer (4L) MoS_2 has been used as the gain medium in a vertically coupled, free-standing SiO_x microdisk and microsphere cavity, which can significantly enhance the coupling between the MoS_2 gain medium and the optical cavity modes, leading to ultralow threshold lasing under continuous wave operation at room temperature.

4.2. Insights into The Quantum Efficiency of Monolayer MoS_2 Light Emitting Diodes

The monolayer MoS_2 flakes were prepared from their natural bulk via mechanical cleavage on Si/SiO_x substrates. The flake was excited by a 514 nm laser source with power ranging from 1 μW to 10 mW under a 50× long working distance objective lens (spot size of 2 μm) in a confocal microscopy setup that enabled us to locate and excite the flakes at the same spot. The temperature-dependent measurements were carried out under N_2 ambient inside a cryostat, which is capable of operating in the temperature range of 83 K to 500 K. Prior to the measurements, the samples were annealed at 200 °C for 10 minutes to remove the moisture, and then cooled down to the measurement temperature.

4.2.1. Temperature-dependent Photoluminescence Measurements

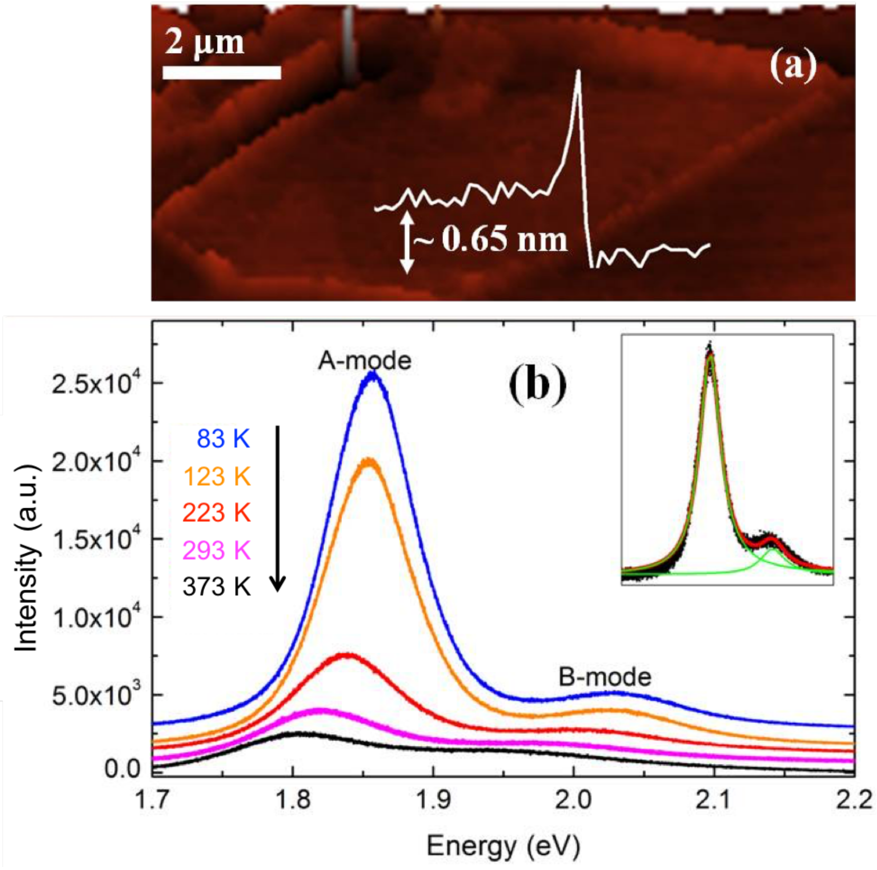

Figure 4-1: (a) AFM image of a monolayer MoS_2 flake with an embedded thickness profile. **(b)** Typical temperature-dependent PL spectra measured from 83 K to 373 K with an example of a Lorentzian fit (inset).

The AFM image embedded with a thickness profile of a large MoS_2 flake (Figure 4-1a) confirms the average thickness of ~0.65 nm, indicating single layer MoS_2. Two prominent transitions at 1.83 eV (A-mode) and 1.99 eV (B-mode) are clearly observed from the PL spectrum of a 1L MoS_2 at room temperature, as shown in Figure 4-1b, attributed to two direct excitonic transitions at K (K′) points at the corners of the hexagonal Brillouin zone [44]. The shape of both modes remained symmetric and exhibited redshifts and broadenings with increasing the temperature in agreement with previous study [166]. The PL spectra at all temperatures can be precisely fitted using Lorentzian curves, with an example shown in the inset of Figure 4-1b. Figure 4-2a plots the peak shifts of both modes with temperature, which can be described using the Varshni's semi-empirical equation [167]:

$$E_g(T) = E_g(0) - \frac{\alpha T^2}{T + \beta} \qquad \text{Eq. } (4-1)$$

Where α and β are the characteristics of the given material. The fitting parameters used for each mode are $E_g(0)$ = 1.868 ± 0.003 eV, $\alpha = (2.2 \pm 0.7)\times10^{-4}$ eV/K, β = 250 ± 100 K (A-mode), and $E_g(0)$ = 2.053 ± 0.003 eV, $\alpha = (5 \pm 1)\times10^{-4}$ eV/K, β = 460 ± 200 K (B-mode).

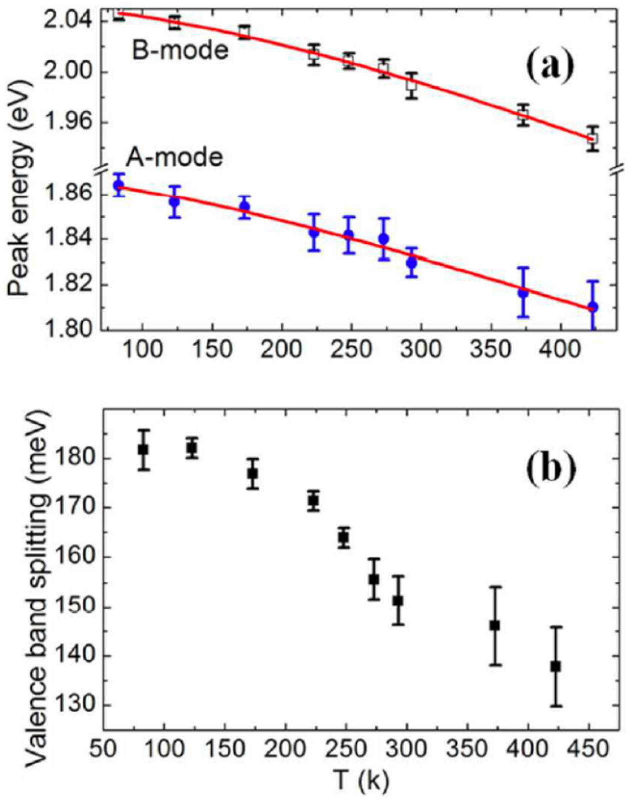

Figure 4-2: (a) Peak energy variation with temperature for A-mode and B-mode. The solid lines are fitting curves by using Varshni's equation. **(b)** Valence band splitting as a function of temperature. [168]

It is of interest to note that α is larger by a factor of two for B-mode compared to the A-mode, indicating a larger shift of the B-mode than A-mode with temperature. This is due to a reduction of the valence band splitting from 182 meV to 137 meV with increasing temperature from 83 K to 423 K (shown in Figure 4-2b).

4.2.2. ABC Model and Determination of Quantum Efficiencies

In the following, we first describe ABC model and then present the experimental data to determine the radiative and nonradiative coefficients and IQE. The steady state carrier generation/recombination rate (G), IQE and integrated PL intensity (I_{PL}) can be expressed as:

$$G = An + Bn^2 + Cn^3 \qquad \text{Eq. } (4-2)$$

$$IQE = \frac{Bn^2}{G} \qquad \text{Eq. } (4-3)$$

$$I_{PL} = \gamma B n^2 \qquad \text{Eq. } (4-4)$$

where A, B and C represent the nonradiative Shockley-Read-Hall (SRH), radiative bimolecular, and nonradiative Auger recombination coefficients. n is the photoexcited carrier (electron) concentration. γ is a constant determined by the sample and the measurement setup details. On the other hand, G can be separately determined from the experimental parameters, i.e., laser power (P_{laser}), Fresnel reflection coefficient (R), absorption coefficient (δ), area of the laser spot (A_{spot}), and excitation energy ($h\nu$), by using the following equation [169]:

$$G = \frac{P_{laser}(1-R)\delta}{A_{spot} h\nu} \qquad \text{Eq. } (4-5)$$

R = 0.6 was calculated from Fresnel equation (normal incidence) using the refractive index of ~8 [170]. In our model, we used δ ~ 0.05 per layer [43]. From Eq. (4-2), $\sqrt{B}n$ can be expressed as a function of ($\frac{A}{\sqrt{B}}, \frac{C}{B^{1.5}}, G$), and therefore the external quantum efficiency (EQE $\propto I_{PL}/G = \gamma \times$ IQE) can be defined as a function of $(\frac{A}{\sqrt{B}}, \frac{C}{B^{1.5}}, \gamma, G)$. $\frac{A}{\sqrt{B}}, \frac{C}{B^{1.5}}$ and the constant γ will be determined as fitting parameters, while G was calculated from Eq. (4-5). The value of $\frac{A}{\sqrt{B}}$ and $\frac{C}{B^{1.5}}$ only depends on temperature.

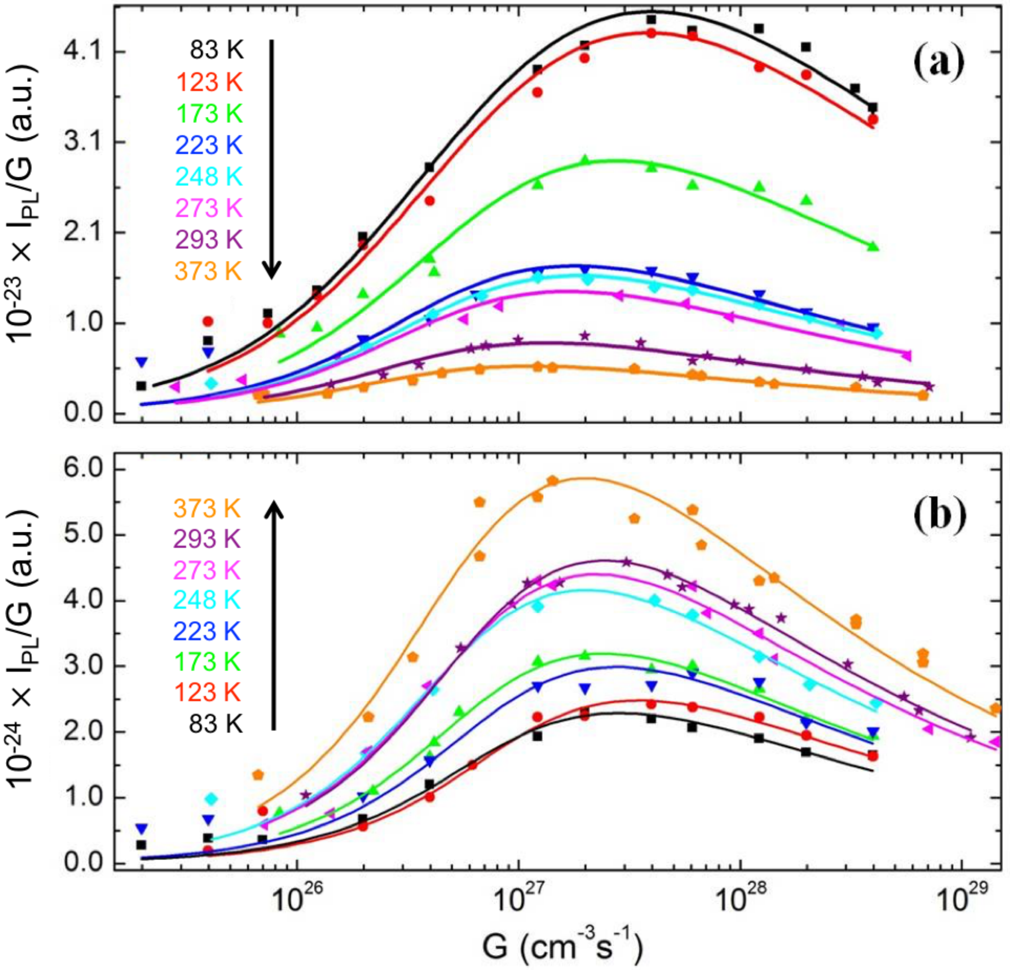

Figure 4-3: Plot of the relative external quantum efficiency (EQE ∝ I_{PL}/G) and IQE as a function of carrier generation rate (G) for **(a)** A-mode and **(b)** B-mode.

Figure 4-3 shows the relative external quantum efficiency (I_{PL}/G) and the IQE as a function of G for both modes. The fitting curves are nearly in perfect agreement with the experimental results at all temperatures. As can be seen in both Figure 4-3a and 4-3b, the external quantum efficiency increases with increasing carrier injection, which is due to the saturation of nonradiative SRH recombination. However, at high carrier injection conditions, the efficiency droop is clearly observed, suggesting the dominance of nonradiative Auger recombination. We have noticed different trends in the variation of internal quantum efficiencies of A-mode and B-mode with temperature at a given carrier generation rate. Specifically, the IQE of A-mode decreases from 45% to 5.2% with increasing temperature from 83 to 373 K, while that of B-mode exhibits an abnormal increase from 2.1% to 6% in the same temperature range. The room-temperature IQE of the A and B modes in 1L MoS_2 are 8.3 % and 4.5 %, respectively.

We have further estimated the value of radiative and nonradiative recombination coefficients in relation with temperature. First, we have evaluated the SRH recombination coefficient (A). This nonradiative recombination process is primarily related to the defects located at the free surface of MoS_2 and its interface with SiO_2 substrate. Thus, SRH recombination cannot be diffusion limited in 1L MoS_2, and hence would have extremely weak temperature dependence. This is consistent with the recent transient absorption spectroscopy observations that the thermal induced carrier diffusion has negligible effect on carrier recombination [171]. We consider A = 10^{10} s^{-1} and assumed it to be temperature-independent in this study.

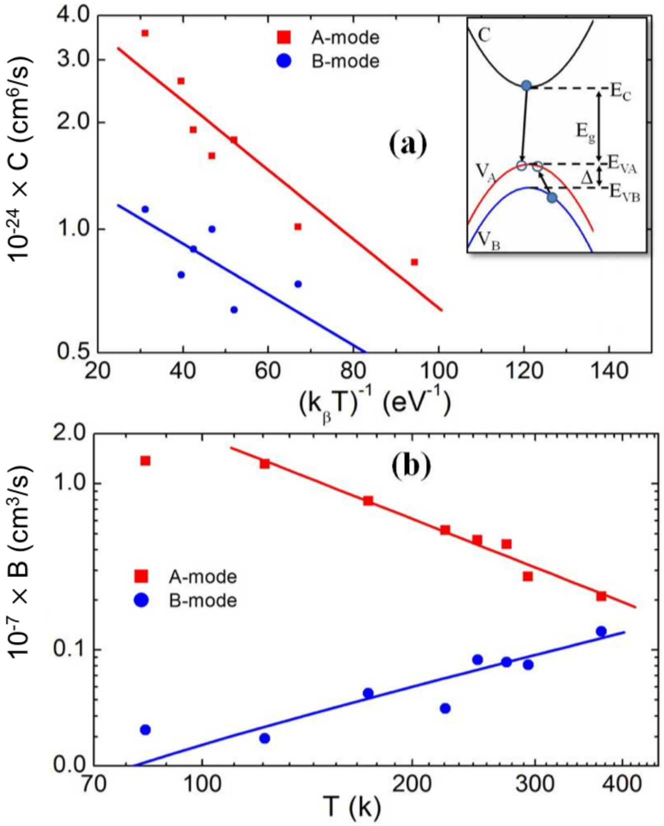

Figure 4-4: **(a)** Plot of the calculated Auger recombination coefficient as a function of $1/(k_\beta T)$. The inset illustrates a possible Auger recombination pathway in a 1L MoS_2. **(b)** Plot of the calculated radiative recombination coefficient as a function of temperature.

The variation of Auger coefficient (C) as a function of $(k_\beta T)^{-1}$ is shown in Figure 4-4a, and is well-fitted by function $\exp(-E_a/k_\beta T)$ (solid lines), as expected for a band-to-band Auger recombination [172]. The activation energy E_a was derived to be 22 ± 3 meV for A-mode and 16 ± 5 meV for B-mode. For a direct band-to-band Auger recombination, E_a should be on the order of the bandgap, and therefore our observed low activation energy indicates the dominance of phonon-assisted Auger recombination (indirect recombination process). Figure 4-4b plots the radiative recombination coefficient (B) as a function of temperature. It is seen that B decreases with the temperature according to $T^{(-1.6\pm0.2)}$ for A-mode; however, it increases for B-mode as $T^{(0.9\pm0.2)}$ (indicated by solid fitting lines in Figure 4-4b). Our observed temperature-dependence of B coefficient of A-mode is consistent with the behavior expected for a typical bulk semiconductor ($B \propto T^{-1.5}$) [173, 174], while the increase in B for B-mode is rather anomalous. To explain this unusual trend, we consider the involvement of the two valence sub-bands in the Auger recombination pathway $CV_AV_BV_A$, as shown in the inset of Figure 4-4a. The process results in the annihilation of an electron (in the conduction band) and two holes (in the valance sub-band V_A), while leaving a hole in the valance sub-band V_B. This model also explains our observed increase in IQE of B-mode with temperature. The transition from conduction band to valence band is proportional to the joint density of states weighted by the corresponding hole occupation number which increases with increasing temperature due to the proposed Auger process, leading to the enhancement of IQE of B-mode with increasing temperature. Under thermal equilibrium, B is defined as R_r/n_i^2, where R_r and n_i are the radiative recombination rate and intrinsic carrier concentration, respectively. Under small deviation from equilibrium, the effective radiative recombination coefficient B^* is defined as $(np/n_i^2) \times B$, where n and p are the electron and hole concentration. According to our proposed model, Auger recombination rate increases exponentially with temperature, resulting in a higher hole concentration in sub-band V_B. Therefore, np/n_i^2 increases with temperature that qualitatively explains our observed deviation of B^* from the expected temperature-dependent behavior. It is worth noting that Auger coefficient of A-mode is slightly larger than that of B-mode (Figure 4-4a). As described above, phonon-assisted Auger recombination annihilates one electron in the conduction band, therefore affecting both (A and B) modes equally. This process, however, also annihilates two holes in the valence sub-band V_A. Consequently, the impact of Auger recombination process on A-mode is stronger than B-mode, resulting in a slightly larger Auger recombination coefficient. It should be noted that the obtained radiative and Auger recombination coefficients are nearly 3 and 6 orders of magnitude higher than the values reported for conventional bulk and quantum well semiconductors, respectively [175-177].

4.2.3. Radiative and Nonradiative Carrier Lifetime

Assuming that all of the recombination processes operate independently, the overall carrier recombination lifetime (τ) is calculated from its components, i.e., SRH lifetime ($\tau_{SRH} = 1/A$), radiative lifetime ($\tau_{rad} = 1/(Bn)$), and Auger lifetime ($\tau_{Auger} = 1/(Cn^2)$), by using the following equation:

$$\frac{1}{\tau} = \frac{1}{\tau_{SRH}} + \frac{1}{\tau_{rad}} + \frac{1}{\tau_{Auger}} \qquad \text{Eq. } (4-6)$$

These parameters of A-mode are plotted in Figure 4-5.

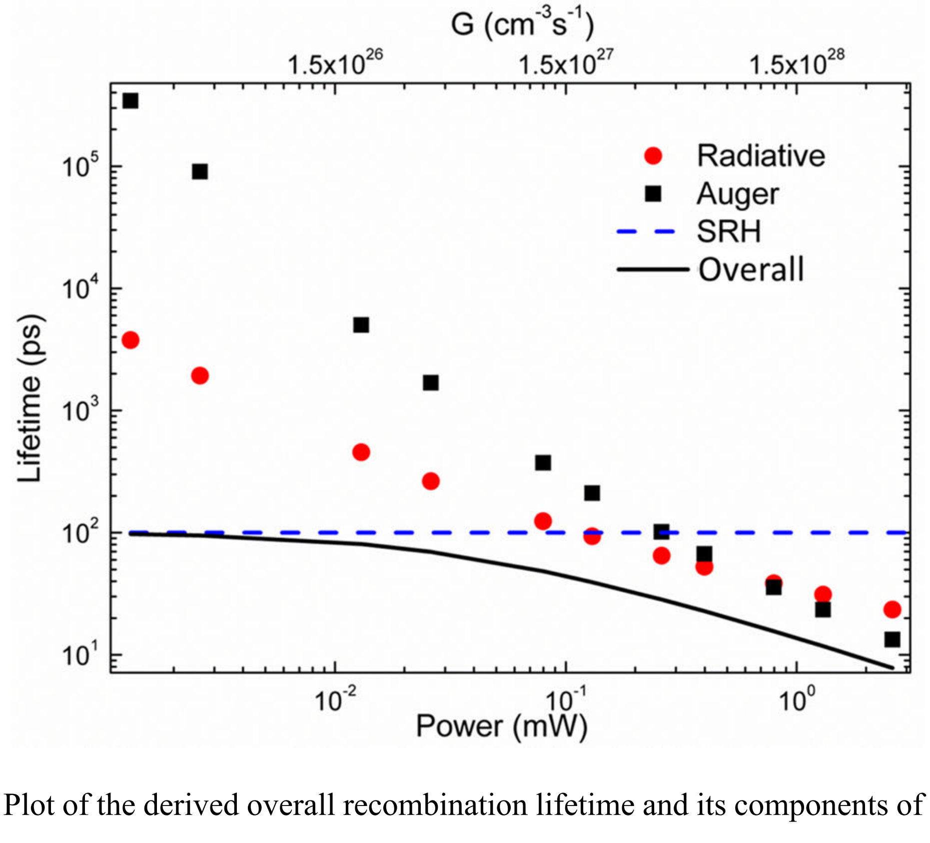

Figure 4-5: Plot of the derived overall recombination lifetime and its components of A-mode as a function of excitation power at 83 K [168].

For low generation rate (or excitation power), the carrier lifetime stays nearly constant and is determined by τ_{SRH} ~ 100 ps. In intermediate generation regime, the lifetime is determined by both SRH and radiative processes, leading to a small decrease; and for high generation rate, the lifetime is determined by Auger recombination. Further increasing the carrier injection enhances Auger recombination process, and thus resulting in further decrease in the carrier lifetime. The calculated carrier lifetime in this study is in excellent agreement with the previous report from time-resolved PL experiments [165].

4.3. Room-temperature Optically Pumped Lasers from Two-dimensional MoS_2

In section 4.2, we reported an abnormally strong Auger effect in 1L MoS_2, which causes the efficiency droop at high carrier concentrations (excitation power > 10^{-1} mW). In this work, we have investigated that the effect of Auger recombination is much less detrimental in four-layer (4L) MoS_2 compared to that in single layer counterpart, and further utilized 4L MoS_2 as the gain medium in a vertically coupled, free-standing SiO_x microdisk and microsphere cavity to achieve ultralow threshold lasing at room temperature.

4.3.1. Properties of As-exfoliated 4L MoS_2

4L MoS_2 flake was prepared and tested following the same method as afore-described for 1L MoS_2. Figure 4-6 shows the optical and AFM images of the flake, clearly confirming 4 layers of MoS_2 was deposited on Si/SiO_x substrate via mechanical exfoliation.

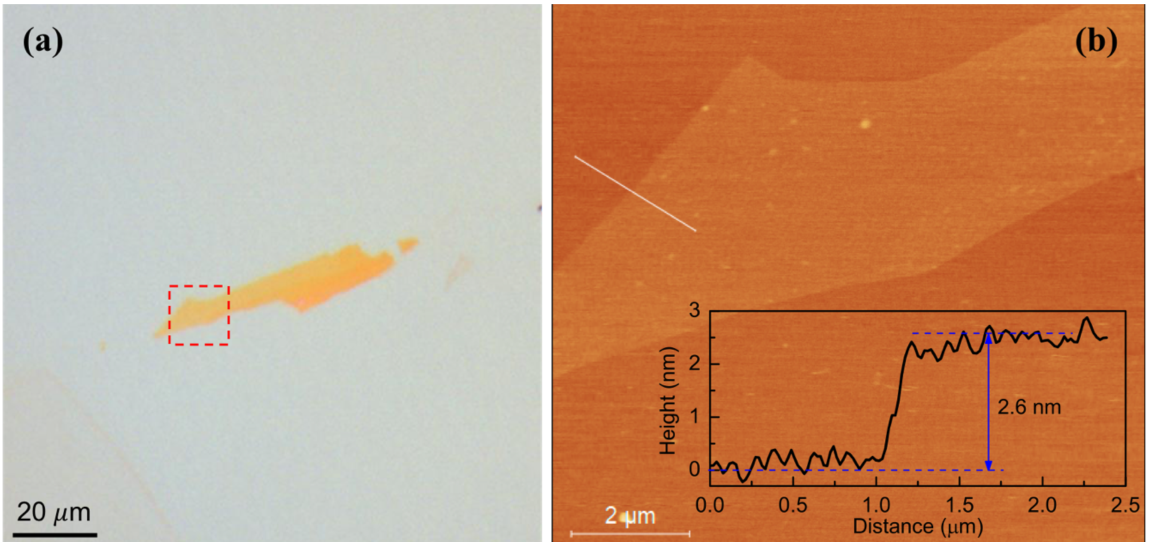

Figure 4-6: (a) Optical image (magnification 50×) of a MoS_2 flake deposited on Si/SiO_x substrate. **(b)** AFM image of the red dashed square shown in (a), confirming 4 layers of MoS_2 from height profile (inset) of the white line scan.

The room-temperature PL spectrum from 4L MoS_2 sample is plotted in Figure 4-7a in comparison with the spectrum from 1L flake. As can be seen, the integrated PL intensity of A- and B-mode of the 4L MoS_2 is about 2 and 50 times lower than that of the 1L counterpart, respectively. Beside these two modes, the PL spectrum of 4L MoS_2 reveals a new peak at 1.47 eV, which is attributed to indirect transition from the bottom of the conduction band along Λ point to the top of valance band at Γ point in multilayer MoS_2 [178]. Figure 4-7b shows much weaker efficiency droop in 4L MoS_2 under high excitation conditions compared to single-layer sample, indicating the reduction of Auger recombination. Employing the ABC model described in Section 4.2.2, we have determined the values of $\frac{A}{\sqrt{B}}$ and $\frac{C}{B^{1.5}}$ which were summarized in Table 4.1.

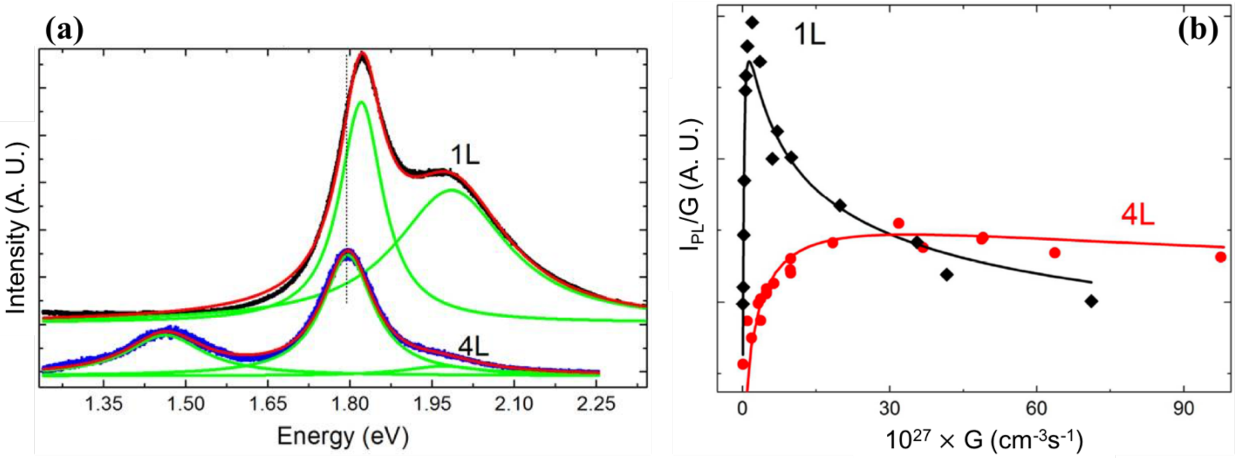

Figure 4-7: The room-temperature PL spectra **(a)** and Plot of the relative external quantum efficiency (EQE $\propto I_{PL}/G$) as a function of carrier generation rate (G) **(b)** of 1L and 4L MoS_2 [179].

Table 4-1: Summary of the fitting parameters ($A/B^{0.5}$ and $C/B^{1.5}$) and estimated values of A, B and C coefficients in monolayer and 4L MoS_2 [179].

Parameter No. of layer	$\frac{A}{B^{0.5}}$	$\frac{C}{B^{1.5}}$	A (s^{-1})	B (cm^3·s^{-1})	C (cm^6·s^{-1})
1	5.8×10^{13}	3.0×10^{-13}	1.0×10^{10}	3.0×10^{-8}	1.6×10^{-24}
4	6.8×10^{13}	4.3×10^{-15}	2.0×10^{9}	8.7×10^{-10}	1.1×10^{-28}

The value of $\frac{A}{\sqrt{B}}$ is similar for both 1L and 4L samples, suggesting that any reduction in surface recombination in 4L MoS_2 was compensated by a reduction of its radiative recombination. However, $\frac{C}{B^{1.5}}$ is reduced by two orders of magnitude as increasing the number of layers from single to four layers. This is an indication of a much weaker Auger effect in multilayer MoS_2.

4.3.2. Fabrication of MoS_2-based Optically Pumped Lasers

The MoS_2-based coupled microdisk/microsphere cavity laser devices were fabricated by photolithography and electron-beam lithography, together with etching techniques. Figure 4-8 illustrates the fabrication sequence of the devices using photolithography. MoS_2 flakes were first mechanically exfoliated on a Si substrate (2” in diameter) coated with 340 nm SiO_2 thermally grown by wet oxidation. The sample was then spin-coated with Shipley 1813 photoresist to define the microdisk arrays via UV exposure and development processes. XeF_2 was used as a vapor phase etchant to remove the exposed MoS_2, followed by reactive ion etching (RIE) in $CF_4/CHF_3/Ar$ to form the oxide disks with diameter of 15 μm. Si was then etched isotropically using XeF_2 until a Si post (lateral size ~2 – 5 μm) was formed to support the SiO_2 disk at its center. Subsequently, the photoresist was removed by solvent stripper. In the final step of microdisk fabrication, the sample was treated in O_2 plasma for 1 min to remove the resist residues and enhance PL intensity, as theoretically and experimentally proved previously [180]. The silica microspheres (diameter of ~7.7 μm) purchased from Cospheric Company were finally dispersed on the microdisks.

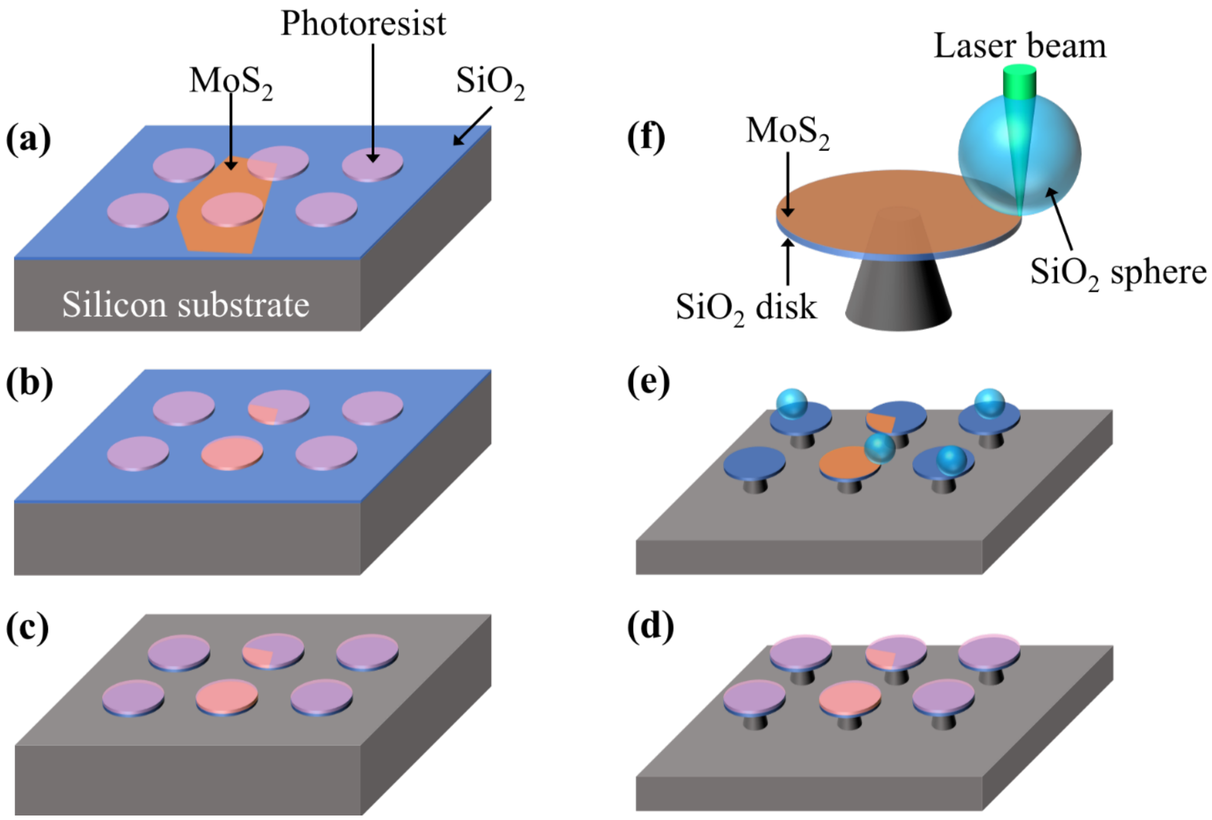

Figure 4-8: Fabrication sequence of microdisk and microsphere cavities. **(a)** Definition of microdisk arrays by standard photolithography. **(b)** Removal of exposed MoS_2 by etching with XeF_2. **(c)** Formation of the microdisks after RIE, followed by Si etching using XeF_2 **(d)**. **(e)** Resist removal and dispersion of silica microspheres. **(f)** Schematic illustration of the MoS_2 vertically coupled optical cavity device and measurement configuration.

For the devices fabricated using EBL (Figure 4-9), the sample (1 cm × 1 cm) containing exfoliated MoS_2 flakes was first spin-coated with 350 nm PMMA A2 positive resist, and then an annular opening with inner and outer diameters of 15 μm and 25 μm, respectively, was defined after standard EBL. The following steps were similar to photolithography process.

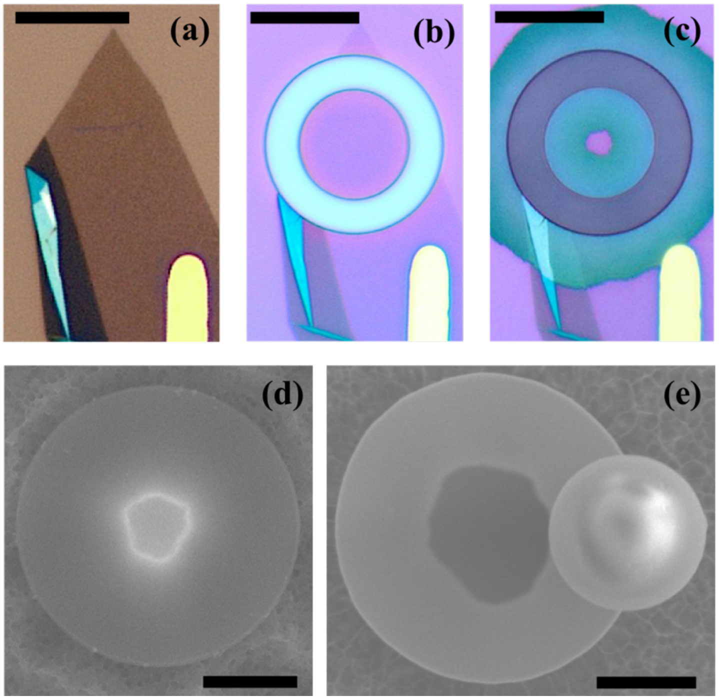

Figure 4-9: Optical microscope images of the sample **(a)** containing a mechanically exfoliated MoS_2 flake on SiO_2/Si substrate, **(b)** after removing the oxide by RIE, **(c)** after isotropic etching of Si by XeF_2. Scale bars (a-c), 15 μm. **(d)** SEM image of the sample in (c). **(e)** Representative top-view SEM image of the sample after microsphere dispersion. Scale bars (d-e), 5 μm.

4.3.3. Performance of MoS_2 Microlaser

The optical measurements were carried out at room temperature under N_2 ambient inside a cryostat using a micro-PL setup with 514 nm pump laser under continuous wave operation. Prior to the experiments, the sample was annealed at 150 °C for 10 min under N_2 gas and then cooled down to room temperature. The laser beam was focused on the top pole of the microsphere that provided a lensing effect to reduce the excitation area by ~16 times, resulting in a significantly enhanced carrier generation rate at relatively low pumping power. A room-temperature charge coupled device (CCD) camera operating in the range of 400 – 1000 nm was used to detect the light emission.

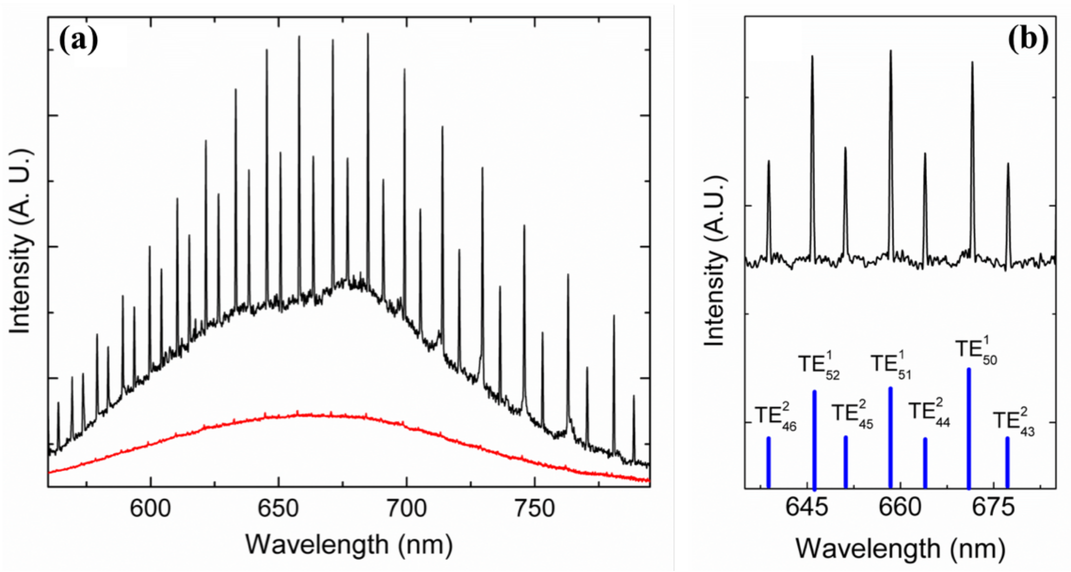

Figure 4-10: (a) Room-temperature PL spectra of the MoS_2 microlaser at excitation power of 3 μW (red) and 30 μW (black). **(b)** WGM spectrum after subtracting the background spontaneous emission (upper) along with the calculated mode positions (lower) using Mie's theory (excitation power of 100 μW). [179]

Shown in Figure 4-10a are the PL spectra of a 4L MoS_2 laser device measured at room temperature below and above threshold power (P_{th}). Very weak whispering gallery modes (WGMs) were observed at an excitation power of 3 μW (below threshold). By increasing the excitation power to 30 μW (above threshold), sharp WGM peaks emerged and superimposed on the broad background spontaneous emission spectrum. It should be noted that the enhancement factor of the WGMs is 10 times higher than that of the spontaneous emission as increasing pump power. Figure 4-10b plots the WGM spectrum at an excitation power of 100 μW after subtracting the background emission, along with the derived mode positions from Mie's theory [181]. The positions of WGMs, with angular mode number l confined in a microsphere with radius of R (= 3.85 μm) and refractive index of n_s (~1.5 for silica) surrounded by a medium with refractive index of n_0 (= 1 for air), are the roots of the following equation:

$$F(\lambda) = \left(\eta\alpha + \frac{l}{R}\right) \times j_l(kn_sR) - kn_s \times j_{l+1}(kn_sR) \qquad \text{Eq.}(4-7)$$

where:

$$\eta = \begin{cases} 1 & (TE \text{ mode}) \\ (n_s/n_0)^2 & (TM \text{ mode}) \end{cases} \qquad \text{Eq.}(4-7\text{a})$$

$$\alpha = (\beta^2 - k^2n_0^2)^{1/2} \qquad \text{Eq.}(4-7\text{b})$$

$$\beta = [l(l+1)]^{1/2}/R \qquad \text{Eq.}(4-7\text{c})$$

$$k = 2\pi/\lambda \qquad \text{Eq.}(4-7\text{d})$$

$$l = 2\pi Rn_{eff}/\lambda \qquad \text{Eq.}(4-7\text{e})$$

j_l represents the spherical Bessel function, n_{eff} is the effective refractive index of the microsphere for a given mode, which is about 1.43. The calculated WGM peak positions are in excellent agreement with the observed lasing modes from PL spectrum, and indicate that the spectrum is composed of the first and the second order transverse electric (TE) polarized modes. The quality factor (Q) was estimated from $Q = \lambda/\delta\lambda$, where $\delta\lambda$ is the linewidth or FWHM of the WGMs. In our coupled microsphere/microdisk optical cavity with embedded MoS_2 at the interface, Q-factor was found to be in the range of 2600 – 3300 and 1900 – 2500 for the first and second order TE polarized modes, respectively.

The device performance was further studied via the excitation power-dependent measurements by changing the pump power from 0.2 μW to 1 mW under continuous wave operation. Figure 4-11a shows the variation of the integrated intensity and FWHM of the first order TE mode with angular mode number of $l = 52$ (TE^1_{52}) at relatively low excitation powers. We observed a low threshold power of 5 μW, which can be attributed to the enhanced Coulomb interactions and the enhanced pumping efficiency in microsphere cavity. In addition, a clear observation of spectral linewidth reduction from 0.36 ± 0.02 nm to 0.26 ± 0.02 nm as increasing pump power further confirms lasing operation. More importantly, no saturation was measured for pumping power up to 1 mW (200 times above the threshold) as shown in Figure 4-11b, suggesting the feasibility of stable, low noise, and high output power laser based on MoS_2 thin films.

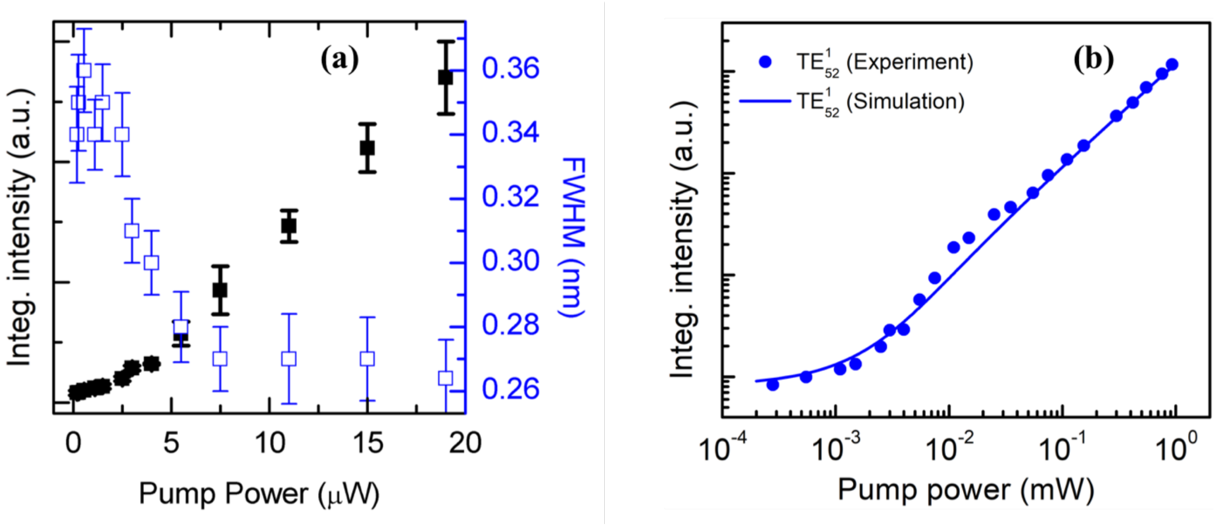

Figure 4-11: (a) Variation of FWHM and integrated intensity as a function of excitation power for TE^1_{52}. **(b)** Log-Log plot of the integrated intensity as a function of excitation power for TE^1_{52} mode along with the simulated result (solid curve) based on rate equation analysis.

4.4. Conclusion

In summary, we have investigated the exciton kinetics, quantum efficiency, and efficiency droop in monolayer MoS_2 via temperature- and power-dependent PL studies. The radiative bimolecular and nonradiative Auger recombination coefficients were calculated that indicate efficient indirect Auger recombination processes. Consequently, photonic devices based on monolayer MoS_2 may suffer from efficiency droop at high carrier injection concentrations, albeit reachable internal quantum efficiency of 45% at 83 K. On the contrary, four-layer MoS_2 exhibits much weaker efficiency droop under high excitation conditions, and therefore was successfully used to fabricate stable, ultralow threshold laser devices operating at room temperature, in which 2D material was sandwiched between a free-standing SiO_2 microdisk and a silica microsphere.

The device shows a remarkably low threshold power of 5 μW under continuous wave operation. Our findings can pave the way for the realization of 2D TMDC-based nanophotonic devices on low-cost, large area substrates for flexible display, sensing, and optical communication applications.

Chapter 5: Multi-wafer Demonstration of Photochemical Water Splitting under Natural Sunlight using Fresnel Lens

III-nitride nanowires can be used not only for optoelectronic applications but also for renewable energy. In Chapter 5, we present the scaling up of nanowire growth on large Si wafers and demonstrate large-scale hydrogen production via water splitting under concentrated natural sunlight.

5.1. Introduction

Harvesting solar power to produce hydrogen via water splitting process has emerged as one of the key technologies towards the future of clean, renewable, and sustainable energy resource. Critical to the development of practical system includes the realization of efficient visible light driven photocatalysts that are extremely robust and stable in harsh photocatalytic conditions, and can be synthesized on large scale using industry-friendly mature techniques. State-of-the-art PEC and photovoltaic-assisted electrolysis (PV-E) devices demonstrate solar-to-hydrogen (STH) energy conversion efficiency up to 19% and 30%, respectively [182, 183]. Nevertheless, most studies based on these techniques are focused on very small samples (active area of ~0.3 cm^2 or less) to minimize the losses due to significantly increased resistivity and potential drop at large-scale [183, 184]. In addition, photovoltaic-electrochemical (PV-EC) cells with high STH efficiency (>10%) mostly rely on PV-grade materials [185, 186] with poor photocatalytic stability and high manufacturing costs [187], limiting practical realization of the technology at larger scale. The system scalability is further limited by the integration of additional protective or passivation layer, which often involves expensive techniques [188]. In this context, PC water splitting holds enormous promise for hydrogen generation in neutral pH condition at the wafer scale owing to the integration of micro/nano-electrodes on the semiconductor surfaces that greatly eliminates the problem of ionic diffusion for balanced water splitting reaction.

Particulate photocatalytic systems have been widely studied over the past decades. To date, however, the STH energy conversion efficiency on such devices has been generally limited to ~1%, or less while exhibiting low apparent quantum yield (AQY) under visible light irradiation [189]. Major challenges that hinder the realization of large-scale photocatalytic water splitting using simple powdered photocatalysts include large grain boundary resistance resulted from aggregation and weak light absorption of small particles, abrasion in long-term measurements, and poor stability under concentrated sunlight irradiation [190, 191]. It is worth mentioning the benefits of using high intensity light source for economically viable industrial production of hydrogen using limited land area and employing minimum amount of photocatalyst [79, 192-194]. However, most of the photocatalysts become unstable and less-efficient under concentrated irradiation due to enhanced corrosion (self-oxidation) and radiative recombination, therefore requiring significant scalability (very large device-area) to exhibit comparable yield when operated under the nominal light intensity of one sun [191].

Wafer-scale GaN-based nanostructure has been proved as a very promising, yet less explored photocatalyst for highly efficient, stable unassisted overall neutral water splitting under concentrated sunlight thanks to some distinct attributes. For example, the bandgap and band-edges of GaN-based alloys can be tuned to absorb extended visible spectrum from sunlight while straddling the redox potentials of water [89]; the surface charge properties (i.e., surface Fermi-level) of the nanostructured photocatalysts can be tuned through controlled Mg-dopant incorporation, and the apparent quantum efficiency (AQE) for solar-to-hydrogen conversion can be enhanced by nearly two orders of magnitude under UV [195] and visible light illumination [196]. Harvesting of solar energy and carrier extraction at high illumination intensity is more efficient using such vertically-aligned wafer-level nanostructures. However, albeit the gradual and consistent improvements in numerous performance metrics, there exists significant challenges that need to be addressed prior to the development of a practical renewable GaN-based artificial photosynthesis system.

In this work, we demonstrate the large-scale unassisted overall water splitting under natural sunlight using standard materials widely used in the industry, i.e., GaN alloys on Si wafers, and address some of the key issues related to scalability and reproducibility towards the translation of the technology from the lab to the 'real world'. We primarily focus on the scalability of the light absorber, one of the key factors towards large-scale realization of water splitting system. Therefore, the nanowire synthesis and the device area were reproducibly scaled up using larger Si substrates (3-inch diameter), which is substantially challenging. The nanowire morphology, uniformity, Mg-doping concentration and crystalline quality were optimized for maximum performance of the device. To facilitate water splitting reaction, Co_3O_4 and Rh/Cr_2O_3 nanoparticles were deposited on the nanowire surfaces as water oxidation and proton reduction co-catalysts for OER and HER, respectively. The dual-cocatalyst decorated double-band GaN/InGaN nanowires exhibit an STH efficiency of ~1.1% when tested under concentrated natural sunlight, with average intensity of ~60 suns on the sample surface. Our study on the intensity dependent photochemical activity suggests that by optimizing the solar concentration ratio and water level thickness on such devices, the STH efficiency can be improved significantly.

5.2. Demonstration of Wafer-scale Unassisted Artificial Photosynthesis under Natural Sunlight

5.2.1. On the Synthesis Scaling-up and Characterization of *p*-GaN/InGaN Double-band Nanowire Heterostructures

Design and growth of double-band *p*-GaN/InGaN nanowire heterostructure

Previous studies on the synthesis and performance evaluation of Ga(In)N nanowire based photocatalysts using MBE were largely focused on small sample sizes [196, 197], which is generally true for almost all PC and PEC water splitting devices. Herein, we demonstrate and optimize the realization of double-band GaN:Mg/InGaN:Mg nanowire arrays on relatively large Si wafer (diameter: 3-inch) by plasma-assisted MBE after extensive studies on the growth and characterization of Mg-doped GaN and InGaN nanowires. Vertically aligned GaN/InGaN nanowires (schematically illustrated in Figure 5-1) were grown on *n*-type Si (111) substrate using Veeco GENxplor MBE system equipped with a radio frequency plasma-assisted nitrogen source. *In-situ* oxide desorption was performed at ~ 900 °C in the growth chamber before the growth initiation, which was confirmed by a clean Si (111) 7 × 7 reconstructed surface using reflection high-energy electron diffraction (RHEED) analysis. Instead of using foreign metal catalyst (Au, Ni, Fe) which often diffuses into the nanowires and creates deep-level defects, a very thin (about mono-layer) Ga seeding layer was deposited to promote the nucleation of nanowires with controlled size and uniformity via diffusion-induced mechanism [101]. In this study, the nanowires were grown under nitrogen-rich condition that suppresses the formation of N-vacancy related defects. Moreover, it has been proved that unique N-termination of both top and side surfaces of the nanowires can be achieved under this growth condition, and hence leading to high efficiency and stability for overall water splitting [198].

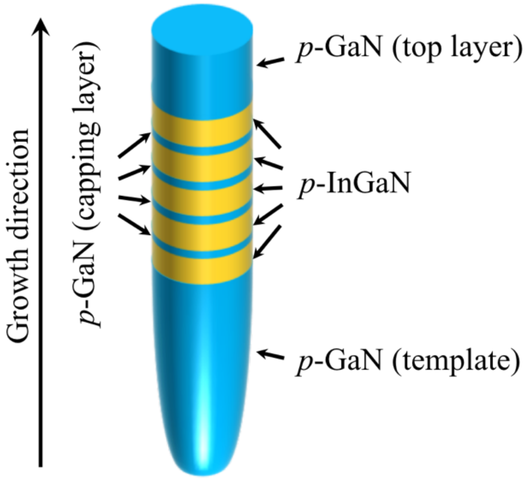

Figure 5-1: Schematic illustration of double-band GaN/InGaN nanowire heterostructure.

The optimization of GaN/InGaN nanowire heterostructure growth commenced with the p-GaN segment served as a template, which plays an important role in the density, morphology, crystalline quality and consequently, the photocatalytic performance of the nanowires. The growth conditions of p-GaN included a substrate temperature in a range of 860 °C – 800 °C, and a Ga flux of ~5.1 ×10^{-8} Torr, a Mg effusion cell temperature (T_{Mg}) of 200 °C – 320 °C. Shown in Figure 5-2 are SEM images of p-GaN nanowire arrays grown at different substrate temperatures. The uniformity in morphology and distribution of the nanowire arrays grown at 810 °C provides enhanced photocatalytic hydrogen evolution (as shown in Figure 5-3a) which can also be correlated to effective Mg-dopant incorporation. However, nanowires epitaxially grown at a low substrate temperature are typically big and short as shown in Figure 5-2c, resulting in a possible nanowire coalescence. To avoid further coalescence of the double-band p-GaN/InGaN nanowire arrays, a second p-GaN segment was then grown at a slightly higher substrate temperature of 840 °C, a nitrogen flow of 1.0 sccm, and a Ga flux of ~6.3 × 10^{-8} Torr. Together with substrate temperature, the III/V flux ratio also strongly affects the growth morphology. Thus, Ga cell temperature, nitrogen flow rate and plasma power were carefully tuned to obtain uniform nanowire arrays with least coalescence.

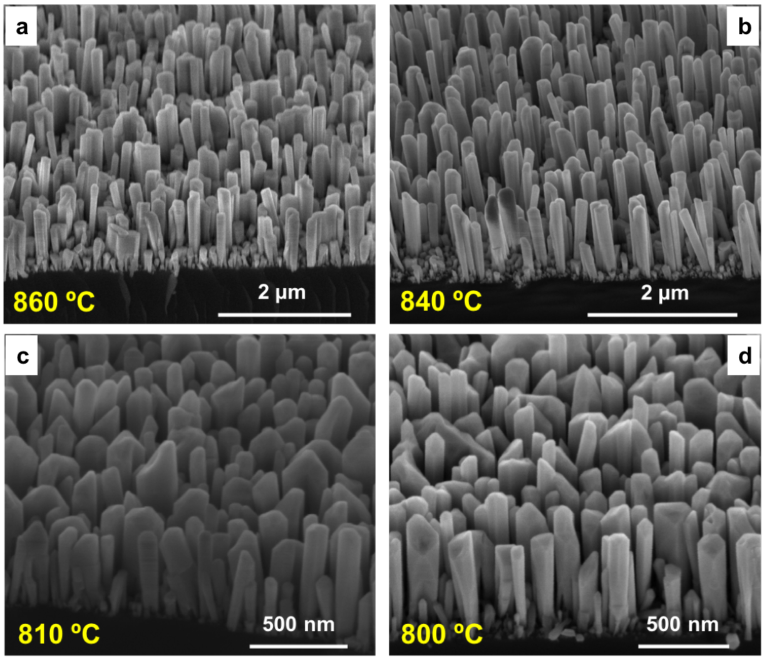

Figure 5-2: Effect of growth temperature on the nanowire morphology. SEM images of Mg-doped *p*-GaN nanowire arrays grown on large-area Si wafer (duration ~4 hours) at different substrate temperatures in the range of 860 °C – 800 °C.

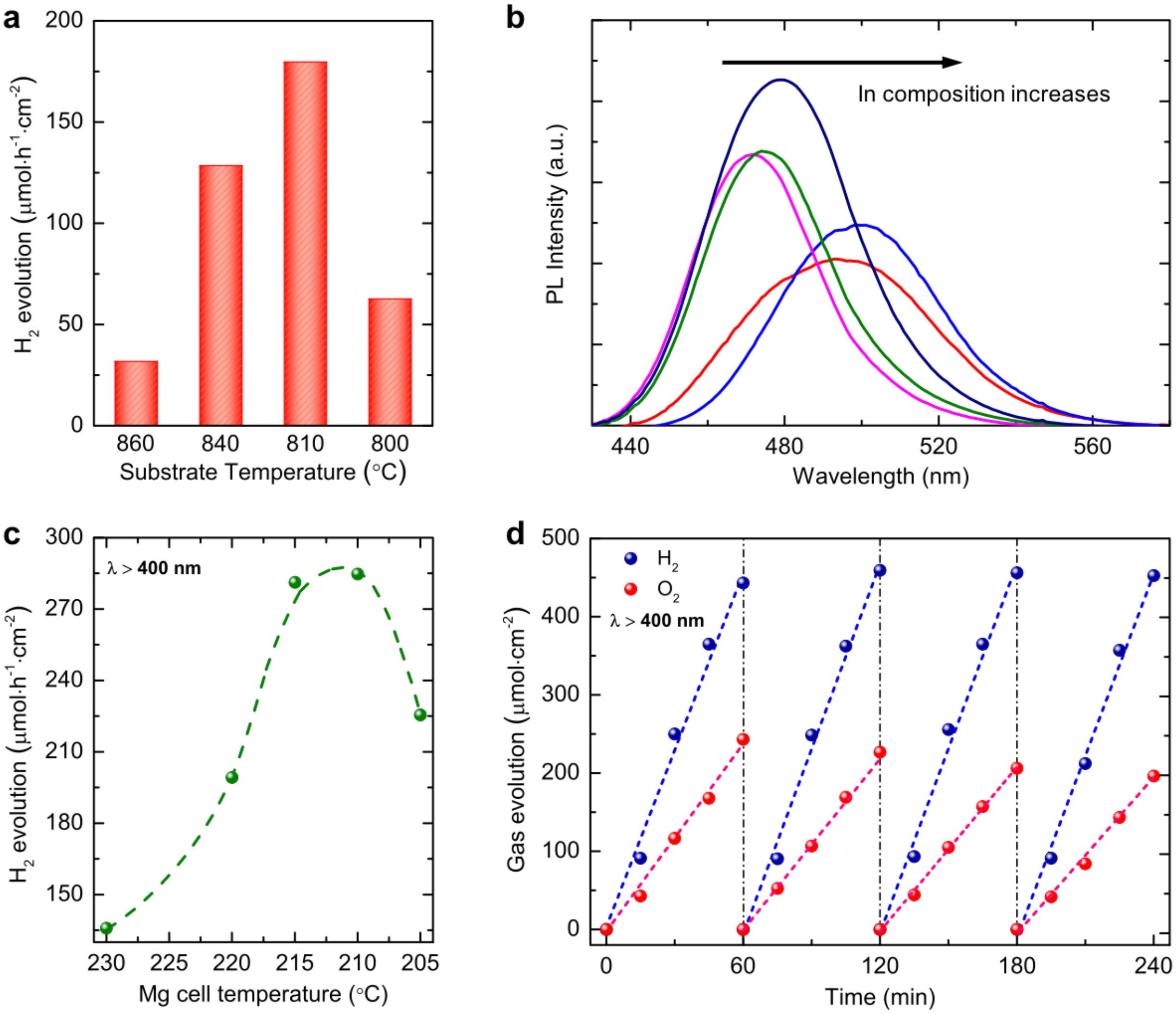

Figure 5-3: Structural optimization of GaN/InGaN double-band nanowires grown by MBE. **(a)** Variation of H_2 evolution rate with substrate temperatures, measured from Mg-doped GaN template decorated with Rh/Cr_2O_3 core/shell nanoparticles under full-arc illumination. **(b)** Room-temperature PL spectra of samples with different In contents ranging from 20% – 25%. **(c)** Significant dependence of photocatalytic performance (in visible range) on the Mg doping levels controlled by changing Mg cell temperature. **(d)** Reaction time courses of overall water splitting on *p*-GaN/$In_{0.22}Ga_{0.78}N$ nanowire arrays coated with Rh/Cr_2O_3 and Co_3O_4 nanoparticles under visible light (> 400 nm) illumination, revealing the stoichiometric ratio of 2:1 (H_2:O_2) and stability of nanowire heterostructures.

Subsequently, five p-$In_xGa_{1-x}N$ segments (each ~70-100 nm in length, depending on the diameter) sandwiched with thin (~10nm) GaN layers were embedded into GaN nanowires to enhance visible photon absorption [196]. The growth conditions of $In_xGa_{1-x}N$ segment consisted of a substrate temperature of 775 °C, a nitrogen flow of 1.0 sccm, an In and Ga fluxes of ~$5.0 \times 10^{-8} - 6.8 \times 10^{-8}$ Torr, and 3.87×10^{-8} Torr, respectively. The growth of multi-stacked GaN/InGaN was performed at sufficient low substrate temperature in order to prevent In desorption and phase separation [199]. Finally, a Mg-doped GaN segment was grown on top, which not only prevents the energy loss due to thermal relaxation of carriers in InGaN but also harvests UV photons and leads to enhanced photocatalytic activity. By varying In composition, the bandgap of $In_xGa_{1-x}N$ was tuned properly to be narrow enough for driving redox reactions forward without sacrificing the device performance, which is evident from the emission wavelength (bandgap) of the nanowires (Figure 5-3b). As derived in our previous studies [195], unassisted photochemical dissociation of water using nanowire heterostructures is also extremely sensitive to the magnitude of the near surface band-bending. Mg dopant incorporation in GaN and InGaN bands were individually tuned to achieve optimum band-bending at the non-polar lateral surfaces. The Mg effusion cell temperature was varied from 205 °C to 230 °C (Figure 5-3c), and the maximum photocatalytic performance was obtained at T_{Mg} of ~210 °C with corresponding BEP of ~8.1×10^{-11} Torr. With optimum Mg-doping concentration, unassisted visible-light driven overall water splitting can be observed with stoichiometric gas evolution ratio of H_2:O_2 = 2:1, as shown in Figure 5-3d, exhibiting nearly two-fold enhancement in photocatalytic activity and performance stability, when loaded with both Rh/Cr_2O_3 and Co_3O_4 nanoparticles as co-catalysts [196]. Significantly, the performance of the photocatalytic device is not compromised compared to previous reports, despite the large-scale nanowire synthesis and device processing, which will be discussed further in later sections. In the wavelength range of 400-480 nm, the AQE and energy conversion efficiency (ECE) were estimated as ~28.8% and 12.8%, respectively, when illuminated with intensity equivalent to ~29 suns and absorbable incident power of ~237.1 mW cm^{-2}.

In summary, extensive growth optimization was performed to achieve multi-stacked GaN/InGaN nanowire arrays, exhibiting high photocatalytic activity and excellent stability. The optimum growth conditions for p-GaN segments consist of substrate temperatures of 810 °C and 840 °C; Ga fluxes of ~5.1 $\times 10^{-8}$ Torr and ~6.3 $\times$ 10^{-8} Torr, respectively; a T_{Mg} of 210 °C – 320 °C. The optimal growth conditions of InGaN segments include a substrate temperature of 775 °C; In and Ga fluxes of ~5.0 $\times$ 10^{-8}, and ~3.87 $\times$ 10^{-8} Torr, respectively; a T_{Mg} of 210 °C corresponding to a Mg equivalent pressure of ~8.1 $\times$ 10^{-11} Torr. A nitrogen flow rate of 1.0 sccm, and a forward plasma power of ~380 W were used.

Optimization of cocatalysts loading

Scaling up and optimizing the amount of cocatalyst loading on the large-area InGaN nanowire based artificial photosynthesis device is non-linear due to numerous reasons: (i) The structural inhomogeneity of the nanowires along the radial direction of Si wafer that can be correlated to gradual change of In composition and nanowire morphology due to the temperature gradient during MBE growth, (ii) lack of suitable irradiation source (lamp) with large beam-size and uniform intensity distribution for photoexcitation of the device (Figure 5-4). Therefore, the concentration and the amount of precursor solution for optimum co-catalyst loading are subject to changes depending on the area of illumination, the average light intensity on the sample surface and the duration of photoexcitation.

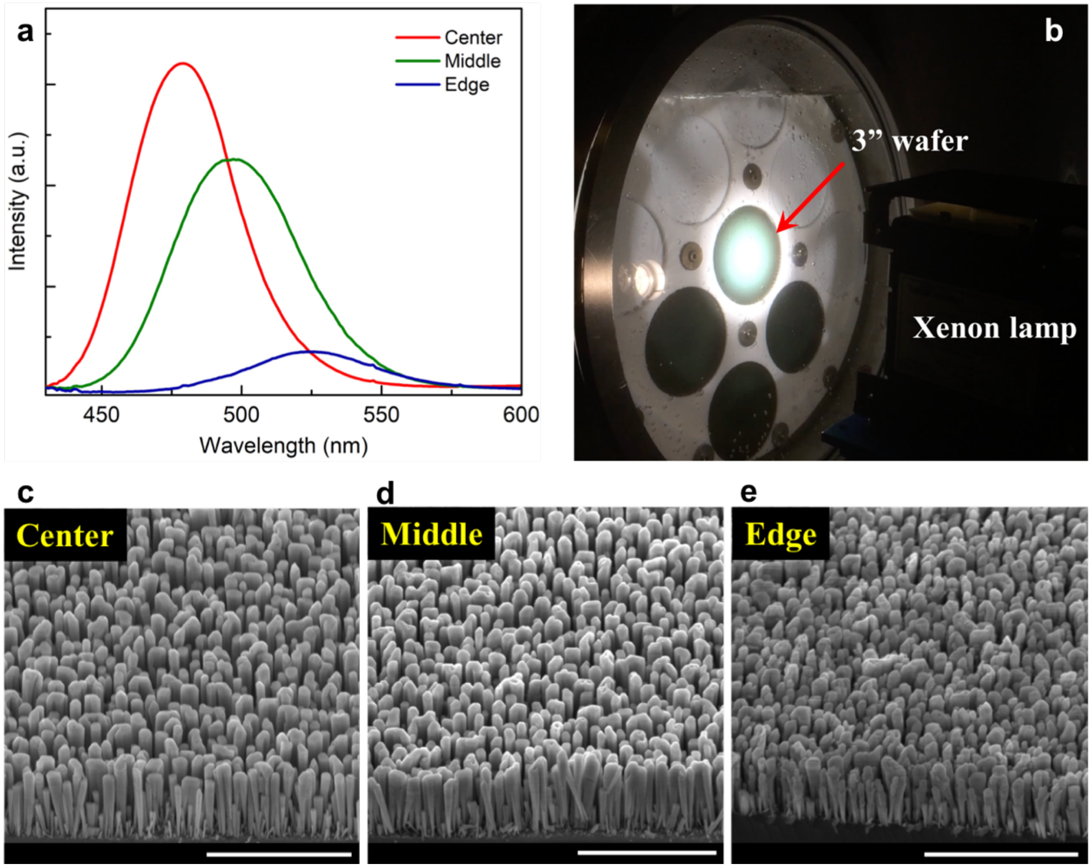

Figure 5-4: **(a)** Room-temperature PL spectra of as-grown sample measured at different points from center towards periphery, showing the structural inhomogeneity. This implies that the scaled-up device can largely provide consistent photocatalytic activity for almost entire area. **(b)** Non-uniform intensity distribution of Xenon short arc lamp (PE 300BUV) over 3” Si wafer. **(c-e)** SEM images of InGaN nanowires taken at different regions of the device. Scale bar, 2 μm.

In this study, 0.5 M sodium hexachlororhodate (III) (Na_3RhCl_6), 0.2 M potassium chromate (K_2CrO_4), 0.01 M cobalt nitrate hexahydrate ($Co(NO_3)_2 \cdot 6H_2O$) precursors were used for the decoration of Rh, Cr_2O_3, and Co_3O_4 nanoparticles, respectively on *p*-GaN/InGaN nanowire surface. With the maximum average light intensity (~29 suns) available in the lab-scale for large-area wafer illumination, the duration of the photoexcitation was varied as 30, 45, 60, and 77 minutes for metal deposition. H_2 evolution from the photodeposition of Rh nanoparticles hits the plateau after 60 minutes for a wide range of precursor loading. The amount of Na_3RhCl_6 precursor solution was then varied during the photodeposition of Rh (for 60 mins). As such, 65 μl of Na_3RhCl_6 and 65 μl of K_2CrO_4 precursor solutions have been found to be optimum amounts for the best photocatalytic performance of the large-area device when loaded with Rh/Cr_2O_3 (core-shell) nanoparticles as co-catalyst for HER. Subsequently, the amount of $Co(NO_3)_2{\cdot}6H_2O$ precursor solution for Co_3O_4 cocatalyst loading was varied within the range of 75-125 μl. The device exhibits maximum hydrogen evolution rate with stoichiometric ratio (H_2:O_2 ~2:1) from unassisted overall pure water splitting, when Co_3O_4 is photodeposited for 60 minutes on the nanowires using 95 μl of $Co(NO_3)_2{\cdot}6H_2O$ precursor (Figure 5-5a). As a result, an improvement of ~20% in the photocatalytic activity was observed on samples decorated with dual-cocatalysts compared to that of the samples using only HER cocatalyst under visible light illumination (Figure 5-5b). The conditions for optimum loading of dual-cocatalyst nanoparticles (Rh/Cr_2O_3 and Co_3O_4) on double-band *p*-GaN/InGaN nanowire heterostructures of large-area (~41 cm^2) artificial photosynthesis device is summarized below:

Na_3RhCl_6	K_2CrO_4	CH_3OH/H_2O	$Co(NO_3)_2{\cdot}6H_2O$	KIO_3/H_2O	Deposition time
65 μl	65 μl	24/120 ml	95 μl	14.3/130 ml	60 min

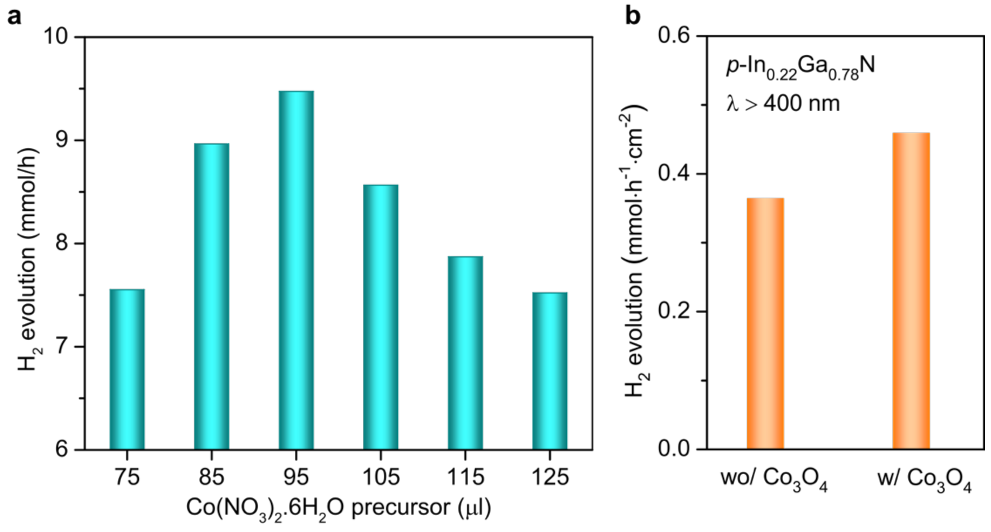

Figure 5-5: (a) Optimization of Co_3O_4 cocatalyst loading on whole 3" device area for suitable distribution of reaction sites on nanowire surfaces and to prevent back reactions. **(b)** Improvement of the photocatalytic activity on the sample decorated with dual-cocatalysts. Experiments were carried out under visible light irradiation (> 400 nm).

TEM characterization of double-band *p*-GaN/InGaN nanowires

Structurally, the morphology and the crystalline quality of the nanowires in larger devices are comparable to those processed at smaller scale. The high-resolution scanning transmission electron microscopy high-angle annular dark-field (STEM-HAADF) and bright-field (STEM-BF) image of the nanowire (Figure 5-6a) clearly depicts multiple $In_{0.22}Ga_{0.78}N$ segments (each ~70-100 nm in length, depending on the diameter) incorporated in the visible band of the nanowire heterostructure. Energy dispersive X-ray scanning (EDXS) spectrum analysis and elemental mapping of Ga and In further illustrates the top GaN layer (UV-band) and the sharp interfaces between multiple layers. Both the UV- and visible-band (GaN and InGaN segments) of the nanowire were controllably doped with magnesium for *p*-type conductivity, optimum surface charge properties (band-bending) and enhanced photocatalytic activity. Figure 5-6b further reveals the fluctuation of material compositions (Ga and In) along the growth direction using EDXS line spectrum analysis. The secondary electron (SE) spectral image of a dual-cocatalyst loaded (not-optimized) nanowire and the EDXS elemental mapping of Rh and Co (Figure 5-6c) confirms the simultaneous deposition of both Co_3O_4 and Rh on the nanowire surface as water oxidation and proton reduction cocatalysts. The crystalline quality and the abrupt interfaces between GaN and InGaN were confirmed from HRTEM lattice fringe images, as presented in Figure 5-6d.

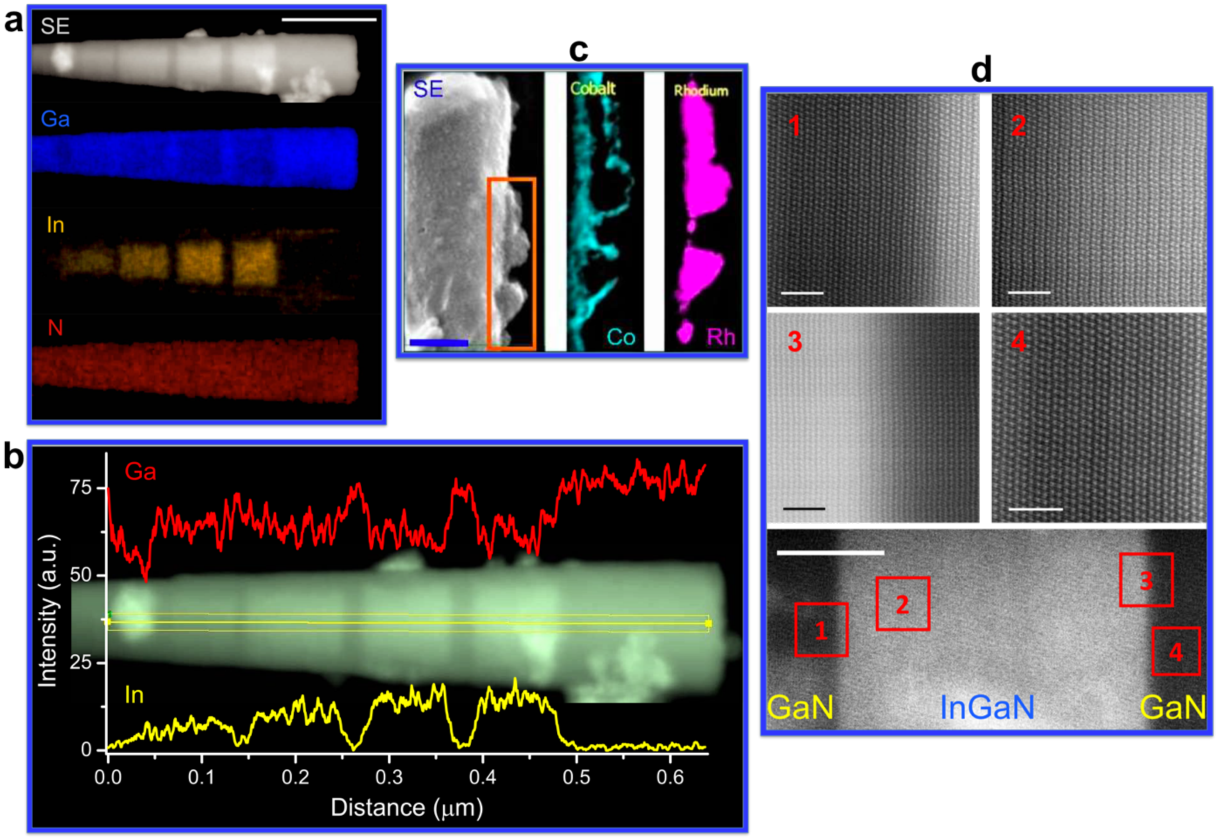

Figure 5-6: **(a)** STEM-HAADF spectral image and energy dispersive X-ray scanning (EDXS) elemental (Ga, In and N) mapping of the *p*-GaN/InGaN nanowire, clearly depicting InGaN segments incorporated in the visible band and the top *p*-GaN segment (UV-band) of the double-band nanowire heterostructure. Scale bar, 200 nm. **(b)** EDXS line scan showing the fluctuations of In and Ga content along the growth direction of the nanowire. Scale bar, 200 nm. **(c)** STEM-SE image of a portion of dual-cocatalyst loaded nanowire (left) and the EDXS elemental mapping of the selected region, showing the simultaneous presence and distribution of cobalt (from Co_3O_4) and Rh (from Rh/Cr_2O_3) on the nanowire surface. Scale bar, 50 nm. **(d)** HRSTEM-ZC lattice fringe

images taken from different regions of the GaN/InGaN nanowire (bottom. Scale bar, 20 nm). The regions include: (1) GaN capping layer, sandwiched between InGaN segments, (2) InGaN layer, (3) abrupt interface between InGaN and GaN and (4) top *p*-GaN layer as UV band. Scale bars, 2 nm.

5.2.2. Setup Preparation

Photoreactor – Preliminary design for multi-wafer demonstration

An (3×3) array of III-nitride photocatalysts synthesized on commercially available and recyclable 3-inch Si wafers can be integrated into a panel-type reactor/chamber for large-scale realization of unassisted overall pure water splitting under concentrated sunlight. The chamber was made of aluminum, which is cheap, light, and easily machinable compared to other materials such as stainless steel or copper alloys. Moreover, Al chamber is anti-corrosive and can withstand vacuum nicely with the use of an appropriate (in terms of thickness) quartz window and high-temperature silicon o-ring.

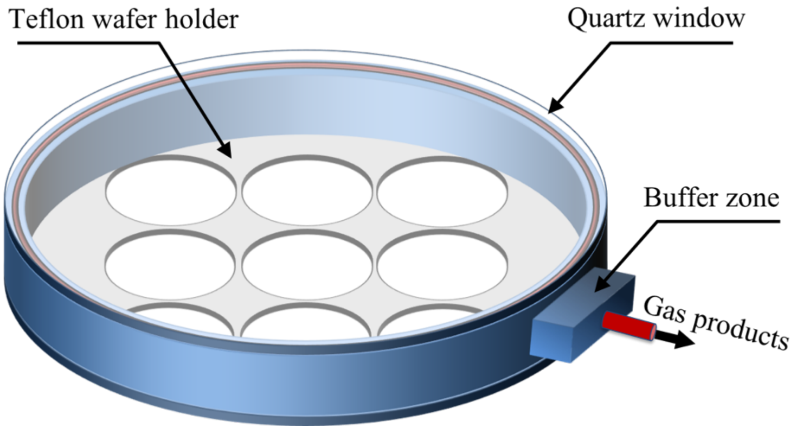

Figure 5-7 Schematic illustration of Aluminum chamber that holds up to 9 Si wafers (diameter: 3 inch) for large-scale demonstration of photocatalytic water splitting under real concentrated sunlight irradiation.

As shown in Figure 5-7, a buffer zone was integrated on the sidewall of the photoreactor to facilitate gas evolution from a large amount of water into the container. In addition, the extra space created by the buffer zone can help prevent water suction during chamber evacuation. Three adjustable clamps (not shown) were mounted on the chamber to provide extra force holding the quartz window during the experiment as the pressure increases with the reaction time.

Fresnel lens system concentrating natural sunlight

Pictorial demonstration of panel-type photocatalytic water splitting system is shown in Figure 5-8a. The unit consists of a 1.1 m × 1.1 m Fresnel lens with transmittance of ~93% mounted on the top part of wooden frame while the chamber is fixed in the center of bottom part to ensure consistent angle of incident light during the experiment, thus minimizing the reduction of photoactivity due to reflectance and shadowing effect. Solar-tracking of the system was done manually.

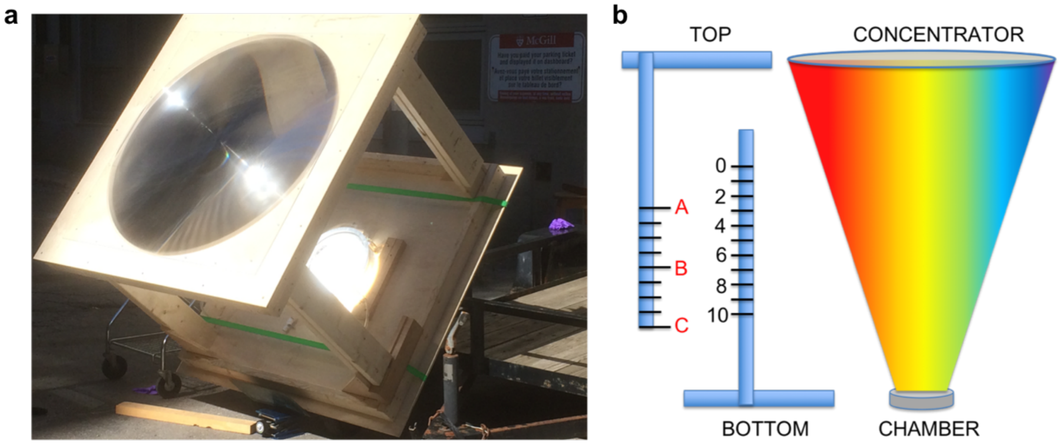

Figure 5-8: (a) Experimental setup of large-scale artificial photosynthesis using Fresnel lens. **(b)** Schematic illustration of the solar concentration mechanism, demonstrating the adjustable concentration ratio by varying the relative position between the top and bottom parts of the wooden frame.

5.2.3. Results

On the Reproducibility and Repeatability of Ga(In)N Nanowire Devices

The structural reproducibility and performance repeatability of the nanowire devices have been investigated carefully, and the influencing factors on the large-scale realization have been analyzed. As shown in Figure 5-9a, three different devices (A, B and C) synthesized and processed under identical conditions exhibit similar gas evolution rates in unassisted overall water splitting under concentrated irradiation using 300 W Xenon lamp. Scaling up and optimization of the device processing and performance evaluation are substantially challenging due to the non-linear influences of a number of determining factors; namely, the duration of synthesis, nanowire morphology and fluctuation of In composition due to the temperature gradient. The distribution of cocatalyst nanoparticles on the nanowire surfaces of the device depends on the light intensity, duration of photo-excitation and the amount of precursor loading during the photodeposition (discussed above).

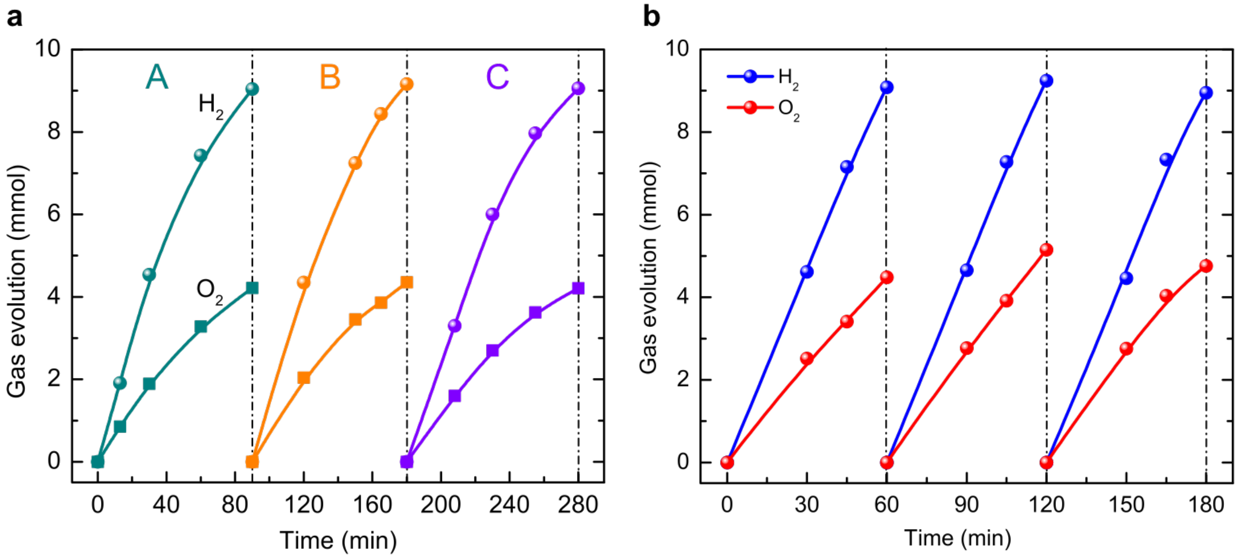

Figure 5-9: Reproducibility and performance repeatability of Ga(In)N nanowire devices. **(a)** Time evolution of stoichiometric H_2 and O_2 evolution in unassisted pure (pH ~7.0) water splitting on reproducible *p*-GaN/InGaN nanowire samples. The nanowires were grown on Si wafers, then

decorated with dual-cocatalysts (Co_3O_4 + Rh/Cr_2O_3, not optimized) and tested under concentrated full-arc irradiation (27 suns) while illuminating whole wafer. **(b)** Performance repeatability of the double-band *p*-GaN/InGaN nanowire heterostructures, tested under same conditions after further optimization of co-catalyst loading.

Significantly, the performance and stability of the dual-cocatalyst decorated double-band *p*-GaN/InGaN nanowire devices can be demonstrated at larger scale, as shown in Figure 5-9b. The device (active area ~40 cm^2) was immersed into pure water (thickness ~10-12 mm, pH ~7.0) and was tested for hydrogen evolution under concentrated irradiation using a 300W Xenon lamp. However, due to the limitation of the beam size from the light source, the device exposure to photo-excitation was limited to an effective area of ~13-18 cm^2. With an average light intensity of ~20 suns or less on the sample surface, the rate of hydrogen evolution from unassisted overall water splitting was measured to be ~9.08 $mmol \cdot h^{-1}$, and the STH efficiency can be estimated as ~1.7-2.3%. The efficiency is slightly lower than that from the devices processed and tested at smaller scale [200], which can be attributed to the non-uniform photon distribution within the larger beam and comparatively lower overall light intensity on the sample surface.

Unassisted Water Splitting on Ga(In)N under Concentrated Sunlight

The device was further tested under natural sunlight using a solar concentrator to create high-intensity light source. The illumination intensity (and area of exposure) can be tuned by changing the sample position (Figure 5-8b). The experiments under real sunlight have been performed during Fall, within the time-span of ~11:00-14:30 on sunny days having intermittent clouds, thereby requiring vertical tilt in the range of 20°-40° (Montreal) for minimum energy losses. The ambient temperature in Montreal in this time period fluctuated significantly within the broad range of 4-18 °C. The reproducibility of the nanowire devices and the consistent photocatalytic activity of the system have been demonstrated, as shown in Figure 5-10.

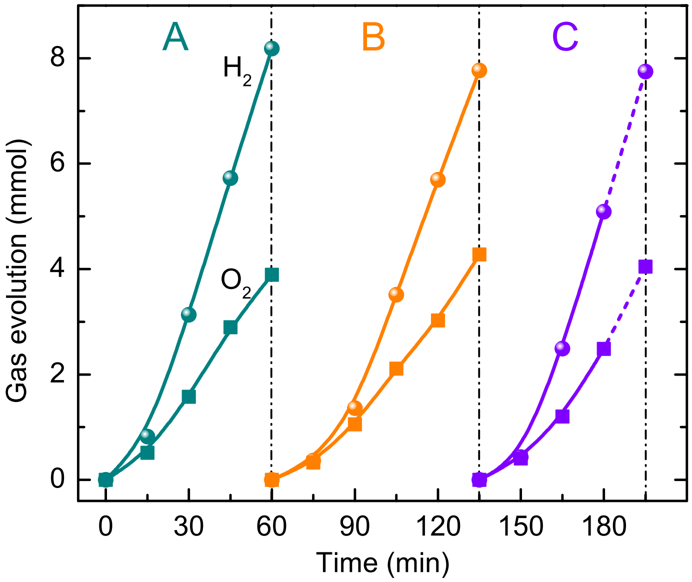

Figure 5-10: Reproducible time course of stoichiometric H_2 and O_2 evolution in unassisted overall pure water splitting on *p*-GaN/InGaN nanowires decorated with dual-cocatalyst (Co_3O_4 + Rh/Cr_2O_3) under concentrated natural sunlight with intensity of ~60 suns. The third cycle was interrupted by intermittent cloud (dotted line) but shows comparable trend of linear gas evolution.

To minimize the gradient in the photon density, the intense focal spot with area of ~10 cm^2 and average intensity of ~60 suns has been used for the photo-excitation of the device. Consequently, hydrogen evolution rate of 9.8 $mmol \cdot h^{-1}$ has been derived, resulting in STH conversion efficiency of ~1.1%. The initial plateau in hydrogen evolution and overall reduction in STH efficiency can be attributed to the large volume (4.0 L) and thickness (~64 mm) of water used due to the vertical tilt of the reaction chamber corresponding to the zenith angle of the excitation source. In the wavelength range of 200-480 nm, the AQE and ECE were derived to be ~17.2% and 7.1%, respectively. The hydrogen evolution rate (~1.0 $mmol \cdot h^{-1} \cdot cm^{-2}$, STP equivalent of 22.4 $mL \cdot h^{-1} \cdot cm^{-2}$) and STH efficiency (~1.1%) derived herein are significantly higher compared to that of ~0.6 mL·h^{-1}·cm^{-2} and ~0.3-0.4%, respectively, which were reported from unassisted overall water splitting under nominal sunlight while using a device with area of ~25 cm^2 with threshold wavelength of ~390 nm (E_g ~ 3.2 eV) and water thickness of ~1mm [201].

5.3. Intensity Dependent Photocatalytic Performance of GaN/InGaN Nanowires

To find out the underlying reasons for efficiency fluctuations at different conditions, we have investigated the influence of light intensity on the photocatalytic performance of Ga(In)N nanostructures. Small devices (area ~1 cm^2) were used to eliminate the problems related to the non-uniform distribution of photons on the sample surface. The incident light intensity on the photocatalyst surface were varied by adjusting the device position, while keeping the thermal energy transfer, chamber pressure and other conditions identical. The performance evaluation of dual-cocatalyst loaded InGaN nanowire device in OWS using a 300 W Xenon lamp is presented in Figure 5-11 as a function of incident light intensity, which can be correlated to the photogenerated charge carrier density inside the semiconductor nanowires.

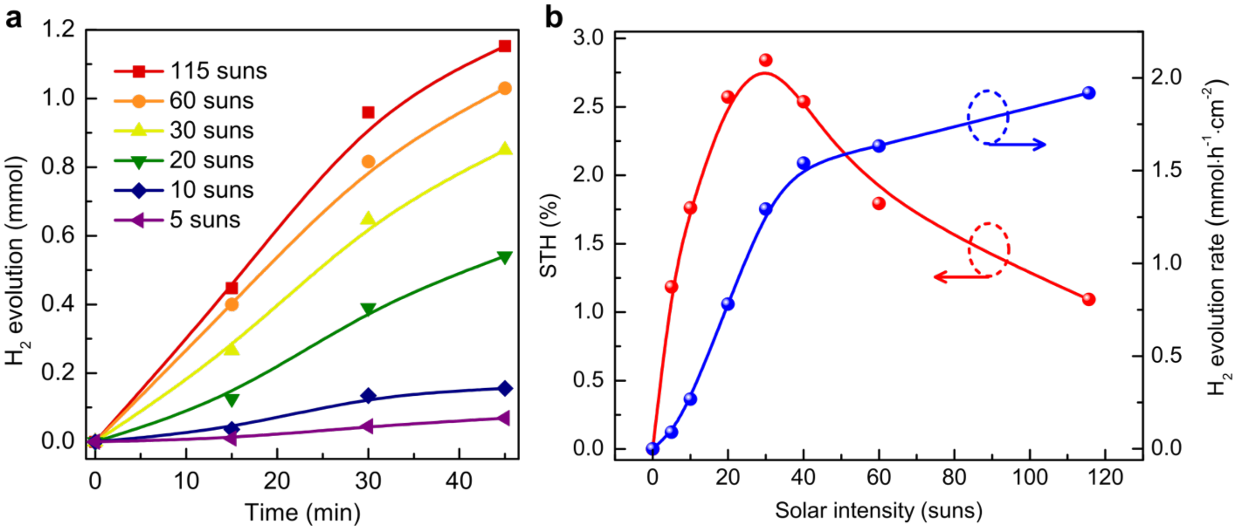

Figure 5-11: (a) The evolution of hydrogen versus time from unassisted overall water splitting as a function of light intensity (using 300 W Xenon lamp) on the dual-cocatalyst coated *p*-GaN/InGaN nanowire devices (area ~1 cm^2). **(b)** Average rate of H_2 production from overall pure water splitting and corresponding STH efficiency – as a function of incident light intensity.

In low light-intensity regime (< 30 suns), the STH efficiency and hydrogen evolution rate increase drastically with increasing light intensity. This can be attributed to the abundance of readily available photo-generated carriers within the semiconductor, followed by their efficient migration from the bulk due to reduced surface band-bending, and their efficient separation and trapping into the cocatalyst nanoparticles on the nanowire surfaces. The STH efficiency, however, decreases at very high photon intensity (as shown in Figure 5-11b) as a result of the apparent plateau in the hydrogen evolution rate. This can be ascribed to the enhanced electron-hole recombination at high intensity illumination either in the bulk or at the surface of the semiconductor due to the limited distribution of cocatalyst particles [194, 202] and comparatively slower water-splitting rate that is limited by sluggish mass transfer and multi-hole water oxidation dynamics [203]. Other possible reasons may include reduced reaction sites due to relatively enhanced bubbling effect (H_2 and O_2) at higher irradiation intensity [203]. As depicted in Figure

5-11b, the dual-cocatalyst decorated double-band GaN/InGaN nanowires exhibited a maximum STH efficiency of ~2.8% for overall pure water splitting under concentrated illumination equivalent to ~30 suns, without any external bias or sacrificial reagent. The reduction in STH efficiency at higher excitation intensity is similar to the efficiency-droop typically observed in III-nitride based visible light-emitting devices at higher injection current [204].

5.4. Discussion

Scaling up the synthesis of an efficient and stable visible-light driven photocatalyst on large-area substrate is critically important for large-scale hydrogen production. However, it is also crucial to minimize the usage of light absorber for energy balance and additional benefits, without compromising the gas evolution rate or the yield of the system. Apparently, wafer-level photocatalytic devices operated under concentrated sunlight can mitigate numerous design challenges compared to the systems that are intended to operate under nominal sunlight. Additional striking features of the wafer-level artificial photosynthesis system include recycling flexibility of the substrates, ease of scale-up by stacking photocatalytic devices in two-dimensional matrix on a panel (Figure 5-7) and selective replacement of damaged/decayed device from a larger array of wafers without perturbing the overall system. As the energy balance and expected benefits of large-scale overall system is fundamentally regulated by the light absorber, the minimalist design to operate the system under concentrated sunlight can efficiently function using smaller device-area and less amount of water to reduce the balance of system (BoS) cost significantly. Most widely explored compound parabolic concentrator (CPC) system consists of a tubular reactor that contains particulate photocatalysts solution and operates under limited concentration ratio (<10) while exhibiting very low efficiency [205]. However, particulate systems require additional complexities for maintaining turbulence inside the reactor to avoid precipitation and aggregation of the photocatalyst, which further limits the absorption efficiency, and face challenges in terms of efficient gas release through the tube to avoid bubbling or shadowing effect and post-reaction recycling of the photocatalysts.

Surface-engineered wafer-level Ga(In)N nanowires, when loaded with suitable co-catalysts (Rh/Cr_2O_3 for HER and Co_3O_4 for OER), can successfully withstand the photo-corrosion, while demonstrating significantly enhanced STH conversion efficiency and long-term stability (over 580 hours) during overall water splitting under concentrated sunlight [200]. The AQE and ECE in the visible range of 400-480 nm for the current devices are also significantly higher than previously reported values, which can further be correlated to the longer InGaN segments in nanowires (70-100 nm compared to previous 40-50 nm each) and increased nanowire fill-factor on the substrate. Given the limited absorption efficiency of most photocatalysts, employing concentrated sunlight on an integrated, wafer-level photocatalyst can increase the generation rate, cumulative density and the trapping of charge-carriers into co-catalyst nanoparticles without proportionally increasing the active area of the device. However, efficiency enhancement does not exhibit linear relationship with excitation intensity, as shown in Figure 5-11b. Therefore, the device needs to be operated under the optimum window of excitation intensity (equivalent to ~25-35 suns, with minimized gradient or fluctuation on the sample surface) for maximum throughput. Ga(In)N nanowire heterostructures on cheap Si wafers are both air- and water-stable owing to their N-rich surfaces and efficient co-catalyst loading. The proximity of the nanowire photocatalysts, including the integrated nature of micro-/nanoelectrodes (co-catalysts) greatly eliminates the problem of ionic diffusion for balanced water splitting reaction. Therefore, these nanostructures can efficiently generate hydrogen from unassisted photocatalytic neutral pH water splitting at larger scale, without encountering the obstacles typically observed in PEC systems, such as the reduction of current density and device efficiency at larger scale compared to the laboratory grade small scale devices [206].

5.5. Conclusion

We have demonstrated the ability to fabricate industry-friendly artificial photosynthesis devices consisting of GaN-alloys on Si wafers and showed that the processing of dual-cocatalyst loaded double-band *p*-GaN/InGaN nanowire devices can be successfully scaled up for efficient and stable hydrogen generation via unassisted pure water splitting under concentrated sunlight. The device is reproducible at larger scale with significantly enhanced solar-to-hydrogen conversion efficiency and stability during the spontaneous photocatalytic reaction. Our intensity dependent measurements on the photocatalytic performance of similar device reveals critical insights for the large-scale design and optimization of artificial photosynthesis system. This study suggests that with careful structural engineering of the photocatalyst and further improvement in the system design, e.g., optimizing the solar concentration ratio and water thickness to minimize energy losses, the solar-to-hydrogen conversion efficiency of the system can be enhanced further during large-scale water splitting under concentrated real sunlight. The material development at the ‘nanoscale’ for higher efficiency and stability should therefore, go in parallel with the system development at ‘large-scale’ for the prior-identification of the challenges.

Chapter 6: Conclusion and Future Work

6.1. Summary of the Thesis Work

In the course of this thesis work, we have elucidated the underlying mechanisms for high efficiency UV LEDs based on AlN nanowires and efficiency droop in monolayer MoS_2 light-emitting devices. Further studies on the optical properties of few-layer MoS_2 have led to the first demonstration of optically pumped lasers operating at room temperature from 2D TMDCs. Moreover, we have successfully scaled up the synthesis of GaN-based nanostructures on Si substrate for the demonstration of large-scale photocatalytic water splitting under natural sunlight. In what follows, we highlight the major findings of this thesis.

Despite the enormous development of III-nitrides based light sources operating in the UV-B/C bands, the device performance of AlGaN planar structures has been severely limited by the prohibitively high dislocation densities and low doping efficiency (specifically, *p*-type), which are due to the lack of lattice-matched substrate and the large activation energy of the common Mg dopant, respectively. By employing relatively strain-free AlN nanowires grown on Si substrate, a record electrical efficiency over 85% has been reported [36]. However, what actually leads to such unusually efficient (*p*-type) doping in AlN nanostructures was still unclear until the investigation of hole hopping conduction in this thesis. Detailed studies on the carrier transport in single AlN nanowire transistor via temperature-dependent measurements reveal the efficient hole hopping conduction in the Mg impurity band, evident from the low activation energy (~20 – 200 meV) at room temperature and the increase in hole mobility with increasing temperature, that results in a room-temperature free hole concentrations up to $\sim 6 \times 10^{17}$ cm^{-3}. This is primarily due to the reduced Mg formation energy stem from the surface strain relaxation in nanowire structures. In addition, the hole conduction in the valance band is also observed, which is attributed to the broadening of the Mg acceptor energy level.

We have further gained insight into the optical properties of emerging 2D TMDC materials, MoS_2 in particular, for the realization of ultralow threshold lasers operating under continuous wave at room temperature. Through temperature- and power-dependent PL measurements on monolayer MoS_2 flake fabricated by means of mechanical exfoliation on Si/SiO_x substrate, we have derived the maximum achievable internal quantum efficiency of 45% at 83 K, which can be explained by the significantly enhanced correlation between electrons and holes in 2D structure, evidenced by the very large calculated radiative recombination rate ($\sim10^{-7}$ $cm^3 \cdot s^{-1}$). Moreover, efficiency droop is clearly measured in monolayer MoS_2 light-emitting devices with increasing carrier injection due to the unusually large Auger recombination coefficient, which is on the order of 10^{-24} $cm^6 \cdot s^{-1}$ at room temperature. In contrast, 4L MoS_2 possesses a much weaker Auger effect, making it a good choice to achieve larger optical confinement. We have consequently designed a vertically coupled silica microsphere/SiO_2 microdisk optical cavity with 4L MoS_2 gain medium. The threshold power is remarkably low (~5 μW), and no saturation is observed for pumping power up to 1 mW.

Not only exhibiting critical impacts on the development of optoelectronics devices, but III-nitride nanowires also have proved to be an excellent candidate as a viable photocatalyst for efficient and stable overall water splitting. Although tremendous efforts have been devoted to improving the STH efficiency and stability of III-nitride based photocatalyst for photocatalytic water splitting, there has been no reports on large-scale demonstration under natural sunlight. Overcoming the significant challenges of scaling up nanowire synthesis on larger Si wafer, we have achieved highly efficient *p*-GaN/InGaN nanowire devices grown on 3”-Si substrates, which shows an AQE of ~28% in the visible range (400 – 480 nm). Furthermore, we have successfully demonstrated large-scale hydrogen generation from unassisted photocatalytic neutral pH water splitting under concentrated natural sunlight and obtained a STH energy conversion efficiency of ~1.1%, which is, to our knowledge, the best value reported so far.

6.2. Suggested Future Work

In the sections below, we propose future directions towards the realization of smooth, nearly dislocation-free AlN thin films grown on sapphire substrate, and the fabrication of GaN quantum wire transistors. In addition, we aim to further optimize the reaction chamber as well as natural sunlight setting in parallel with the development of photocatalyst materials for the development of viable alternatives to carbon-rich fossil fuels.

6.2.1. AlN Epilayers through Controlled Nanowire Coalescence for Nearly Dislocation-Free Planar Deep Ultraviolet Photonic Devices

The device performance of wide-bandgap III-nitride based LEDs, lasers, and transistors strongly depends on the quality of materials. To date, however, AlGaN has been known to suffer from high dislocation density and large polarization fields [207-211]. In addition, the lack of low-cost, high-quality substrates has limited the progress in this field. Alternatively, nanowire heterostructures can be used to overcome these challenges, thanks to the surface stress relaxation, and nearly free of dislocation. To date, research on nanowire-based deep UV LEDs, however, has been facing serious problems associated with surface passivation and planarization due to UV absorption of polyimide. Attempts have been made to form free-standing epilayer on coalesced nanowires [212, 213]. Nonetheless, these nanowires are spontaneously grown on substrates and hence mis-oriented, leading to the presence of strain, grain boundaries, and structural defects [214-217]. Recently, nearly dislocation-free AlGaN films have been grown on sapphire substrates through controlled GaN/AlGaN nanowire coalescence using selective area epitaxial growth. The film structures exhibit excellent *p*-type conduction, involving a room-temperature free hole concentration and mobility of ~7.4 × 10^{18} cm^{-3} and ~8.85 $cm^2/V{\cdot}s$, respectively [218]. In this context, we propose to grow AlN epilayers on sapphire substrate by employing similar approach. The use of SAG technique provides a precise control of the size, position, and orientation of nanowires, minimizing the formation and propagation of dislocations in both nanowire templates and thin films.

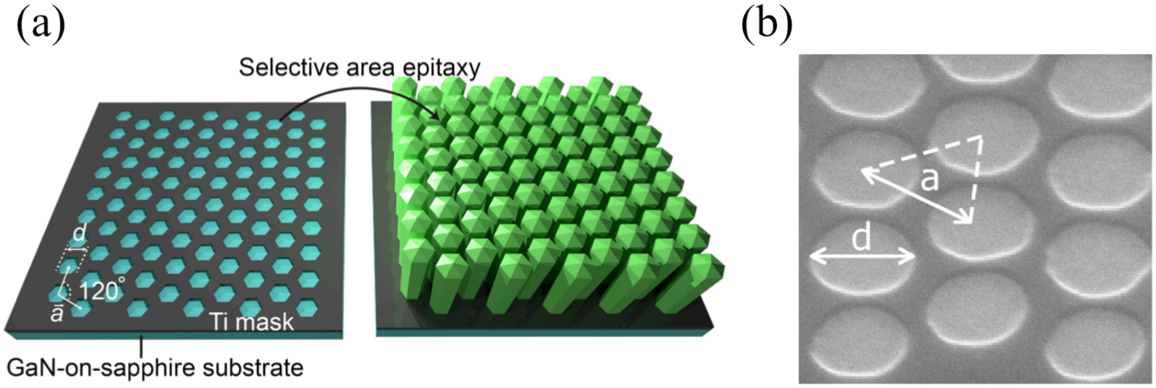

Figure 6-1: (a) Schematic diagram of selective area growth process *. (b) An SEM image of nano-patterned substrate.
*Illustration prepared by Dr. Huy Binh Le.

Illustrated in Figures 6-1(a) and (b) are the schematic diagram of selective area growth process and an SEM image of nano-patterned substrate. The opening apertures can be defined by standard EBL and dry etching processes on a Ti mask deposited on *n*-GaN/sapphire substrate. Undoped GaN nanowires will be first grown, followed by the growth of Si-doped *n*-AlN. Figure 6-2 shows SEM image of an as-grown AlN thin film with smooth surface. However, some cracks are still visible, which can be attributed to strain in 2D structures. It has been proved that quasi-3D semipolar surface offers several advantages over 2D surface, including enhanced Mg-dopant incorporation [219], reduced polarization fields and efficient strain relaxation [220]. Therefore, we believe that further careful optimization of the growth conditions can lead to the formation of semipolar AlN films with superior optical and electrical properties.

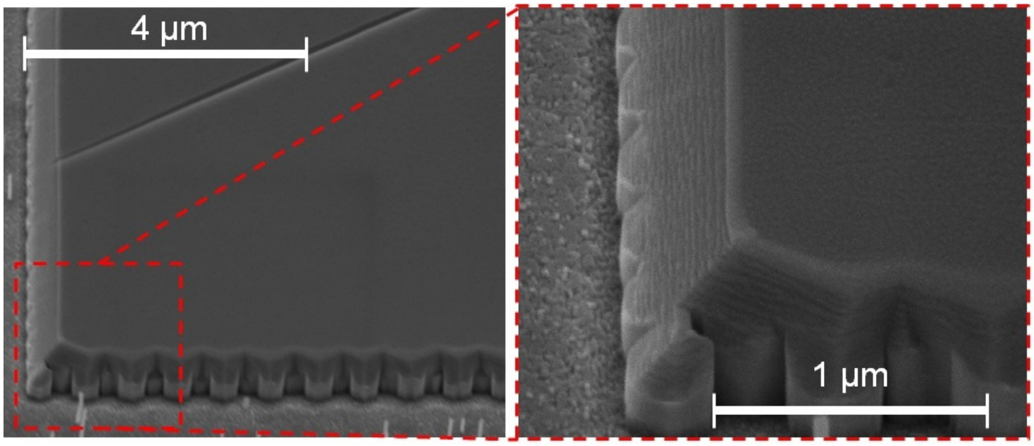

Figure 6-2: SEM image of coalesced AlN:Si thin film on sapphire substrate.

6.2.2. GaN Quantum Wire Transistors

Quantum wire transistor is one of the most promising technologies to continue the scaling of device density in semiconductor industry [221, 222]. Silicon has been widely used for the fabrication of quantum wire transistors due to its low-cost and maturity in processing and integration [222-225]. However, devices based on III-V materials are believed to outperform the Si devices in high speed logic transistor applications [226]. Here, we propose the fabrication of GaN quantum wire transistors using top-down approach.

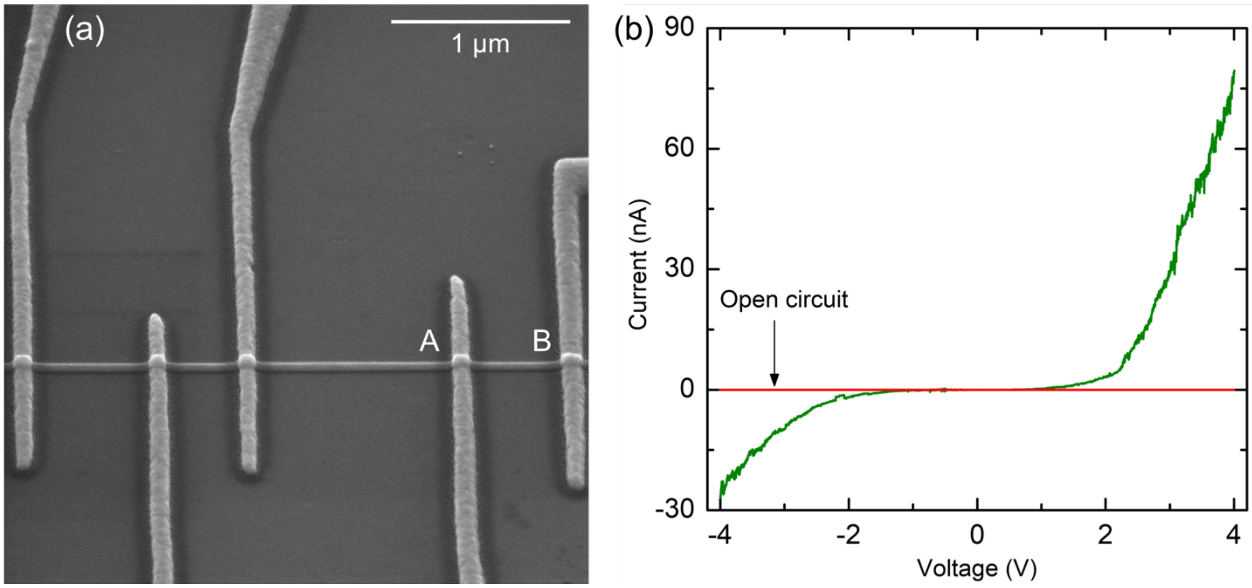

Figure 6-3: (a) 45°-tilted SEM image of a fabricated GaN quantum wire device. **(b)** I-V characteristic (green) of the device when sourcing current through A-B contacts denoted in (a).

GaN:Si film with a thickness of ~35 nm is grown on AlN/sapphire substrate by plasma-assisted MBE. To promote the lateral growth of GaN thin film on sapphire, a thin AlN buffer layer is grown first [227]. The quantum wire is then defined by standard EBL using negative e-beam resist. Dry etching by RIE and subsequent wet etching in KOH result in smooth surface of the quantum wires, as shown in Figure 6-3a. The e-beam resist is removed by RIE. After that, metal contacts are fabricated by using EBL and metallization processes. I-V characteristic of the fabricated device (Figure 6-3b) when biasing two adjacent contacts clearly shows the conduction in GaN quantum wire. In this work, we also propose two designs of the gates as schematically illustrated in Figure 6-4.

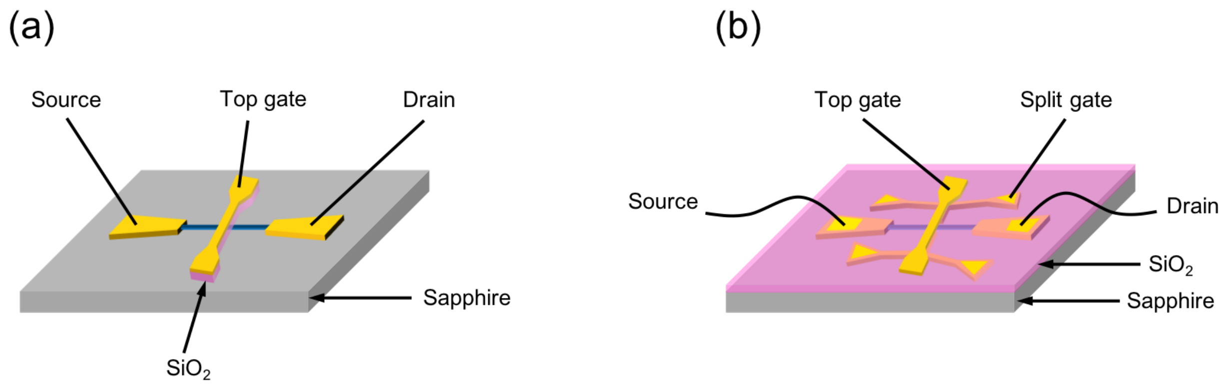

Figure 6-4: (a) *Design 1*: Top-gated GaN quantum wire transistor. **(b)** *Design 2*: GaN quantum wire transistor with both top- and split-gates.

In *Design 1*, the source (S) and drain (D) contacts will be defined by EBL, followed by metallization. Subsequently, SiO_2 is deposited on top of the sample using e-beam evaporator, which offers better quality than plasma-enhanced chemical vapor deposition (PECVD) in terms of smoothness and uniformity. Finally, top gate will be fabricated and also serves as a mask for the SiO_2 etching step in RIE chamber. The fabrication of *Design 2* is similar to that of *Design 1* except that the S, D and split-gate will be deposited at the same time, followed by SiO_2 deposition and then fabrication of the top-gate and window areas opened on top of the contact pads.

There are certain challenges that need to be addressed for the achievement of quantum wire transistor with low resistance (on the order of 10 kΩ), negligible leakage current and operating temperature close to room temperature. For instance, the starting material, i.e., GaN thin film, has to be of high quality to increase the electron mean-free-path. This can be achieved by further careful optimization of the growth conditions. Moreover, the dielectric constant, quality and thickness of the insulating material also play an important role to diminish the leakage current. Instead of using SiO_2, either Al_2O_3, HfO_2, or TiO_2 can be deposited by atomic layer deposition (ALD) for better isolation between gates and channel.

6.2.3. The Next Generation of Photoreactor Design for Multi-wafer Artificial Photosynthesis

As described in Chapter 5, the amount and thickness of pure water used for the outdoor testing is almost 30 and 6 times larger than that for the experiments in lab, respectively. Such heavy weight of water increases the water pressure on the sample, as well as reducing the steady-state reaction temperature (gas evolution rate is constant) under same light intensity, leading to an overall decrease in STH efficiency [189, 201, 228]. In the next generation of reaction chamber, we aim to reduce the water amount/thickness and improve the design for better sealing and ease of operation/maintenance. Major components of the new photoreactor is schematically illustrated in Figure 6-5, and picture of the fabricated chamber is shown in Figure 6-6. To minimize the thickness of water layer on top of the sample, we have utilized aluminum hex standoffs and designed PEEK 'clamps' for the mounting of samples. This new wafer mount system can improve the flow, reduce collateral entrapment of gas bubbles and eliminates the need for relatively expensive PTFE holder. The quartz window mount system will incorporate a side-seal (silicon o-ring) and a PTFE ring on top (not shown in Figure 6-5) to reduce the danger of chipping or cracking due to handling or difference in linear thermal expansion coefficients between aluminum ($\sim 23 \times 10^{-6}$ K^{-1}) and quartz ($\sim 0.6 \times 10^{-6}$ K^{-1}). Moreover, the quartz window is fixed to the chamber, and wafer replacement can be implemented by removing the base at up-side down position without draining off the water. This means of changing wafer is much simpler and time-saving. With the above-described improvements of the new photoreactor over the preliminary design, there should be no doubt about the success of this project, which will provide important economic and societal benefits.

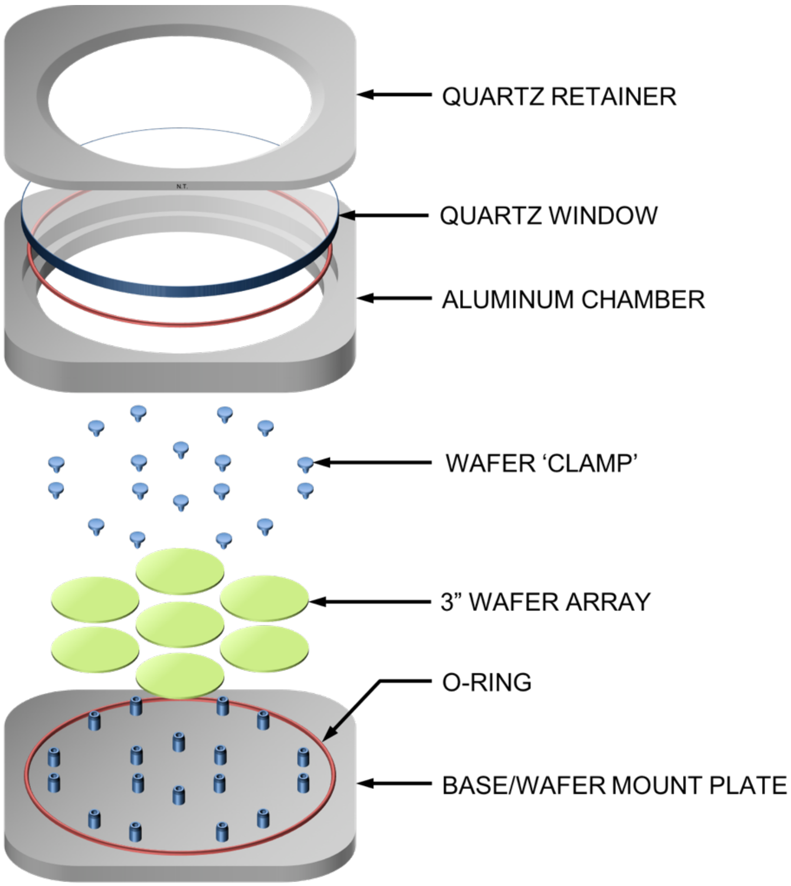

Figure 6-5: Schematic presentation of a 7-wafer photoreactor (major components) for realization of large-scale photocatalytic overall pure water splitting.

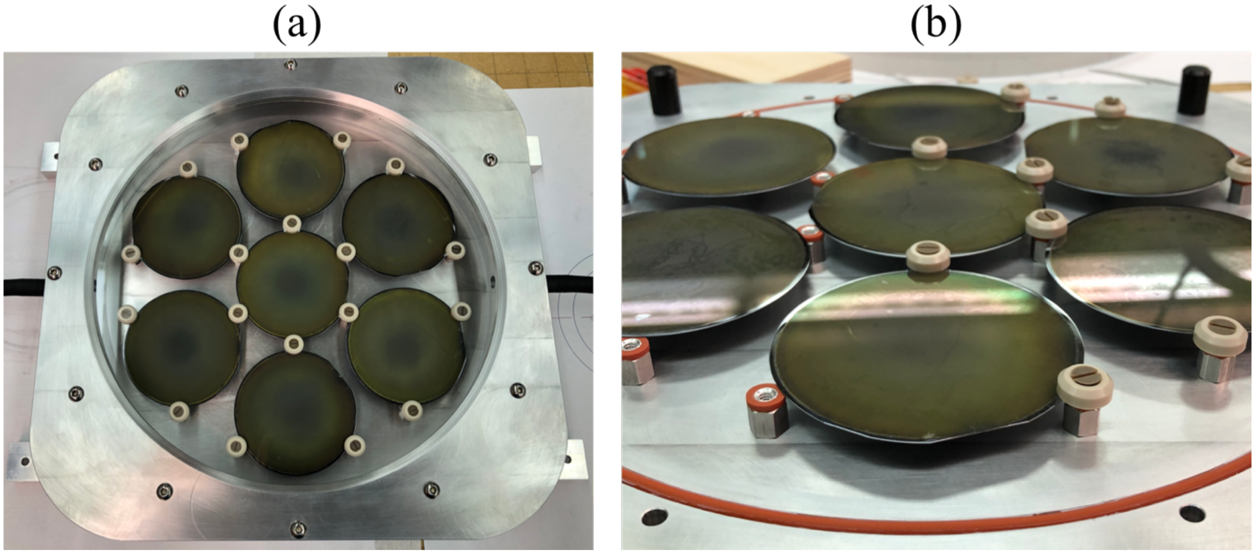

Figure 6-6: (a) Aluminum chamber fabricated at McGill University, Montreal, Canada, which has capability of mounting 7 (3”) Si wafers and adjusting water layer thickness down to 6 – 8 mm on top of the samples. (b) A close look at the wafer mount system.

In the same time, we also develop new designs of the single-wafer chamber and natural sunlight testing system by employing parabolic trough reflector (Figure 6-7). Half of the chamber will have ‘oval-like’ shape to help facilitate the gas evolution at relatively high rate. In addition, the utilization of parabolic trough reflector/concentrator can eliminate the non-uniform convergence and chromatic aberrations problems commonly observed in Fresnel lens [229, 230].

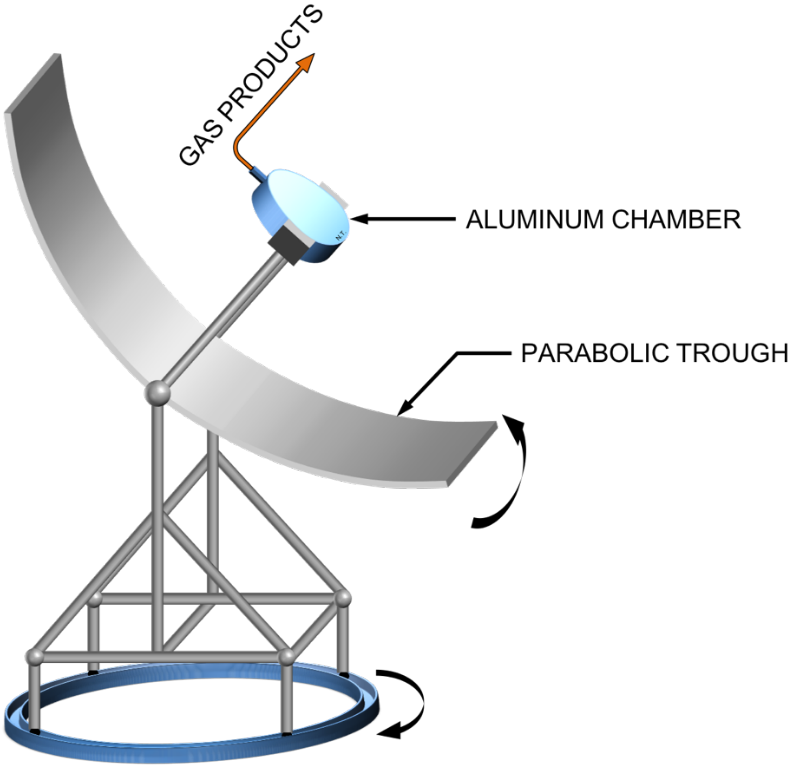

Figure 6-7: Proposed design of a natural sunlight setting using parabolic trough concentrator and single-wafer aluminum chamber. The system can be feasibly scaled up by increasing the length of the reflector and building multiple chambers in series.

List of Publications And Copyrights

Referred and Archival Journal Publications

1. F. A. Chowdhury*, **N. H. Tran***, M. L. Trudeau, Y. Wang, R. Rashid, H. Guo, and Z. Mi, "Sunlight Driven Large-scale Photocatalytic Water Splitting using GaN-alloys", under preparation (2019). [‘*’ *co-first authors*]
2. B. H. Le, X. Liu, A. Mark, **N. H. Tran**, G. A. Botton, and Z. Mi, "An Electrically Injected AlGaN Quantum Dot Ultraviolet Plasmonic Laser Operating at Room Temperature", submitted to ***Nature Photonics*** (2019).
3. B. H. Le, X. Liu, **N. H. Tran**, and Z. Mi, “An Electrically Injected AlGaN Nanowire Defect-free Photonic Crystal Ultraviolet Lasers”, ***Optics Express*** 27, 5843 – 5850 (2019).
4. **Nhung Hong Tran**, Binh Huy Le, Songrui Zhao, and Zetian Mi, “On the mechanism of highly efficient p-type conduction of Mg-doped ultra-wide-bandgap AlN nanostructures”, ***Applied Physics Letters*** 110, 032102 (2017).
5. David Arto Laleyan, Songrui Zhao, Steffi Y. Woo, **Hong Nhung Tran**, Huy Binh Le, Thomas Szkopek, Hong Guo, Gianluigi A. Botton, and Zetian Mi, “AlN/h-BN Heterostructures for Mg Dopant-Free Deep Ultraviolet Photonics”, ***Nano Letters*** 17, 3738 – 3743 (2017).
6. Binh Huy Le, Songrui Zhao, **Nhung Hong Tran**, Thomas Szkopek, and Zetian Mi, “On the Fermi-level pinning of InN grown surfaces”, ***Applied Physics Express*** 8, 061001 (2015).

7. O. Salehzadeh, **N. H. Tran**, X. Liu, I. Shih, and Z. Mi, "Exciton Kinetics, Quantum Efficiency, and Efficiency Droop of Monolayer MoS_2 Light-Emitting Devices", ***Nano Letters*** 14, 4125 – 4130 (2014).
8. Omid Salehzadeh, Mehrdad Djavid, **Nhung Hong Tran**, Ishiang Shih, and Zetian Mi, "Optically Pumped Two-Dimensional MoS_2 Lasers Operating at Room-Temperature", ***Nano Letters*** 15, 5302 – 5306 (2015).
9. Binh Huy Le, Songrui Zhao, **Nhung Hong Tran**, and Zetian Mi, "Electrically injected near-infrared light emission from single InN nanowire p-i-n diode", ***Applied Physics Letters*** 105, 231124 (2014).
10. Binh Huy Le, Shamsul Arafin, **Nhung Hong Tran**, Hieu Pham Trung Nguyen, and Zetian Mi, "Current-Voltage Characteristics of Single InGaN/GaN Nanowire LEDs", ***10th International Conference on Nitride Semiconductors***, Washington, D.C, United States of America, (August 25-30, 2013) (Conference paper).
11. **Nhung Hong Tran**, Binh Huy Le, Shizhao Fan, Songrui Zhao, Zetian Mi, Benjamin A. Schmidt, Michel Savard, Guillaume Gervais, and Kenneth Scott A. Butcher, "Optical and structural characterization of nitrogen-rich InN: Transition from nearly intrinsic to strongly n-type degenerate with temperature", ***Applied Physics Letters*** 103, 262101 (2013).

Conference/Meeting Presentations

1. **Nhung H. Tran**, Faqrul A. Chowdhury, Michel L. Trudeau, and Zetian Mi, "Unassisted Artificial Photosynthesis using GaN-alloys: Scaling up Ga(In)N Nanowire Synthesis for Large-scale Water Splitting under Real Sunlight", ***21st Photonics North Conference***, Quebec City, Canada, May 21 – 23, 2019 (Oral presentation).

2. Faqrul A. Chowdhury, **Nhung H. Tran**, Hong Guo, and Zetian Mi, “On the Efficiency and Long-term Stability of MBE-grown III-Nitride Nanostructures for Unassisted Overall Water Splitting”, ***34th North American Molecular Beam Epitaxy Conference***, Banff, Alberta, Canada, September 30 – October 5, 2018.
3. D. A. Laleyan, S. Zhao, B. H. Le, **N. H. Tran**, and Z. Mi, “AlN/BN Nanowire Heterostructures for High Efficiency Deep Ultraviolet Photonics”, ***58th Electronic Materials Conference***, Delaware, 2016.
4. **N. H. Tran**, S. Zhao, B. H. Le, and Z. Mi, “Impurity-band Conduction in Mg-doped AlN Nanowires”, ***31st North American Molecular Beam Epitaxy Conference***, Mayan Riviera, Mexico, October 4-7, 2015.
5. B. H. Le, S. Zhao, **N. H. Tran**, T. Szkopek, and Z. Mi, “Demonstration of p-type InN Nanowires: Electrical Transport Properties and Near-infrared Electroluminescence Emission”, ***57th Electronic Materials Conference***, Ohio State University, 2015.
6. B. H. Le, S. Zhao, **N. H. Tran**, T. Szkopek, and Z. Mi, “Mg-doped InN nanowires: p-Type conduction and ambipolar behaviors”, ***18th International Conference on Molecular Beam Epitaxy***, Arizona, 2014.
7. **N. H. Tran**, B. H. Le, H. P. T Nguyen, and Z. Mi, “Optical and Electrical Characteristics of Single InGaN/GaN Nanowire LEDs”, ***25th Canadian Materials Science Conference***, McGill University, Montreal, Canada, June 17-19, 2013 (Poster presentation).
8. **N. H. Tran**, B. H. Le, S. Zhao, Z. Mi, and K. S. A. Butcher, “Unusual Photoluminescence Emission at ~0.68 eV from Nonstoichiometric InN:N”, ***16th Canadian Semiconductor Science and Technology Conference***, Thunder Bay, Canada, August 12-16, 2013 (Poster presentation).

9. B. H. Le, **N. H. Tran**, H. P. T. Nguyen, and Z Mi, "Current-Voltage Characteristics of Single InGaN/GaN Nanowire LEDs", ***10th International Conference on Nitride Semiconductors***, Washington D.C, August 25-30, 2013.

10. B. H. Le, **N. H. Tran**, H. P. T. Nguyen, and Z Mi, "InGaN/GaN Dot-in-a-Wire Intermediate-Band Solar Cell Devices", ***30th North American Molecular Beam Epitaxy Conference***, Banff, Alberta, 2013.

Awards

1. Best student presentation award for poster presentation "Impurity-band Conduction in Mg-doped AlN Nanowires", ***31st North American Molecular Beam Epitaxy Conference***, Mayan Riviera, Mexico, October 4-7, 2015.
2. Winner in Photo Contest 2018 for Nanoscale Devices sponsored by CMC Microsystems. Winning photos will be used to showcase innovations developed in MNT laboratories across Canada.
3. Graduate Teaching Workshop, McGill University, 2014.

References

[1] L. Kemény, Z. Csoma, E. Bagdi, A. Banham, L. Krenács, and A. Koreck, "Targeted phototherapy of plaque-type psoriasis using ultraviolet B–light-emitting diodes," *Br. J. Dermatol.,* vol. 163, pp. 167-173, 2010.

[2] M. Schreiner, J. Martínez-Abaigar, J. Glaab, and M. Jansen, "UV-B Induced Secondary Plant Metabolites: Potential benefits for plant and human health," *Optik & Photonik,* vol. 9, pp. 34-37, 2014.

[3] S. Vilhunen, H. Särkkä, and M. Sillanpää, "Ultraviolet light-emitting diodes in water disinfection," *Environ. Sci. Pollut. R.,* vol. 16, pp. 439-442, 2009.

[4] S.-J. Kim, D.-K. Kim, and D.-H. Kang, "Using UVC light-emitting diodes at wavelengths of 266 to 279 nanometers to inactivate foodborne pathogens and pasteurize sliced cheese," *Appl. Environ. Microbiol.,* vol. 82, pp. 11-17, 2016.

[5] P. J. Hargis Jr, T. Sobering, G. C. Tisone, J. S. Wagner, S. A. Young, and R. Radloff, "Ultraviolet fluorescence identification of protein, DNA, and bacteria," in *Optical Instrumentation for Gas Emissions Monitoring and Atmospheric Measurements*, vol. 2366, pp. 147-153, 1995.

[6] "UV LED industry: over 10-years development, market share has trebled," *http://www.yole.fr/2018_press_releases.aspx*, 2018.

[7] S. Strite and H. Morkoç, "GaN, AlN, and InN: a review," *J. Vac. Sci. Technol. B,* vol. 10, pp. 1237-1266, 1992.

[8] H. Hirayama, S. Fujikawa, and N. Kamata, "Recent progress in AlGaN-based deep-UV LEDs," *Elec. Commun. Jp.,* vol. 98, pp. 1-8, 2015.

[9] M. Kneissl, T.-Y. Seong, J. Han, and H. Amano, "The emergence and prospects of deep-ultraviolet light-emitting diode technologies," *Nat. Photonics,* vol. 13, p. 233, 2019.

[10] H. Hirayama, S. Fujikawa, N. Noguchi, J. Norimatsu, T. Takano, K. Tsubaki, and N. Kamata, "222–282 nm AlGaN and InAlGaN-based deep-UV LEDs fabricated on high-quality AlN on sapphire," *Phys. Status Solidi A,* vol. 206, pp. 1176-1182, 2009.

[11] H. Yoshida, Y. Yamashita, M. Kuwabara, and H. Kan, "Demonstration of an ultraviolet 336 nm AlGaN multiple-quantum-well laser diode," *Appl. Phys. Lett.,* vol. 93, p. 241106, 2008.

[12] M. L. Nakarmi, N. Nepal, C. Ugolini, T. M. Altahtamouni, J. Y. Lin, and H. X. Jiang, "Correlation between optical and electrical properties of Mg-doped AlN epilayers," *Appl. Phys. Lett.,* vol. 89, p. 152120, 2006.

[13] K. B. Nam, M. L. Nakarmi, J. Li, J. Y. Lin, and H. X. Jiang, "Mg acceptor level in AlN probed by deep ultraviolet photoluminescence," *Appl. Phys. Lett.,* vol. 83, pp. 878-880, 2003.

[14] Y. Taniyasu, M. Kasu, and T. Makimoto, "An aluminium nitride light-emitting diode with a wavelength of 210 nanometres," *Nature,* vol. 441, pp. 325-328, 2006.

[15] C. Stampfl, J. Neugebauer, and C. G. Van De Walle, "Doping of $Al_xGa_{1-x}N$ alloys," *Mater. Sci. Eng. B Solid State Adv. Technol.,* vol. 59, pp. 253-257, 1999.

[16] P. Kozodoy, H. Xing, S. P. Denbaars, U. K. Mishra, A. Saxler, R. Perrin, S. Elhamri, and W. C. Mitchel, "Heavy doping effects in Mg-doped GaN," *J. Appl. Phys.,* vol. 87, pp. 1832-1835, 2000.

[17] M. Shatalov, W. Sun, R. Jain, A. Lunev, X. Hu, A. Dobrinsky, Y. Bilenko, J. Yang, G. A Garrett, L. E Rodak, M. Wraback, M. Shur, and R. Gaska, "High power AlGaN ultraviolet light emitters," *Semicond. Sci. Technol.,* vol. 29, p. 084007, 2014.

[18] M. Crawford, "Materials challenges of AlGaN-based UV optoelectronic devices," *Semiconduct. Semimet.*, vol. 96, pp. 3-44, 2017.

[19] S. Yu. Karpov, "Bandgap engineering of III-nitride devices on low-defect substrates," *III-Nitride Devices and Nanoengineering*, pp. 367-397, 2008.

[20] O. Ambacher, "Growth and applications of group III-nitrides," *J. Phys. D: Appl. Phys.,* vol. 31, pp. 2653-2710, 1998.

[21] D. Zhu, D. Wallis, and C. Humphreys, "Prospects of III-nitride optoelectronics grown on Si," *Rep. Prog. Phys.,* vol. 76, p. 106501, 2013.

[22] J. Li, K. B. Nam, M. L. Nakarmi, J. Y. Lin, H. X. Jiang, P. Carrier, and S. -H. Wei, "Band structure and fundamental optical transitions in wurtzite AlN," *Appl. Phys. Lett.,* vol. 83, pp. 5163-5165, 2003.

[23] K. Nam, J. Li, M. Nakarmi, J. Lin, and H. Jiang, "Unique optical properties of AlGaN alloys and related ultraviolet emitters," *Appl. Phys. Lett.,* vol. 84, pp. 5264-5266, 2004.

[24] G. D. Chen, M. Smith, J. Y. Lin, H. X. Jiang, S. -H. Wei, M. A. Khan, and C. J. Sun, "Fundamental optical transitions in GaN," *Appl. Phys. Lett.,* vol. 68, pp. 2784-2786, 1996.

[25] A. Sedhain, J. Lin, and H. Jiang, "Valence band structure of AlN probed by photoluminescence," *Appl. Phys. Lett.,* vol. 92, p. 041114, 2008.

[26] F. Glas, "Critical dimensions for the plastic relaxation of strained axial heterostructures in free-standing nanowires," *Phys. Rev. B,* vol. 74, 121302, 2006.

[27] R. Yan, D. Gargas, and P. Yang, "Nanowire photonics," *Nat. Photonics,* vol. 3, p. 569, 2009.

[28] S. Zhao, M. G. Kibria, Q. Wang, H. P. T. Nguyen, and Z. Mi, "Growth of large-scale vertically aligned GaN nanowires and their heterostructures with high uniformity on SiO_x by catalyst-free molecular beam epitaxy," *Nanoscale,* vol. 5, pp. 5283-5287, 2013.

[29] I. Shalish, G. Seryogin, W. Yi, J. M. Bao, M. A. Zimmler, E. Likovich, D. C. Bell, F. Capasso, and V. Narayanamurti, "Epitaxial catalyst-free growth of InN nanorods on c-plane sapphire," *Nanoscale Res. Lett.,* vol. 4, pp. 532-537, 2009.

[30] M. Tchernycheva, C. Sartel, G. Cirlin, L. Travers, G. Patriarche, J-C. Harmand, L. S. Dang, J. Renard, B. Gayral, L. Nevou, and F. Julien, "Growth of GaN free-standing nanowires by plasma-assisted molecular beam epitaxy: structural and optical characterization," *Nanotechnology,* vol. 18, p. 385306, 2007.

[31] E. Calleja, J. Ristić, S. Fernández-Garrido, L. Cerutti, M. Sánchez-García, J. Grandal, A. Trampert, U. Jahn, G. Sánchez, A. Griol, and B. Sánchez, "Growth, morphology, and structural properties of group-III-nitride nanocolumns and nanodisks," *Phys. Status Solidi B,* vol. 244, pp. 2816-2837, 2007.

[32] Q. Wang, A. T. Connie, H. P. Nguyen, M. G. Kibria, S. Zhao, S. Sharif, I. Shih, and Z. Mi, "Highly efficient, spectrally pure 340 nm ultraviolet emission from $Al_xGa_{1-x}N$ nanowire based light emitting diodes," *Nanotechnology,* vol. 24, 345201, 2013.

[33] S. Zhao, A. T. Connie, M. H. Dastjerdi, X. H. Kong, Q. Wang, M. Djavid, S. Sadaf, X. D. Liu, I. Shih, H. Guo, and Z. Mi, "Aluminum nitride nanowire light emitting diodes: Breaking the fundamental bottleneck of deep ultraviolet light sources," *Sci. Rep.,* vol. 5, 8332, 2015.

[34] A. L. Henneghien, G. Tourbot, B. Daudin, O. Lartigue, Y. Désières, and J. M. Gérard, "Optical anisotropy and light extraction efficiency of MBE grown GaN nanowires epilayers," *Opt. Express,* vol. 19, pp. 527-539, 2011.

[35] Z. Mi, S. Zhao, S. Y. Woo, M. Bugnet, M. Djavid, X. Liu, J. Kang, X. Kong, W. Ji, H. Guo, Z. Liu, and G. A. Botton, "Molecular beam epitaxial growth and characterization of Al(Ga)N nanowire deep ultraviolet light emitting diodes and lasers," *J. Phys. D: Appl. Phys.,* vol. 49, p. 364006, 2016.

[36] S. Zhao, M. Djavid, and Z. Mi, "Surface Emitting, High Efficiency Near-Vacuum Ultraviolet Light Source with Aluminum Nitride Nanowires Monolithically Grown on Silicon," *Nano Lett.,* vol. 15, pp. 7006–7009, 2015.

[37] M. R. Hilton and P. D. Fleischauer, "Applications of solid lubricant films in spacecraft," *Surf. Coat. Technol.,* vol. 54, pp. 435-441, 1992.

[38] S. R. Cohen, L. Rapoport, E. A. Ponomarev, H. Cohen, T. Tsirlina, R. Tenne, and C. Lévy-Clément, "The tribological behavior of type II textured MX_2 (M= Mo, W; X= S, Se) films," *Thin Solid Films,* vol. 324, pp. 190-197, 1998.

[39] F. Xia, H. Wang, D. Xiao, M. Dubey, and A. Ramasubramaniam, "Two-dimensional material nanophotonics," *Nat. Photonics,* vol. 8, pp. 899-907, 2014.

[40] B. Radisavljevic1, A. Radenovic, J. Brivio1, V. Giacometti, and A. Kis, "Single-layer MoS_2 transistors," *Nat. Nanotechnol.,* vol. 6, pp. 147-150, 2011.

[41] Q. H. Wang, K. Kalantar-Zadeh, A. Kis, J. N. Coleman, and M. S. Strano, "Electronics and optoelectronics of two-dimensional transition metal dichalcogenides," *Nat. Nanotechnol.,* vol. 7, p. 699, 2012.

[42] A. B. Kaul, "Two-dimensional layered materials: Structure, properties, and prospects for device applications," *J. Mater. Res.,* vol. 29, pp. 348-361, 2014.

[43] K. F. Mak, C. Lee, J. Hone, J. Shan, and T. F. Heinz, "Atomically thin MoS_2: A new direct-gap semiconductor," *Phys. Rev. Lett.,* vol. 105, 136805, 2010.

[44] A. Splendiani, L. Sun, Y. Zhang, T. Li, J. Kim, C-Y Chim, G. Galli, and F. Wang, "Emerging photoluminescence in monolayer MoS_2," *Nano Lett.,* vol. 10, pp. 1271-1275, 2010.

[45] A. Kuc, N. Zibouche, and T. Heine, "Influence of quantum confinement on the electronic structure of the transition metal sulfide TS_2," *Phys. Rev. B,* vol. 83, p. 245213, 2011.

[46] R. Roldán, J. A. Silva-Guillén, M. P. López-Sancho, F. Guinea, E. Cappelluti, and P. Ordejón, "Electronic properties of single-layer and multilayer transition metal dichalcogenides MX_2 (M= Mo, W and X= S, Se)," *Annalen der Physik,* vol. 526, pp. 347-357, 2014.

[47] Z. M. Wang, "MoS_2 Materials, Physics, and Devices," *Lecture Notes in Nanoscale Science and Technology,* vol. 21, 2014.

[48] A. Ramasubramaniam, "Large excitonic effects in monolayers of molybdenum and tungsten dichalcogenides," *Phys. Rev. B,* vol. 86, p. 115409, 2012.

[49] Z. Y. Zhu, Y. C. Cheng, and U. Schwingenschlögl, "Giant spin-orbit-induced spin splitting in two-dimensional transition-metal dichalcogenide semiconductors," *Phys. Rev. B,* vol. 84, 153402, 2011.

[50] A. Chernikov, T. C. Berkelbach, H. M. Hill, A. Rigosi, Y. Li, O. B. Aslan, D. R. Reichman, M. S. Hybertsen, and T. F. Heinz, "Exciton binding energy and nonhydrogenic Rydberg series in monolayer WS_2," *Phys. Rev. Lett.,* vol. 113, p. 076802, 2014.

[51] T. Cheiwchanchamnangij and W. R. Lambrecht, "Quasiparticle band structure calculation of monolayer, bilayer, and bulk MoS_2," *Phys. Rev. B,* vol. 85, p. 205302, 2012.

[52] F. Hüser, T. Olsen, and K. S. Thygesen, "How dielectric screening in two-dimensional crystals affects the convergence of excited-state calculations: Monolayer MoS_2," *Phys. Rev. B,* vol. 88, p. 245309, 2013.

[53] H. Shi, H. Pan, Y.-W. Zhang, and B. I. Yakobson, "Quasiparticle band structures and optical properties of strained monolayer MoS_2 and WS_2," *Phys. Rev. B,* vol. 87, p. 155304, 2013.

[54] K. F. Mak, K. He, C. Lee, G. H. Lee, J. Hone, T. F. Heinz, and J. Shan, "Tightly bound trions in monolayer MoS_2," *Nat. Mater.,* vol. 12, pp. 207-211, 2013.

[55] Y. Li, A. Chernikov, X. Zhang, A. Rigosi, H. M. Hill, A. M. van der Zande, D. A. Chenet, E-M. Shih, J. Hone, and T. F. Heinz., "Measurement of the optical dielectric function of monolayer transition-metal dichalcogenides: MoS_2, $MoSe_2$, WS_2, and WSe_2," *Phys. Rev. B,* vol. 90, p. 205422, 2014.

[56] H. P. Komsa and A. V. Krasheninnikov, "Effects of confinement and environment on the electronic structure and exciton binding energy of MoS_2 from first principles," *Phys. Rev. B,* vol. 86, 241201, 2012.

[57] T. C. Berkelbach, M. S. Hybertsen, and D. R. Reichman, "Theory of neutral and charged excitons in monolayer transition metal dichalcogenides," *Phys. Rev. B,* vol. 88, p. 045318, 2013.

[58] D. Y. Qiu, H. Felipe, and S. G. Louie, "Optical spectrum of MoS_2: many-body effects and diversity of exciton states," *Phys. Rev. Lett.,* vol. 111, p. 216805, 2013.

[59] K. He, N. Kumar, L. Zhao, Z. Wang, K. F. Mak, H. Zhao, and J. Shan, "Tightly bound excitons in monolayer WSe_2," *Phys. Rev. Lett.,* vol. 113, 026803, 2014.

[60] Z. Ye, T. Cao, K. O'Brien, H. Zhu, X. Yin, Y. Wang, S. G. Louie, and X. Zhang, "Probing excitonic dark states in single-layer tungsten disulphide," *Nature,* vol. 513, p. 214, 2014.

[61] M. M. Ugeda, A. J. Bradley, S-F. Shi, F. H. da Jornada, Y. Zhang, D. Y. Qiu, W. Ruan, S-K. Mo, Z. Hussain, Z-X. Shen, F. Wang, S. G. Louie, and M. F. Crommie, "Giant bandgap renormalization and excitonic effects in a monolayer transition metal dichalcogenide semiconductor," *Nat. Mater.,* vol. 13, pp. 1091-1095, 2014.

[62] F. Withers, O. Del Pozo-Zamudio, A. Mishchenko, A. P. Rooney, A. Gholinia, K.Watanabe, T. Taniguchi, S. J. Haigh, A. K. Geim, A. I. Tartakovskii, and K. S. Novoselov, "Light-emitting diodes by band-structure engineering in van der Waals heterostructures," *Nat. Mater.,* vol. 14, pp. 301-306, 2015.

[63] L. Britnell, R. M. Ribeiro, A. Eckmann, R. Jalil, B. D. Belle, A. Mishchenko, Y.-]. Kim, R. V. Gorbachev, T. Georgiou, S. V. Morozov, A. N. Grigorenko, A. K. Geim, C. Casiraghi, A. H. Castro Neto, K. S. Novoselov, "Strong light-matter interactions in heterostructures of atomically thin films," *Science,* vol. 340, pp. 1311-1314, 2013.

[64] Q. Yue, J. Kang, Z. Shao, X. Zhang, S. Chang, G. Wang, S. Qin, and J. Li, "Mechanical and electronic properties of monolayer MoS_2 under elastic strain," *Phys. Lett. A,* vol. 376, pp. 1166-1170, 2012.

[65] A. Castellanos-Gomez, M. Poot, G. A. Steele, H. S. Van Der Zant, N. Agraït, and G. Rubio-Bollinger, "Elastic properties of freely suspended MoS_2 nanosheets," *Adv. Mater.,* vol. 24, pp. 772-775, 2012.

[66] S. Bertolazzi, J. Brivio, and A. Kis, "Stretching and breaking of ultrathin MoS_2," *ACS Nano,* vol. 5, pp. 9703-9709, 2011.

[67] I. Omae, "Recent developments in carbon dioxide utilization for the production of organic chemicals," *Coord. Chem. Rev.,* vol. 256, pp. 1384-1405, 2012.

[68] J. Blunden, D. S. Arndt, and G. Hartfield, "State of the Climate in 2017," *Bull. Amer. Meteor. Soc,* vol. 99, 2018.

[69] M. I. Hoffert, K. Caldeira, A. K. Jain, E. F. Haites, L. D. Danny Harveyk, S. D. Potter, M. E. Schlesinger, S. H. Schneider, R. G.Watts, T. M. L. Wigley, and D. J. Wuebbles, "Energy implications of future stabilization of atmospheric CO_2 content," *Nature,* vol. 395, p. 881, 1998.

[70] N. S. Lewis and D. G. Nocera, "Powering the planet: Chemical challenges in solar energy utilization," *Proc. Natl. Acad. Sci.,* vol. 103, pp. 15729-15735, 2006.

[71] R. Perez and M. Perez, "A fundamental look at supply side energy reserves for the planet," *Int. Energy Agency SHC Program. Sol. Updat,* vol. 62, pp. 4-6, 2015.

[72] K. Rajeshwar, R. D. McConnell, and S. Licht, *Solar hydrogen generation: toward a renewable energy future*, New York, 2008.

[73] C. Grimes, O. Varghese, and S. Ranjan, *Light, water, hydrogen: the solar generation of hydrogen by water photoelectrolysis*, Springer Science & Business Media, 2007.

[74] J. A. Turner, "A realizable renewable energy future," *Science,* vol. 285, pp. 687-689, 1999.

[75] A. Fujishima and K. Honda, "Electrochemical photolysis of water at a semiconductor electrode," *Nature,* vol. 238, p. 37, 1972.

[76] S. Chen, T. Takata, and K. Domen, "Particulate photocatalysts for overall water splitting," *Nat. Rev. Mater.,* vol. 2, p. 17050, 2017.

[77] L. Yuan, C. Han, M.-Q. Yang, and Y.-J. Xu, "Photocatalytic water splitting for solar hydrogen generation: fundamentals and recent advancements," *Int. Rev. Phys. Chem.,* vol. 35, pp. 1-36, 2016.

[78] J. R. Bolton, "Solar photoproduction of hydrogen: a review," *Sol. Energy,* vol. 57, pp. 37-50, 1996.

[79] Y. Tachibana, L. Vayssieres, and J. R. Durrant, "Artificial photosynthesis for solar water-splitting," *Nat. Photonics,* vol. 6, p. 511, 2012.

[80] Z. Wang, C. Li, and K. Domen, "Recent developments in heterogeneous photocatalysts for solar-driven overall water splitting," *Chem. Soc. Rev.,* vol. 48, pp. 2109-2125, 2019.

[81] J. Yang, D. Wang, H. Han, and C. Li, "Roles of cocatalysts in photocatalysis and photoelectrocatalysis," *Acc. Chem. Res.,* vol. 46, pp. 1900-1909, 2013.

[82] A. Kudo and Y. Miseki, "Heterogeneous photocatalyst materials for water splitting," *Chem. Soc. Rev.,* vol. 38, pp. 253-278, 2009.

[83] X. Chen, S. Shen, L. Guo, and S. S. Mao, "Semiconductor-based photocatalytic hydrogen generation," *Chem. Rev.,* vol. 110, pp. 6503-6570, 2010.

[84] K. Maeda and K. Domen, "Photocatalytic water splitting: recent progress and future challenges," *J. Phys. Chem. Lett.,* vol. 1, pp. 2655-2661, 2010.

[85] R. M. Navarro Yerga, M. C. Alvarez Galvan, F. Del Valle, J. A. Villoria de la Mano, and J. L. Fierro, "Water splitting on semiconductor catalysts under visible-light irradiation," *ChemSusChem,* vol. 2, pp. 471-485, 2009.

[86] Y. Wang, H. Suzuki, J. Xie, O. Tomita, D. J. Martin, M. Higashi, D. Kong, R. Abe, and J. Tang, "Mimicking natural photosynthesis: solar to renewable H_2 fuel synthesis by Z-scheme water splitting systems," *Chem. Rev.,* vol. 118, pp. 5201-5241, 2018.

[87] J. Wu, "When group-III nitrides go infrared: New properties and perspectives," *J. Appl. Phys.,* vol. 106, 011101, 2009.

[88] W. Luo, B. Liu, Z. Li, Z. Xie, D. Chen, Z. Zou, and R. Zhang, "Stable response to visible light of InGaN photoelectrodes," *Appl. Phys. Lett.,* vol. 92, p. 262110, 2008.

[89] P. G. Moses and C. G. Van de Walle, "Band bowing and band alignment in InGaN alloys," *Appl. Phys. Lett.,* vol. 96, p. 021908, 2010.

[90] F. E. Osterloh, "Inorganic nanostructures for photoelectrochemical and photocatalytic water splitting," *Chem. Soc. Rev.,* vol. 42, pp. 2294-2320, 2013.

[91] N. Wu, J. Wang, D. N. Tafen, H. Wang, J.-G. Zheng, J. P. Lewis, X. Liu, S. S. Leonard, and A. Manivannan, "Shape-enhanced photocatalytic activity of single-crystalline anatase TiO_2 (101) nanobelts," *J. Am. Chem. Soc.,* vol. 132, pp. 6679-6685, 2010.

[92] M. Kibria and Z. Mi, "Artificial photosynthesis using metal/nonmetal-nitride semiconductors: current status, prospects, and challenges," *J. Mater. Chem. A,* vol. 4, pp. 2801-2820, 2016.

[93] I. M. Tiginyanu, V. V. Ursaki, V. V. Zalamai, S. Langa, S. Hubbard, D. Pavlidis, and H. Foll, "Luminescence of GaN nanocolumns obtained by photon-assisted anodic etching," *Appl. Phys. Lett.,* vol. 83, pp. 1551-1553, 2003.

[94] C.-Y. Wang, L.-Y. Chen, C.-P. Chen, Y.-W. Cheng, M.-Y. Ke, M.-Y. Hsieh, H.-M. Wu, L.-H. Peng, and J. Huang, "GaN nanorod light emitting diode arrays with a nearly constant electroluminescent peak wavelength," *Opt. Express,* vol. 16, pp. 10549-10556, 2008.

[95] G. T. Wang, Q. Li, J. J. Wierer, D. D. Koleske, and J. J. Figiel, "Top–down fabrication and characterization of axial and radial III-nitride nanowire LEDs," *Phys. Status Solidi A,* vol. 211, pp. 748-751, 2014.

[96] J. Zhu, L. Wang, S. Zhang, H. Wang, D. Zhao, J. Zhu, Z. Liu, D. Jiang, and H. Yang, "The fabrication of GaN-based nanopillar light-emitting diodes," *J. Appl. Phys.,* vol. 108, p. 074302, 2010.

[97] T. Tang, S. Han, W. Jin, X. Liu, C. Li, D. Zhang, C. Zhou, B. Chen, J. Han, and M. Meyyapan, "Synthesis and characterization of single-crystal indium nitride nanowires," *J. Mater. Res.,* vol. 19, pp. 423-426, 2004.

[98] H. Y. Peng, X. T. Zhou, N. Wang, Y. F. Zheng, L. S. Liao, W. S. Shi, C. S. Lee, and S. T. Lee, "Bulk-quantity GaN nanowires synthesized from hot filament chemical vapor deposition," *Chem. Phys. Lett.,* vol. 327, pp. 263-270, 2000.

[99] C. K. Chao, J.-I. Chyi, C. N. Hsiao, C. C. Kei, S. Y. Kuo, H.-S. Chang, and T. M. Hsu, "Catalyst-free growth of indium nitride nanorods by chemical-beam epitaxy," *Appl. Phys. Lett.,* vol. 88, p. 233111, 2006.

[100] Y.-L. Chang, F. Li, A. Fatehi, and Z. Mi, "Molecular beam epitaxial growth and characterization of non-tapered InN nanowires on Si (111)," *Nanotechnology,* vol. 20, p. 345203, 2009.

[101] R. Debnath, R. Meijers, T. Richter, T. Stoica, R. Calarco, and H. Lüth, "Mechanism of molecular beam epitaxy growth of GaN nanowires on Si (111)," *Appl. Phys. Lett.,* vol. 90, p. 123117, 2007.

[102] V. Gottschalch, G. Wagner, J. Bauer, H. Paetzelt, and M. Shirnow, "VLS growth of GaN nanowires on various substrates," *J. Cryst. Growth,* vol. 310, pp. 5123-5128, 2008.

[103] R. Wagner and W. Ellis, "Vapor-liquid-solid mechanism of single crystal growth," *Appl. Phys. Lett.,* vol. 4, pp. 89-90, 1964.

[104] R. Wagner and A. P. Levitt, "Whisker technology," *by AP Levitt, Wiley, New York,* pp. 47-119, 1970.

[105] B. A. Wacaser, K. A. Dick, J. Johansson, M. T. Borgström, K. Deppert, and L. Samuelson, "Preferential interface nucleation: an expansion of the VLS growth mechanism for nanowires," *Adv. Mater.,* vol. 21, pp. 153-165, 2009.

[106] E. Stern, G. Cheng, E. Cimpoiasu, R. Klie, S. Guthrie, J. Klemic, I. Kretzschmar, E. Steinlauf, D. Turner-Evans, E. Broomfield, J. Hyland, R. Koudelka, T. Boone, M. Young, A. Sanders, R. Munden, T. Lee, D. Routenberg, and M. A. Reed, "Electrical characterization of single GaN nanowires," *Nanotechnology,* vol. 16, pp. 2941-2953, 2005.

[107] S. Kang, B. Kang, and D. Yoon, "Growth and properties of vertically well-aligned GaN nanowires by thermal chemical vapor deposition process," *Mater. Lett.,* vol. 65, pp. 763-765, 2011.

[108] J. Liu, Z. Cai, and G. Koley, "Charge transport and trapping in InN nanowires investigated by scanning probe microscopy," *J. Appl. Phys.,* vol. 106, p. 124907, 2009.

[109] C. Chèze, L. Geelhaar, O. Brandt, W. M. Weber, H. Riechert, S. Münch, R. Rothemund, S. Reitzenstein, A. Forchel, T. Kehagias, P. Komninou, G. P. Dimitrakopulos, and T. Karakostas, "Direct comparison of catalyst-free and catalyst-induced GaN nanowires," *Nano Res.,* vol. 3, pp. 528-536, 2010.

[110] J. Ristić, E. Calleja, S. Fernández-Garrido, L. Cerutti, A. Trampert, U. Jahn, and K. H. Ploog, "On the mechanisms of spontaneous growth of III-nitride nanocolumns by plasma-assisted molecular beam epitaxy," *J. Cryst. Growth,* vol. 310, pp. 4035-4045, 2008.

[111] A. Vajpeyi, A. O. Ajagunna, G. Tsiakatouras, A. Adikimenakis, E. Iliopoulos, K. Tsagaraki, M. Androulidaki, and A. Georgakilas, "Spontaneous growth of III-nitride nanowires on Si by molecular beam epitaxy," *Microelectron. Eng.,* vol. 86, pp. 812-815, 2009.

[112] T. Stoica, R. Meijers, R. Calarco, T. Richter, and H. Lüth, "MBE growth optimization of InN nanowires," *J. Cryst. Growth,* vol. 290, pp. 241-247, 2006.

[113] V. Consonni, M. Knelangen, L. Geelhaar, A. Trampert, and H. Riechert, "Nucleation mechanisms of epitaxial GaN nanowires: Origin of their self-induced formation and initial radius," *Phys. Rev. B,* vol. 81, p. 085310, 2010.

[114] V. Consonni, M. Hanke, M. Knelangen, L. Geelhaar, A. Trampert, and H. Riechert, "Nucleation mechanisms of self-induced GaN nanowires grown on an amorphous interlayer," *Phys. Rev. B,* vol. 83, p. 035310, 2011.

[115] K. A. Bertness, A. Roshko, L. Mansfield, T. E. Harvey, and N. A. Sanford, "Mechanism for spontaneous growth of GaN nanowires with molecular beam epitaxy," *J. Cryst. Growth,* vol. 310, pp. 3154-3158, 2008.

[116] Q. Wang, X. Liu, M. G. Kibria, S. Zhao, H. P. T. Nguyen, K. H. Li, Z. Mi, T. Gonzalezb, and M. P. Andrews, "p-Type dopant incorporation and surface charge properties of catalyst-free GaN nanowires revealed by micro-Raman scattering and X-ray photoelectron spectroscopy," *Nanoscale,* vol. 6, pp. 9970-9976, 2014.

[117] S. D. Hersee, X. Sun, and X. Wang, "The controlled growth of GaN nanowires," *Nano Lett.,* vol. 6, pp. 1808-1811, 2006.

[118] K. A. Bertness, Aric W. Sanders, D. M. Rourke, T. E. Harvey, A. Roshko, J. B. Schlager, and N. A. Sanford, "Controlled nucleation of GaN nanowires grown with molecular beam epitaxy," *Adv. Funct. Mater.,* vol. 20, pp. 2911-2915, 2010.

[119] T. Schumann, T. Gotschke, F. Limbach, T. Stoica, and R. Calarco, "Selective-area catalyst-free MBE growth of GaN nanowires using a patterned oxide layer," *Nanotechnology,* vol. 22, p. 095603, 2011.

[120] H. Sekiguchi, K. Kishino, and A. Kikuchi, "Ti-mask selective-area growth of GaN by RF-plasma-assisted molecular-beam epitaxy for fabricating regularly arranged InGaN/GaN nanocolumns," *Appl. Phys. Express,* vol. 1, p. 124002, 2008.

[121] K. Kishino, H. Sekiguchi, and A. Kikuchi, "Improved Ti-mask selective-area growth (SAG) by rf-plasma-assisted molecular beam epitaxy demonstrating extremely uniform GaN nanocolumn arrays," *J. Cryst. Growth,* vol. 311, pp. 2063-2068, 2009.

[122] A. Bengoechea-Encabo, F.Barbagini, S. Fernandez-Garrido, J. Grandal, J. Ristic, M. A. Sanchez-Garcia, E. Calleja, U. Jahn, E. Luna, and A. Trampert, "Understanding the selective area growth of GaN nanocolumns by MBE using Ti nanomasks," *J. Cryst. Growth,* vol. 325, pp. 89-92, 2011.

[123] S. F. Li, S. Fuendling, X. Wang, S. Merzsch, M. A. M. Al-Suleiman, J. D. Wei, H.-H. Wehmann, A. Waag, W. Bergbauer, and M. Strassburg, "Polarity and its influence on growth mechanism during MOVPE growth of GaN sub-micrometer rods," *Cryst. Growth Des.,* vol. 11, pp. 1573-1577, 2011.

[124] Z. Gačević, D. G. Sanchez, and E. Calleja, "Formation mechanisms of GaN nanowires grown by selective area growth homoepitaxy," *Nano Lett.,* vol. 15, pp. 1117-1121, 2015.

[125] V. A. Shchukin and D. Bimberg, "Spontaneous ordering of nanostructures on crystal surfaces," *Rev. Mod. Phys.,* vol. 71, p. 1125, 1999.

[126] J. Li, Z. Y. Fan, R. Dahal, M. L. Nakarmi, J. Y. Lin, and H. X. Jiang, "200 nm deep ultraviolet photodetectors based on AlN," *Appl. Phys. Lett.,* vol. 89, p. 213510, 2006.

[127] H. Sekiguchi, K. Kishino, and A. Kikuchi, "GaN/AlGaN nanocolumn ultraviolet light-emitting diodes grown on n-(111) Si by RF-plasma-assisted molecular beam epitaxy," *Electron. Lett.,* vol. 44, pp. 151-152, 2008.

[128] T. Nishida, H. Saito, and N. Kobayashi, "Efficient and high-power AlGaN-based ultraviolet light-emitting diode grown on bulk GaN," *Appl. Phys. Lett.,* vol. 79, pp. 711-712, 2001.

[129] M. A. Khan, M. Shatalov, H. P. Maruska, H. M. Wang, and E. Kuokstis, "III-nitride UV devices," *Jpn. J. Appl. Phys.,* vol. 44, pp. 7191-7206, 2005.

[130] M. H. Crawford, A. A. Allerman, A. M. Armstrong, M. L. Smith, and K. C. Cross, "Laser diodes with 353nm wavelength enabled by reduced-dislocation-density AlGaN templates," *Appl. Phys. Express,* vol. 8, 112702, 2015.

[131] Y. P. Gong, K. Xing, and T. Wang, "Influence of high temperature AlN buffer on optical gain in AlGaN/AlGaN multiple quantum well structures," *Appl. Phys. Lett.,* vol. 99, p. 171912, 2011.

[132] M. Nakarmi, N. Nepal, C. Ugolini, T. Altahtamouni, J. Lin, and H. Jiang, "Correlation between optical and electrical properties of Mg-doped AlN epilayers," *Appl. Phys. Lett.,* vol. 89, p. 152120, 2006.

[133] C. Stampfl and C. G. Van de Walle, "Theoretical investigation of native defects, impurities, and complexes in aluminum nitride," *Phys. Rev. B,* vol. 65, pp. 1552121-15521210, 2002.

[134] C. G. Van De Walle and J. Neugebauer, "First-principles calculations for defects and impurities: Applications to III-nitrides," *J. Appl. Phys.,* vol. 95, pp. 3851-3879, 2004.

[135] J. Simon, V. Protasenko, C. Lian, H. Xing, and D. Jena, "Polarization-induced hole doping in wide-band-gap uniaxial semiconductor heterostructures," *Science,* vol. 327, pp. 60-64, 2010.

[136] A. T. M. G. Sarwar, B. J. May, J. I. Deitz, T. J. Grassman, D. W. McComb, and R. C. Myers, "Tunnel junction enhanced nanowire ultraviolet light emitting diodes," *Appl. Phys. Lett.,* vol. 107, p. 101103, 2015.

[137] G. Kipshidze, V. Kuryatkov, B. Borisov, Yu. Kudryavtsev, R. Asomoza, S. Nikishin, and H. Temkin, "Mg and O codoping in p-type GaN and $Al_xGa_{1-x}N$ ($0<x<0.08$)," *Appl. Phys. Lett.,* vol. 80, pp. 2910-2912, 2002.

[138] H. Wu, R. Zheng, W. Liu, S. Meng, and J. Huang, "C and Si codoping method for p -type AlN," *J. Appl. Phys.,* vol. 108, 053715, 2010.

[139] V. N. Jmerik, A. M. Mizerov, T. V. Shubina, A. A. Toropov, K. G. Belyaev, A. A. Sitnikova, M. A. Yagovkina, P. S. Kop'ev, E. V. Lutsenko, A. V. Danilchyk, N. V. Rzheutskii, G. P. Yablonskii, B. Monemar, and S. V. Ivanov, "Optically pumped lasing at 300.4nm in AlGaN MQW structures

grown by plasma-assisted molecular beam epitaxy on c-Al_2O_3," *Phys. Status Solidi A,* vol. 207, pp. 1313-1317, 2010.

[140] T. Wunderer, C. L. Chua, J. E. Northrup, Z. Yang, N. M. Johnson, M. Kneissl, G. A. Garrett, H. Shen, M. Wraback, B. Moody, H. S. Craft, R. Schlesser, R. F. Dalmau, and Z. Sitar, "Optically pumped UV lasers grown on bulk AlN substrates," *Phys. Status Solidi C,* vol. 9, pp. 822-825, 2012.

[141] T. Takano, Y. Narita, A. Horiuchi, and H. Kawanishi, "Room-temperature deep-ultraviolet lasing at 241.5 nm of AlGaN multiple-quantum-well laser," *Appl. Phys. Lett.,* vol. 84, pp. 3567-3569, 2004.

[142] J. Xie, S. Mita, Z. Bryan, W. Guo, L. Hussey, B. Moody, R. Schlesser, R. Kirste, M. Gerhold, R. Collazo, and Z. Sitar, "Lasing and longitudinal cavity modes in photo-pumped deep ultraviolet AlGaN heterostructures," *Appl. Phys. Lett.,* vol. 102, p. 171102, 2013.

[143] M. Martens, F. Mehnke, C. Kuhn, C. Reich, V. Kueller, A. Knauer, C. Netzel, C. Hartmann, J. Wollweber, J. Rass, T. Wernicke, M. Bickermann, M. Weyers, and M. Kneissl, "Performance characteristics of UV-C AlGaN-based lasers grown on sapphire and bulk AlN substrates," *IEEE Photonics Technol. Lett.,* vol. 26, pp. 342-345, 2014.

[144] S. Zhao, S. Fathololoumi, K. H. Bevan, D. P. Liu, M. G. Kibria, Q. Li, G. T. Wang, H. Guo, and Z. Mi, "Tuning the surface charge properties of epitaxial InN nanowires," *Nano Lett.,* vol. 12, pp. 2877-82, 2012.

[145] S. Zhao, A. T. Connie, M. H. Dastjerdi, X. H. Kong, Q. Wang, M. Djavid, S. Sadaf, X. D. Liu, I. Shih, H. Guo, and Z. Mi, "Aluminum nitride nanowire light emitting diodes: Breaking the fundamental bottleneck of deep ultraviolet light sources," *Sci. Rep.,* vol. 5, 8332, 2015.

[146] S. Zhao, X. Liu, S. Y. Woo, J. Kang, G. A. Botton, and Z. Mi, "An electrically injected AlGaN nanowire laser operating in the ultraviolet-C band," *Appl. Phys. Lett.,* vol. 107, p. 043101, 2015.

[147] Y.-B. Tang, X.-H. Bo, J. Xu, Y.-L. Cao, Z.-H. Chen, H.-S. Song, C.-P. Liu, T.-F. Hung, W.-J. Zhang, H.-M. Cheng, I. Bello, S.-T. Lee, and C.-S. Lee, "Tunable p-type conductivity and transport properties of AlN nanowires via Mg doping," *ACS Nano,* vol. 5, pp. 3591-3598, 2011.

[148] A. T. Connie, S. Zhao, S. Md. Sadaf, I. Shih, Z. Mi, X. Du, J. Lin, and H. Jiang, "Optical and electrical properties of Mg-doped AlN nanowires grown by molecular beam epitaxy," *Appl. Phys. Lett.,* vol. 106, p. 213105, 2015.

[149] Q. Wang, S. Zhao, A. T. Connie, I. Shih, Z. Mi, T. Gonzalez, M. P. Andrews, X. Z. Du, J. Y. Lin, and H. X. Jiang, "Optical properties of strain-free AlN nanowires grown by molecular beam epitaxy on Si substrates," *Appl. Phys. Lett.,* vol. 104, p. 223107, 2014.

[150] K. Kumakura, T. Makimoto, and N. Kobayashi, "Mg-acceptor activation mechanism and transport characteristics in p-type InGaN grown by metalorganic vapor phase epitaxy," *J. Appl. Phys.,* vol. 93, pp. 3370-3375, 2003.

[151] T. Kinoshita, T. Obata, H. Yanagi, and S. I. Inoue, "High p-type conduction in high-Al content Mg-doped AlGaN," *Appl. Phys. Lett.,* vol. 102, p. 012105, 2013.

[152] Z. Zhong, F. Qian, D. Wang, and C. M. Lieber, "Synthesis of p-type gallium nitride nanowires for electronic and photonic nanodevices," *Nano Lett.,* vol. 3, pp. 343-346, 2003.

[153] D. Wang, Q. Wang, A. Javey, R. Tu, H. Dai, H. Kim, P. C. McIntyre, T. Krishnamohan, and K. C. Saraswat, "Germanium nanowire field-effect transistors with SiO2 and high-κ HfO2 gate dielectrics," *Appl. Phys. Lett.,* vol. 83, pp. 2432-2434, 2003.

[154] J. Jie, W. Zhang, K. Peng, G. Yuan, C. S. Lee, and S. T. Lee, "Surface-dominated transport properties of silicon nanowires," *Adv. Funct. Mater.,* vol. 18, pp. 3251-3257, 2008.

[155] B. Sapoval and C. Hermann, *Physics of Semiconductors,* Springer, New York, 1995.

[156] C. S. Hung and J. R. Gliessman, "Resistivity and Hall Effect of Germanium at Low Temperatures," *Phys. Rev.,* vol. 96, pp. 1226-1236, 1954.

[157] R. J. Molnar, T. Lei, and T. D. Moustakas, "Electron transport mechanism in gallium nitride," *Appl. Phys. Lett.,* vol. 62, pp. 72-74, 1993.

[158] W. Geerts, J. D. Mackenzie, C. R. Abernathy, S. J. Pearton, and T. Schmiedel, "Electrical transport in p-GaN, n-InN and n-InGaN," *Solid State Electron.,* vol. 39, pp. 1289-1294, 1996.

[159] G. L. Pearson and J. Bardeen, "Electrical properties of pure silicon and silicon alloys containing boron and phosphorus," *Phys. Rev.,* vol. 75, pp. 865-883, 1949.

[160] A. Motayed, A. V. Davydov, S. N. Mohammad, and J. Melngailis, "Experimental investigation of electron transport properties of gallium nitride nanowires," *J. Appl. Phys.,* vol. 104, p. 024302, 2008.

[161] S. Zhao, B. H. Le, D. P. Liu, X. D. Liu, M. G. Kibria, T. Szkopek, H. Guo, and Z. Mi, "P-type InN nanowires," *Nano Lett.,* vol. 13, pp. 5509-5513, 2013.

[162] M. Bernardi, M. Palummo, and J. C. Grossman, "Extraordinary sunlight absorption and one nanometer thick photovoltaics using two-dimensional monolayer materials," *Nano Lett.,* vol. 13, pp. 3664-3670, 2013.

[163] W. Bao, X. Cai, D. Kim, K. Sridhara, and M. S. Fuhrer, "High mobility ambipolar MoS_2 field-effect transistors: Substrate and dielectric effects," *Appl. Phys. Lett.,* vol. 102, p. 042104, 2013.

[164] B. Radisavljevic and A. Kis, "Mobility engineering and a metal–insulator transition in monolayer MoS_2," *Nat. Mater.,* vol. 12, p. 815, 2013.

[165] T. Korn, S. Heydrich, M. Hirmer, J. Schmutzler, and C. Schuller, "Low-temperature photocarrier dynamics in monolayer MoS_2," *Appl. Phys. Lett.,* vol. 99, p. 102109, 2011.

[166] S. Tongay, J. Zhou, C. Ataca, K. Lo, T. S. Matthews, J. Li, J. C. Grossman, and J. Wu, "Thermally driven crossover from indirect toward direct bandgap in 2D semiconductors: $MoSe_2$ versus MoS_2," *Nano Lett.,* vol. 12, pp. 5576-5580, 2012.

[167] Y. P. Varshni, "Temperature dependence of the energy gap in semiconductors," *Physica,* vol. 34, pp. 149-154, 1967.

[168] O. Salehzadeh, N. H. Tran, X. Liu, I. Shih, and Z. Mi, "Exciton kinetics, quantum efficiency, and efficiency droop of monolayer MoS_2 light-emitting devices," *Nano Lett.,* vol. 14, pp. 4125-4130, 2014.

[169] Q. Dai, M. F. Schubert, M. H. Kim, J. K. Kim, E. F. Schubert, D. D. Koleske, M. H. Crawford, S. R. Lee, A. J. Fischer, G. Thaler, and M. A. Banas, "Internal quantum efficiency and nonradiative recombination coefficient of GaInN/GaN multiple quantum wells with different dislocation densities," *Appl. Phys. Lett.,* vol. 94, p. 111109, 2009.

[170] A. Castellanos-Gomez, N. Agraït, and G. Rubio-Bollinger, "Optical identification of atomically thin dichalcogenide crystals," *Appl. Phys. Lett.,* vol. 96, p. 213116, 2010.

[171] H. Shi, R. Yan, S. Bertolazzi, J. Brivio, B. Gao, A. Kis, D. Jena, H. G. Xing, and L. Huang, "Exciton dynamics in suspended monolayer and few-layer MoS_2 2D crystals," *ACS Nano,* vol. 7, pp. 1072-1080, 2013.

[172] P. T. Landsberg, *Recombination in semiconductors*, Cambridge University Press, 1991.

[173] Y. Varshni, "Band-to-band radiative recombination in groups IV, VI, and III-V semiconductors (I)," *Phys. Status Solidi B,* vol. 19, pp. 459-514, 1967.

[174] R. N. Hall, "Recombination processes in semiconductors," *Proc. IEE,* vol. 106, pp. 923-931, 1959.

[175] R. Olshansky, C. Su, J. Manning, and W. Powazinik, "Measurement of radiative and nonradiative recombination rates in InGaAsP and AlGaAs light sources," *IEEE J. Quantum Electron.,* vol. 20, pp. 838-854, 1984.

[176] Y. C. Shen, G. O. Mueller, S. Watanabe, N. F. Gardner, A. Munkholm, and M. R. Krames, "Auger recombination in InGaN measured by photoluminescence," *Appl. Phys. Lett.,* vol. 91, p. 141101, 2007.

[177] R. Fehse, S. Tomic´, A. R. Adams, S. J. Sweeney, E. P. O'Reilly, A. Andreev, and H. Riechert, "A quantitative study of radiative, Auger, and defect related recombination processes in 1.3-μ GaInNAs-based quantum-well lasers," *IEEE J. Sel. Top. Quantum Electron.,* vol. 8, pp. 801-810, 2002.

[178] W. Zhao, R. M. Ribeiro, M. Toh, A. Carvalho, C. Kloc, A. H. Castro Neto, and G. Eda, "Origin of indirect optical transitions in few-layer MoS_2, WS_2, and WSe_2," *Nano Lett.,* vol. 13, pp. 5627-5634, 2013.

[179] O. Salehzadeh, M. Djavid, N. H. Tran, I. Shih, and Z. Mi, "Optically Pumped Two-Dimensional MoS_2 Lasers Operating at Room-Temperature," *Nano Lett.,* vol. 15, pp. 5302-5306, 2015.

[180] R. Dhall, M. R. Neupane, D. Wickramaratne, M. Mecklenburg, Z. Li, C. Moore, R. K. Lake, and S. Cronin, "Direct Bandgap Transition in Many-Layer MoS_2 by Plasma-Induced Layer Decoupling," *Adv. Mater.,* vol. 27, pp. 1573-1578, 2015.

[181] G. Mie, "Beiträge zur Optik trüber Medien, speziell kolloidaler Metallösungen," *Annalen der physik,* vol. 330, pp. 377-445, 1908.

[182] W.-H. Cheng, M. H. Richter, M. M. May, J. Ohlmann, D. Lackner, F. Dimroth, T. Hannappel, H. A. Atwater, and H.-J. Lewerenz, "Monolithic photoelectrochemical device for direct water splitting with 19% efficiency," *ACS Energy Lett.,* vol. 3, pp. 1795-1800, 2018.

[183] J. Jia, L. C. Seitz, J. D. Benck, Y. Huo, Y. Chen, J. W. Desmond Ng, T. Bilir, J. S. Harris, and T. F. Jaramillo, "Solar water splitting by photovoltaic-electrolysis with a solar-to-hydrogen efficiency over 30%," *Nat. Commun.,* vol. 7, p. 13237, 2016.

[184] J. L. Young, M. A. Steiner, H. Döscher, R. M. France, J. A. Turner, and T. G. Deutsch, "Direct solar-to-hydrogen conversion via inverted metamorphic multi-junction semiconductor architectures," *Nat. Energy,* vol. 2, p. 17028, 2017.

[185] T. J. Jacobsson, V. Fjällström, M. Sahlberg, M. Edoff, and T. Edvinsson, "A monolithic device for solar water splitting based on series interconnected thin film absorbers reaching over 10% solar-to-hydrogen efficiency," *Energy Environ. Sci.,* vol. 6, pp. 3676-3683, 2013.

[186] J. Luo, J.-H. Im, M. T. Mayer, M. Schreier, M. K. Nazeeruddin, N.-G. Park, S. D. Tilley, H. J. Fan, and M. Gratzel, "Water photolysis at 12.3% efficiency via perovskite photovoltaics and Earth-abundant catalysts," *Science,* vol. 345, pp. 1593-1596, 2014.

[187] P. Kohl and F. Ostermayer Jr, "Photoelectrochemical methods for III-V compound semiconductor device processing," *Annu. Rev. Mater. Sci.,* vol. 19, pp. 379-399, 1989.

[188] M. M. May, H.-J. Lewerenz, D. Lackner, F. Dimroth, and T. Hannappel, "Efficient direct solar-to-hydrogen conversion by in situ interface transformation of a tandem structure," *Nat. Commun.,* vol. 6, p. 8286, 2015.

[189] Q. Wang, T. Hisatomi, Q. Jia, H. Tokudome, M. Zhong, C. Wang, Z. Pan, T. Takata, M. Nakabayashi, N. Shibata, Y. Li, I. D. Sharp, A. Kudo, T. Yamada, and K. Domen, "Scalable water splitting on particulate photocatalyst sheets with a solar-to-hydrogen energy conversion efficiency exceeding 1%," *Nat. Mater.,* vol. 15, p. 611, 2016.

[190] M. Schröder, K. Kailasam, J. Borgmeyer, M. Neumann, A. Thomas, R. Schomacker, and M. Schwarze, "Hydrogen Evolution Reaction in a Large-Scale Reactor using a Carbon Nitride Photocatalyst under Natural Sunlight Irradiation," *Energy Technol.,* vol. 3, pp. 1014-1017, 2015.

[191] Q. Wang, T. Hisatomi, M. Katayama, T. Takata, T. Minegishi, A. Kudo, T. Yamada, and K. Domen, "Particulate photocatalyst sheets for Z-scheme water splitting: advantages over powder suspension and photoelectrochemical systems and future challenges," *Faraday Discuss.,* vol. 197, pp. 491-504, 2017.

[192] N. S. Lewis, "Developing a scalable artificial photosynthesis technology through nanomaterials by design," *Nat. Nanotechnol.,* vol. 11, p. 1010, 2016.

[193] O. Khaselev and J. A. Turner, "A Monolithic Photovoltaic-Photoelectrochemical Device for Hydrogen Production via Water Splitting," *Science,* vol. 280, p. 425, 1998.

[194] S. Bell, G. Will, and J. Bell, "Light intensity effects on photocatalytic water splitting with a titania catalyst," *Int. J. Hydrog. Energy,* vol. 38, pp. 6938-6947, 2013.

[195] M. G. Kibria, S. Zhao, F. A. Chowdhury, Q. Wang, H. P. T. Nguyen, M. L. Trudeau, H. Guo, and Z. Mi, "Tuning the surface Fermi level on p-type gallium nitride nanowires for efficient overall water splitting," *Nat. Commun.,* vol. 5, p. 3825, 2014.

[196] M. Kibria, F. A. Chowdhury, S. Zhao, B. AlOtaibi, M. L. Trudeau, H. Guo, and Z. Mi, "Visible light-driven efficient overall water splitting using p-type metal-nitride nanowire arrays," *Nat. Commun.,* vol. 6, p. 6797, 2015.

[197] B. AlOtaibi, H. Nguyen, S. Zhao, M. Kibria, S. Fan, and Z. Mi, "Highly stable photoelectrochemical water splitting and hydrogen generation using a double-band InGaN/GaN core/shell nanowire photoanode," *Nano Lett.,* vol. 13, pp. 4356-4361, 2013.

[198] M. G. Kibria, R. Qiao, W. Yang, I. Boukahil, X. Kong, F. A. Chowdhury, M. L. Trudeau, W. Ji, H. Guo, F. J. Himpsel, L. Vayssieres, and Z. Mi, "Atomic-Scale Origin of Long-Term Stability and High Performance of p-GaN Nanowire Arrays for Photocatalytic Overall Pure Water Splitting," *Adv. Mater.,* vol. 28, pp. 8388-8397, 2016.

[199] D. Doppalapudi, S. Basu, K. Ludwig Jr, and T. Moustakas, "Phase separation and ordering in InGaN alloys grown by molecular beam epitaxy," *J. Appl. Phys.,* vol. 84, pp. 1389-1395, 1998.

[200] X. Guan, F. A. Chowdhury, Y. Wang, N. Pant, S. Vanka, M. L. Trudeau, L. Guo, L. Vayssieres, and Z. Mi, "Making of An Industry-Friendly Artificial Photosynthesis Device," *ACS Energy Lett.,* vol. 3, pp. 2230-2231, 2018.

[201] Y. Goto, T. Hisatomi, Q. Wang, T. Higashi, K. Ishikiriyama, T. Maeda, Y. Sakata, S. Okunaka, H. Tokudome, M. Katayama, S. Akiyama, H. Nishiyama, Y. Inoue, T. Takewaki, T. Setoyama, T. Minegishi, T. Takata, T. Yamada, and K. Domen, "A Particulate Photocatalyst Water-Splitting Panel for Large-Scale Solar Hydrogen Generation," *Joule,* vol. 2, pp. 509-520, 2018.

[202] M. Schröder, K. Kailasam, S. Rudi, M. Richter, A. Thomas, R. Schomacker, and M. Schwarze, "Impact of the reaction conditions on the photocatalytic reduction of water on mesoporous polymeric carbon nitride under sunlight irradiation," *Int. J. Hydrog. Energy,* vol. 39, pp. 10108-10120, 2014.

[203] L. Guo, Y. Chen, J. Su, M. Liu, and Y. Liu, "Obstacles of solar-powered photocatalytic water splitting for hydrogen production: a perspective from energy flow and mass flow," *Energy,* vol. 172, pp. 1079-1086, 2019.

[204] A. David and M. J. Grundmann, "Droop in InGaN light-emitting diodes: A differential carrier lifetime analysis," *Appl. Phys. Lett.,* vol. 96, p. 103504, 2010.

[205] D. Jing, H. Liu, X. Zhang, L. Zhao, and L. Guo, "Photocatalytic hydrogen production under direct solar light in a CPC based solar reactor: Reactor design and preliminary results," *Energy Convers. Manag.,* vol. 50, pp. 2919-2926, 2009.

[206] B. Turan, J.-P. Becker, F. Urbain, F. Finger, U. Rau, and S. Haas, "Upscaling of integrated photoelectrochemical water-splitting devices to large areas," *Nat. Commun.,* vol. 7, p. 12681, 2016.

[207] K. Takeda, F. Mori, Y. Ogiso, T. Ichikawa, K. Nonaka, M. Iwaya, S. Kamiyama, H. Amano, and I. Akasaki, "Internal quantum efficiency of GaN/AlGaN-based multi quantum wells on different dislocation densities underlying layers," *Phys. Status Solidi C,* vol. 7, pp. 1916-1918, 2010.

[208] K. Ban, J.-I. Yamamoto, K. Takeda, K. Ide, M. Iwaya, T. Takeuchi, S. Kamiyama, I. Akasaki, and H. Amano, "Internal quantum efficiency of whole-composition-range AlGaN multiquantum wells," *Appl. Phys. Express,* vol. 4, p. 052101, 2011.

[209] J. Mickevičius, E. Kuokstis, V. Liuolia, G. Tamulaitis, M. S. Shur, J. Yang, and R. Gaska, "Photoluminescence dynamics of AlGaN quantum wells with built-in electric fields and localized states," *Phys. Status Solidi A,* vol. 207, pp. 423-427, 2010.

[210] J. S. Im, H. Kollmer, J. Off, A. Sohmer, F. Scholz, and A. Hangleiter, "Reduction of oscillator strength due to piezoelectric fields in GaN/$Al_xGa_{1-x}N$ quantum wells," *Phys. Rev. B,* vol. 57, pp. R9435-R9438, 1998.

[211] T. F. Kent, S. D. Carnevale, A. T. M. Sarwar, P. J. Phillips, R. F. Klie, and R. C. Myers, "Deep ultraviolet emitting polarization induced nanowire light emitting diodes with $Al_xGa_{1-x}N$ active regions," *Nanotechnology,* vol. 25, p. 455201, 2014.

[212] P. Dogan, O. Brandt, C. Pfuller, J. Lahnemann, U. Jahn, C. Roder, A. Trampert, L. Geelhaar, and H. Riechert, "Formation of high-quality GaN microcrystals by pendeoepitaxial overgrowth of GaN nanowires on Si(111) by molecular beam epitaxy," *Cryst. Growth Des.,* vol. 11, pp. 4257-4260, 2011.

[213] Q. Li, Y. Lin, J. R. Creighton, J. J. Figiel, and G. T. Wang, "Nanowire-templated lateral epitaxial growth of low-dislocation density nonpolar a-plane GaN on r-plane sapphire," *Adv. Mater.,* vol. 21, pp. 2416-2420, 2009.

[214] S. Fan, S. Zhao, X. Liu, and Z. Mi, "Study on the coalescence of dislocation-free GaN nanowires on Si and SiO_x," *J. Vac. Sci. Technol. B.,* vol. 32, p. 02c114, 2014.

[215] B. Jenichen, O. Brandt, C. Pfüller, P. Dogan, M. Knelangen, and A. Trampert, "Macro-and micro-strain in GaN nanowires on Si(111)," *Nanotechnology,* vol. 22, p. 295714, 2011.

[216] V. M. Kaganer, B. Jenichen, O. Brandt, S. Fernández-Garrido, P. Dogan, L. Geelhaar, and H. Riechert, "Inhomogeneous strain in GaN nanowires determined from x-ray diffraction peak profiles," *Phys. Rev. B,* vol. 86, p. 115325, 2012.

[217] S. Fernández-Garrido, V. M. Kaganer, C. Hauswald, B. Jenichen, M. Ramsteiner, V. Consonni, L. Geelhaar, and O. Brandt, "Correlation between the structural and optical properties of spontaneously formed GaN nanowires: A quantitative evaluation of the impact of nanowire coalescence," *Nanotechnology,* vol. 25, p. 455702, 2014.

[218] B. H. Le, S. Zhao, X. Liu, S. Y. Woo, G. A. Botton, and Z. Mi, "Controlled Coalescence of AlGaN Nanowire Arrays: An Architecture for Nearly Dislocation-Free Planar Ultraviolet Photonic Device Applications," *Adv. Mater.,* vol. 28, pp. 8446-8454, 2016.

[219] J. F. Kaeding, H. Asamizu, H. Sato, M. Iza, T. E. Mates, S. P. DenBaars, J. S. Speck, and S. Nakamura, "Realization of high hole concentrations in Mg doped semipolar (101¯1¯) GaN," *Appl. Phys. Lett.,* vol. 89, p. 202104, 2006.

[220] A. A. Toropov, E. A. Shevchenko, T. V. Shubina, V. N. Jmerik, D. V. Nechaev, M. A. Yagovkina, A. A. Sitnikova, S. V. Ivanov, G. Pozina, J. P. Bergman, and B. Monemar, "Suppression of the quantum-confined Stark effect in $Al_xGa_{1-x}N/Al_yGa_{1-y}N$ corrugated quantum wells," *J. Appl. Phys.,* vol. 114, p. 124306, 2013.

[221] M. Gilbert and D. Ferry, "Indium arsenide quantum wire trigate metal oxide semiconductor field effect transistor," *J. Appl. Phys.,* vol. 99, p. 054503, 2006.

[222] M. Je, S. Han, I. Kim, and H. Shin, "A silicon quantum wire transistor with one-dimensional subband effects," *Solid State Electron.,* vol. 44, pp. 2207-2212, 2000.

[223] K. Morimoto, Y. Hirai, K. Yuki, and K. Morita, "Fabrication and transport properties of silicon quantum wire gate-all-around transistor," *Jpn. J. Appl. Phys.,* vol. 35, p. 853, 1996.

[224] J. Kedzierski, J. Bokor, and E. Anderson, "Novel method for silicon quantum wire transistor fabrication," *J. Vac. Sci. Technol. B,* vol. 17, pp. 3244-3247, 1999.

[225] K. Trivedi, H. Yuk, H. C. Floresca, M. J. Kim, and W. Hu, "Quantum confinement induced performance enhancement in sub-5-nm lithographic Si nanowire transistors," *Nano Lett.,* vol. 11, pp. 1412-1417, 2011.

[226] R. Chau, S. Datta, M. Doczy, B. Doyle, B. Jin, J. Kavalieros, A. Majumdar, M. Metz, and M. Radosavljevic, "Benchmarking nanotechnology for high-performance and low-power logic transistor applications," *IEEE Trans. Nanotechnol.,* vol. 4, pp. 153-158, 2005.

[227] H. Amano, I. Akasaki, K. Hiramatsu, N. Koide, and N. Sawaki, "Effects of the buffer layer in metalorganic vapour phase epitaxy of GaN on sapphire substrate," *Thin Solid Films,* vol. 163, pp. 415-420, 1988.

[228] T. Hisatomi, K. Maeda, K. Takanabe, J. Kubota, and K. Domen, "Aspects of the Water Splitting Mechanism on $(Ga_{1-x}Zn_x)(N_{1-x}O_x)$ Photocatalyst Modified with $Rh_{2-y}Cr_yO_3$ Cocatalyst," *J. Phys. Chem. C,* vol. 113, pp. 21458-21466, 2009.

[229] E. Bobkova, V. Grilikhes, A. Soluyanov, and M. Shvarts, "Effect of chromatic aberration on the concentration of solar radiation by Fresnel lenses," *Tech. Phys. Lett.,* vol. 32, pp. 1039-1042, 2006.

[230] E. Lorenzo, "Chromatic aberration effect on solar energy systems using Fresnel lenses," *Appl. Opt.,* vol. 20, pp. 3729-3732, 1981.